Physics-Based Models of Hysteresis in Multiphase Flow in Porous Media

by

Zongyu Gu

B.E.(Hons), University of Auckland (2014)
M.S., Massachusetts Institute of Technology (2016)

Submitted to the Department of Chemical Engineering
in partial fulfillment of the requirements for the degree of

Doctor of Philosophy in Chemical Engineering

at the

MASSACHUSETTS INSTITUTE OF TECHNOLOGY

September 2019

© Massachusetts Institute of Technology 2019. All rights reserved.

Signature redacted

Author .....
Department of Chemical Engineering
July 18, 2019

Signature redacted

Certified by .....
Martin Z. Bazant
E. G. Roos (1944) Professor of Chemical Engineering
Executive Officer, Department of Chemical Engineering
Professor of Mathematics
Thesis Supervisor

Signature redacted

Accepted by .....
Patrick S. Doyle
Robert T. Haslam (1911) Professor of Chemical Engineering
Singapore Research Professor
Chairman, Committee for Graduate Students

MASSACHUSETTS INSTITUTE OF TECHNOLOGY
SEP 19 2019
LIBRARIES
ARCHIVES

Physics-Based Models of Hysteresis in Multiphase Flow in Porous Media

by

Zongyu Gu

Submitted to the Department of Chemical Engineering
on July 18, 2019, in partial fulfillment of the
requirements for the degree of
Doctor of Philosophy in Chemical Engineering

Abstract

We propose a novel probabilistic framework based on pore-scale probabilistic events to derive a theory of hysteresis in multiphase flow in porous media. In particular, we define the pore-space accessivity to contrast the serial and parallel arrangement of different-radius pore slices, and the radius-resolved saturations to detail the pore-scale distribution of immiscible fluids. We show that accessivity can be measured by mercury cyclic porosimetry. Our microscopic theory of hysteresis produces simple formulae that are suitable for use as hysteresis-enabling constitutive laws for capillary pressure and relative permeabilities in conventional continuum simulations of multiphase flow.

Thesis Supervisor: Martin Z. Bazant
Title: E. G. Roos (1944) Professor of Chemical Engineering
Executive Officer, Department of Chemical Engineering
Professor of Mathematics


B
a tempo
con sord.
mp

Acknowledgments

Over the course of my doctoral studies, I have crossed paths with many groups and individuals, some leaving a lasting impression on me. They have my heartfelt gratitude, yet I forgo the pleasure of thanking all of them by name. Here, in particular, I acknowledge the following people:

- The amazing musicians at MIT with whom I have been able to share my unquenchable passion for music, including:
  - The MIT Video Game Orchestra (VGO), in which I have played clarinet and bass clarinet since its founding in Fall 2016, and which I have had the pleasure of codirecting since Fall 2018;
  - Larry Wang, the revered founder of the VGO, who inspired me to take up orchestral arranging;
  - Sebastian Franjou, my fellow codirector of the VGO, with whom I became friends through not only music but also trips to Haymarket and cooking;
  - Other VGO execs and members for their commitment to the VGO and sheer musical brilliance, including Iganacio Perez Pedoya, Andrew Lin, Michael Tang, and so many others;
  - Hane Lee, Sam Moore, Forest Tong, Evan Lynch, and others in the MIT Improvisation Ensemble;
  - Stephanie Doong, Alex Ji, and Kiera Tai, and others in MIT Ribotones;
  - German Parada, Adrian Silva, and others with whom I have played music or watched concerts;
  - Mentors on the MIT music faculty, especially Prof. Charles Shadle, who taught me in 21M.303, 21M.304, and 21M.310 and helped me grow as a composer;
- Jim Chu (also Zihan Xu and SXC), Max Liu, Moo Sun Hong, Alex Brayton, and other good friends for the time we have spent together;

- The phenomenal people that I had the fortune of sharing my Practice School experience with, including my classmates, station directors, and sponsors at Emirates Global Aluminium and the Food and Drug Administration;
- All students who took 10.50 in Fall 2017, for which McLain Leonard and I were teaching assistants;
- The MIT Educational Studies Program for their amazing platform for teaching middle- and high-school students;
- The team for the indie game "Alight" for the opportunity to compose a video game soundtrack (see Page 5);
- My parents and extended family, whose unwavering advocacy for my well-being above all else is well taken;
- My thesis committee, Prof. Ruben Juanes and Prof. Klavs Jensen, for their constructive feedback on my research and career goals;
- Members of the MIT Digital Learning Lab and MIT Open Learning at large, especially Jen French and Michelle Tomasik for helping me get started on 10.50.1x;
- Members of the Bazant research group, including Amin Amooie, Mohammad Mirzadeh, and Tingtao Zhou with whom I have closely collaborated on research, as well as Pedro de Souza, Surya Effendy, and Hongbo Zhao with whom I worked on the Fall 2018 run of 10.50.1x;
- My advisor, Prof. Martin Bazant, for whom I have profound respect as a scientist, and to whom I am indebted for the various circumstances that he helped create to enable me to pursue my interest in education.

I am also thoroughly grateful to my old friends and mentors in New Zealand and China for their support and guidance before I moved to the United States, without whom I am most certain that my life would have taken a very different trajectory.

Lastly, I will say that the music of Дмитрий Дмитриевич Шостакович has brought me hope in even the most difficult times.

Contents

List of Figures

List of Tables

Chapter 1

Introduction

Porous materials are truly ubiquitous in both nature and civilization. From rocks and wood to concrete and heterogeneous catalysts, they vary widely in origin, properties, and applications. Despite their macroscopic appearance as solid objects, porous media are distinguished by their ability to contain fluids internally, owing to their heterogeneous microstructure – the solid matrix occupies only a portion of the macroscopic domain, while the complementary pore space is able to accommodate one or more fluid phases [2].

As a result, **transport phenomena** in porous media are central to innumerable engineering applications: after a storm, rainwater drains away by infiltrating through a permeable city pavement [3]; at an oil and gas extraction site, hydrocarbons flow under pressure through geological structures to reach production wells [4]; during the day, humidity fluctuations in a house are buffered by the cyclic uptake and release of moisture in wood layers in the floor and the wall [5]; in a chemical reactor, reactants are delivered to the surface of a catalyst pellet in a packed bed before they diffuse through pores into the pellet and react away on the internal catalytic surface [6]; ...

The design and operation of these and many other engineering systems thus draw heavily on **continuum models** of porous media, where microscopic details at the length scale of individual pores are smeared out to give way to homogenized macroscopic descriptions of the medium as a whole. In the typical case of well-connected pores, continuum models tend to work well for diverse physical phenomena occur-

ring in porous media, including fluid flow, heat and mass transfer, gas adsorption, phase transformations, and chemical reactions [7]. Remarkably, these models encapsulate the essential features of the often nontrivial pore-space morphologies in a small number of parameters like **porosity** (ϕ), **tortuosity** (τ), **intrinsic permeability** (k_s), **specific surface area** (a_s), etc. – a well-known example is the eponymous constitutive law of French engineer Henry P. G. Darcy for fluid flow in porous media:

$$\mathbf{q} = -\frac{k_s}{\mu}\left(\nabla p - \rho \mathbf{g}\right), \tag{1.1}$$

which Darcy proposed based on experimental observations of the steady flow of water through a vertical column of sand [8]. Here, $\mathbf{q}$ is called the **specific discharge** or **Darcy velocity** (defined as the volumetric flow rate of fluid per unit area of the porous medium), μ and ρ are the viscosity and the density of the fluid, respectively, $\mathbf{g}$ is the gravitational acceleration, and p denotes the fluid pressure variable.

Over time, **Darcy's law** has acquired an axiomatic status so venerated that it customarily serves as the starting point for modeling more complex flows in porous media, some of which barely resembling Darcy's original experimental system. In continuum simulations, the intrinsic permeability is sometimes generalized to a spatially dependent tensor, $\mathbf{k}_s(\mathbf{x})$, to account for heterogeneity and anisotropy in real porous media [2]; Forchheimer [9] and Klinkenberg [10] proposed corrections to Darcy's law to include inertial and slip effects, which may become important when the Reynolds number and the Knudsen number, respectively, are no longer much less than unity [11]; in a seemingly far-fetched but now canonized attempt, Darcy's law was even modified to describe dense granular flow [12]; lastly, of principal importance to this thesis is, naturally, the generalization of Darcy's law to **multiphase flow** in porous media, where immiscible fluid phases (liquids or gases) jointly occupy the pore space [13, 14]. In the special case of **two-phase flow**, denoting the two phases by w and n (we will explain the physical significance of these labels in Section 2.1.3), the system of continuum governing equations, consisting of several Partial Differential Equations

(PDEs) and algebraic constraints, may be written as[1] [2, 15]:

$$\phi \frac{\partial s_w}{\partial t} = -\nabla \cdot \mathbf{q}_w, \quad \phi \frac{\partial s_n}{\partial t} = -\nabla \cdot \mathbf{q}_n, \tag{1.2}$$

$$\mathbf{q}_w = -\frac{k_s k_{rw}(s_w)}{\mu_w} \left(\nabla p_w - \rho_w \mathbf{g}\right), \quad \mathbf{q}_n = -\frac{k_s k_{rn}(s_w)}{\mu_n} \left(\nabla p_n - \rho_n \mathbf{g}\right), \tag{1.3}$$

$$p_n - p_w = p_c(s_w), \tag{1.4}$$

$$s_w + s_n = 1. \tag{1.5}$$

In this formulation, either phase is associated with its own **saturation**, Darcy velocity, **relative permeability**, and pressure, e.g., s_w, $\mathbf{q}_w$, k_{rw}, and p_w, respectively, for phase w, in addition to standard fluid properties. Eq. (1.2) are differential statements of mass conservation, where saturation is defined as the volume fraction of pore space occupied by either fluid phase; the saturations of the two phases must sum to unity by definition, which is reflected in Eq. (1.5). Darcy's law for single-phase flow, Eq. (1.1), is modified to give Eq. (1.3), where multiplicative factors k_{rw} and k_{rn} account for deviations of Darcy velocities in two-phase flow compared to single-phase flow. Eq. (1.4) imposes an algebraic constraint on the two pressure variable via p_c, which is referred to as the **capillary pressure**. Conventionally, p_c, k_{rw}, and k_{rn} are given as predetermined functions of s_w. While the approach may work as a first approximation, these relationships suffer from **hysteresis**, as illustrated in Figure 1-1. Given a certain s_w at some location in a porous medium, depending on the past trajectory of s_w, the capillary pressure and the relative permeabilities may assume different values. For example, during **drainage**, which is when s_w locally decreases, the values of p_c, k_{rw}, and k_{rn} generally differ from those during **imbibition**, which is when s_w locally increases; these behaviors become more complex when s_w undergoes arbitrary cyclic fluctuations.

In practice, hysteresis is often described empirically or neglected altogether in continuum simulations of multiphase flow in porous media, although it is considered crucial for making certain type of predictions, e.g., [16, 17, 18]. Thus, the overall

[1] assuming that the solid matrix and the fluid phases are incompressible and all material properties are homogeneous and anisotropic

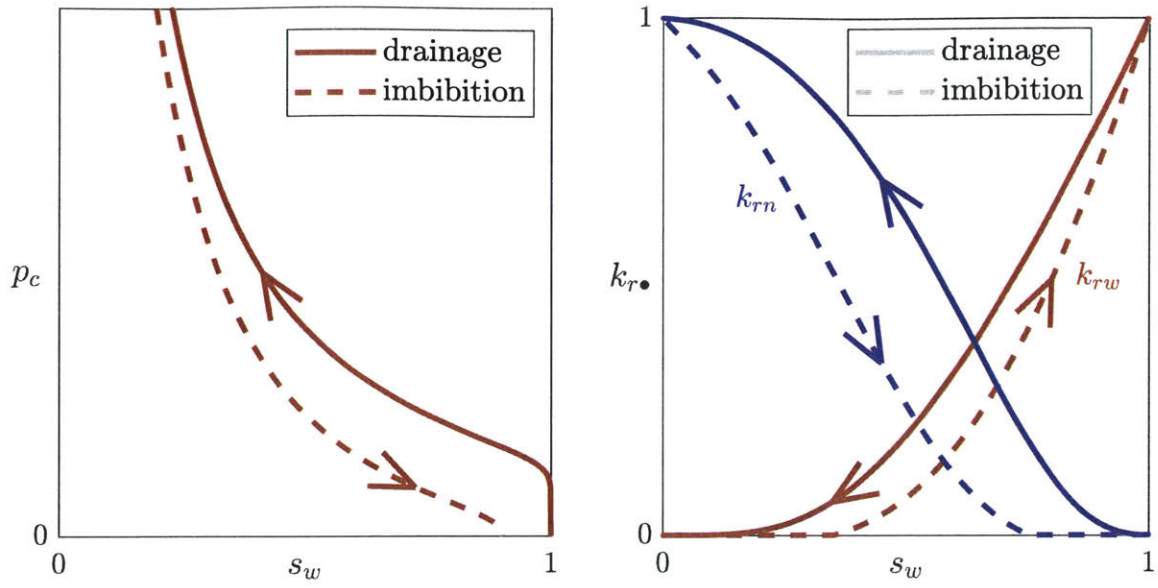

Figure 1-1: Qualitative features of hysteresis in the relationship between capillary pressure and saturation as well as that between the relative permeability of either phase and saturation in the conventional formulation of two-phase flow in porous media.

objective of this thesis is to build upon conventional continuum formulations of multiphase flow in porous media to include the effects of hysteresis. The modifications should reflect the pore-scale physical processes that are responsible for hysteresis in the first place, but remain simple enough to be incorporated into current applications. In the short term, the new concepts we propose may be incorporated into conventional continuum models for incremental improvements, while in the long term, they may be subject to pore-scale investigations, and ultimately play a role in future continuum models of multiphase flow.

Chapter 2

Modeling pore-space morphology

Certain transport processes in porous media, such as heat conduction, may involve both the solid matrix and the pore space, while processes like electron conduction may involve only the solid phase. Fluid flow in a porous medium, on the other hand, occurs exclusively in the pore space, and is hence strongly influenced by both the geometry of individual pore units and the way they are interconnected, or their topology. We say that the geometrical and topological features of the pore space constitute its **morphology** [19].

Therefore, the kinds of coarse-grained descriptions found in continuum models of fluid flow in porous media should reflect essential characteristics of the pore-space morphology. In this chapter, we will discuss existing notions related to physically significant aspects of pore-space morphology. We will then introduce new concepts – such as the **pore-space accessivity** – and establish a unified modeling framework which we will use to derive many of the results in this thesis.

2.1 Existing concepts

Like with other composite materials, we can record the precise microstructure of a porous medium with the function:

$$p_s : \Omega \to \{0,1\} : \mathbf{x} \mapsto \begin{cases} 1 & \text{the point } \mathbf{x} \text{ belongs to the pore space} \\ 0 & \text{the point } \mathbf{x} \text{ belongs to the solid matrix,} \end{cases} \tag{2.1}$$

where $\Omega \subset \mathbb{R}^3$ denotes the 3-D physical domain occupied by the medium. The function $p_s(\mathbf{x})$ encodes the morphology of the pore space. We rarely have a precise knowledge of $p_s(\mathbf{x})$ for real porous specimens, although numerous image acquisition and processing techniques can be used to estimate $p_s(\mathbf{x})$ up to some spatial resolution and sample size – see Section 7.2. This information would then enable the simulation of physical processes at the **pore scale**, the challenges notwithstanding. As far as continuum modeling is concerned, there are numerous quantitative properties that are useful for characterizing the pore-space morphology at the continuum scale. We will review some of them here.

2.1.1 Porosity

The average **porosity** of a porous sample occupying a domain of Ω is defined as:

$$\overline{\phi} \equiv \int_{\Omega} p_s(\mathbf{x})\, \mathrm{d}\Omega, \tag{2.2}$$

which equals the ratio of the volume of the pore space in Ω to that of Ω itself [2, 7]. Because $p_s(\mathbf{x}) \in \{0,1\}, \forall \mathbf{x} \in \Omega$, we have $\overline{\phi} \in [0,1]$. In the limit $\overline{\phi} \to 0$, the medium becomes plainly the solid, while the limit of $\overline{\phi} \to 1$ represents a homogeneous free space available for fluid occupation.

For homogeneous porous materials or those with a periodic microstructure, it seems reasonable to assign to each location within the medium a local porosity that is equal to the average porosity in Ω, namely, $\phi(\mathbf{x}) = \overline{\phi}$. For example, con-

sider a close-packing of monodispersed spheres, which has an average porosity of $\overline{\phi} = 1 - \pi/(3\sqrt{2}) \approx 0.26$, the lowest among any infinite packing of equal spheres [20, 21]; we may plausibly associate this porosity value with different macroscopic regions in the close-packing, which are morphologically identical. On the other hand, for heterogeneous media, the proper continuum definition of $\phi(\mathbf{x})$ is more elusive. The usual strategy is to consider a so-called **representative elementary volume (REV)** surrounding each point $\mathbf{x}$, which we denote by V here, and define:

$$\phi(\mathbf{x}) \equiv \int_V p_s(\mathbf{x})\, \mathrm{d}V, \tag{2.3}$$

where $V \subset \Omega$ is a neighborhood of $\mathbf{x}$ that is much smaller in size than Ω, but large enough[1] so that the value of $\phi(\mathbf{x})$ obtained is insensitive to small changes in the size of the REV [15].

The porosity informs many macroscopic properties of porous media. For example, the average bulk density of a porous medium is given by:

$$\overline{\rho} = \overline{\phi}\rho_f + (1 - \overline{\phi})\rho_s, \tag{2.4}$$

where ρ_f and ρ_s are the densities of the pore-space fluid and the solid matrix, respectively. Effective transport coefficients in a homogeneous porous medium, such as the mean effective thermal conductivity, denoted by $\overline{k}$, are generally not uniquely determined from ϕ, but are guaranteed to lie within certain bounds that are functions of ϕ. For example, in an anisotropic porous medium, $\overline{k}$ obeys the Wiener bounds [22]:

$$\frac{1}{\phi/k_f + (1-\phi)/k_s} \leq \overline{k} \leq \phi k_f + (1-\phi)k_s, \tag{2.5}$$

where k_f and k_s are the thermal conductivities in the pore-space fluid and the solid matrix, respectively[2]. The Hashin-Shtrikman bounds [23] for isotropic porous media similarly depend on ϕ.

[1] In the limit of $V \to 0$, Eq. (2.3) returns a $\phi(\mathbf{x})$ that equals either zero or unity, as given by $p_s(\mathbf{x})$.

[2] neglecting modes of heat transfer other than conduction in the fluid, e.g., natural convection

Finally, we note that the definitions given in Eqs. (2.2) and (2.3) correspond to what one may call the **total porosity**. This term is created to distinguish it from **accessible porosity**, which only accounts for the subset of the pore space that is reachable from the outside of the porous medium via a continuous path through the pore space [19]. Virtually all physical processes considered in this thesis involve fluid flows of one kind or another, where a genuinely isolated pore pocket, into which fluids cannot enter, is functionally equivalent to a part of the solid matrix. For that reason, we favor accessible porosity as the physically relevant measure of porosity.

2.1.2 Tortuosity

Tortuosity, which is also referred to as the **tortuosity factor**, is sometimes taken intuitively as:

$$\tau \sim \frac{L_e}{L} \quad \text{or} \quad \tau \sim \left(\frac{L_e}{L}\right)^2, \tag{2.6}$$

where L is the straight-line distance along a particular transport direction in the porous medium, and L_e is the typical arc length of a tortuous microscopic path spanning the distance that is followed by a tracer particle in the pore space [24], although the more rigorous definition is based on the effective tracer diffusivity through the porous medium[3]:

$$D_{\text{eff}} = \frac{D\phi}{\tau}, \tag{2.7}$$

where D is the "true" diffusivity in the pore space. Based on the above, we expect $\tau \in [1, \infty)$.

In general, the macroscopic definition of τ in Eq. (2.7) does not have a definitive connection to its simplistic microscopic geometrical interpretation in Eq. (2.6), and τ can only be reliably determined by studying diffusion through the porous medium [25]. Nevertheless, the limit of low tortuosity, $\tau \to 1$, would plausibly be represented

[3]assuming that no diffusion occurs in the solid matrix

by a collection of straight (i.e., least "tortuous") channels that are oriented parallel to the direction of transport. As we raise τ, the typical residence time of a tracer particle undergoing diffusion in the pore space increases, leading to slower transport [24], which is in fact due to branched, non-percolating paths and serial connections in the pore network [7].

In the classical chemical engineering literature [26, 27, 28, 29], the intrinsic permeability seen in Eq. (1.1) is similarly linked to porosity and tortuosity. Approximating the pore space as a bundle of channels that are nearly identical in their cross-sectional shapes and effective radii, the intrinsic permeability may be modeled as:

$$k_s = C\frac{\phi}{\tau}, \tag{2.8}$$

where the linear proportionality constant C has units of area and is dependent on geometrical properties of the channels, such as analyzed in [30].

2.1.3 Pore-size distribution

Imagine tracing a straight line L in an infinite homogeneous porous medium in 3D. Given the pore-space morphology as indicated by $p_s(\mathbf{x})$, we may break L into a collection of nonadjacent line segments that fall entirely within either the pore space or the solid matrix. That is, we may express the set $L_1 = \{\mathbf{x} \in L : p_s(\mathbf{x}) = 1\}$ as the union of a number of nonadjacent and disjoint subsets. Repeating this process with various L, we obtain a collection of such pore space–spanning line segments, whose lengths give some indication as to the typical **pore sizes** in the porous medium.

Crucially, these pore sizes mark a length scale[4] at the level of individual pores that is distinct from the macroscopic dimensions of a porous specimen. In truth, key pore-scale physics are dictated by the local dimensions of the pore space.

To illustrate, suppose that a part of the pore space resembles a straight cylindrical capillary of radius r. Then, viscous flow through the pore is described by the **Hagen-**

[4]or possibly a plurality of length scales in hierarchical porous materials

Poiseuille equation [31]:

$$Q = \frac{\pi r^4}{8\mu} \left| \frac{\mathrm{d}\mathscr{P}}{\mathrm{d}z} \right|, \tag{2.9}$$

where Q is the volumetric flow rate, and $|\mathrm{d}\mathscr{P}/\mathrm{d}z|$ is the magnitude of the dynamic pressure gradient along the pore axis[5]. Intuitively speaking, the larger the radii of pores, the smaller their resistances to flow.

Capillary phenomena are also strongly influenced by local pore dimensions. Note that for a chosen combination of two immiscible fluids and a solid, we may identify one fluid as the **wetting phase**, labeled w, and the other as the **nonwetting phase**, labeled n; at equilibrium, along a contact line that simultaneously borders all three phases, the **static contact angle** as measured in the wetting phase, which is defined as the angle between the w-n interface and the s-w interface at the contact line, is less than $\pi/2$, whose supplementary angle, which is greater than $\pi/2$, equals the contact angle as measured in the nonwetting phase[6]. Now, consider two immiscible fluids in a straight cylindrical channel of radius r; at mechanical equilibrium, the meniscus separating the two fluids takes the shape of a spherical cap that is symmetric about the central axis of the channel[7], as shown in Figure 2-1. The interfacial pressure difference, or the **capillary pressure**[8], can be evaluated using the **Young–Laplace equation** [31]:

$$p_n - p_w = \frac{2\gamma_{wn}\cos\theta_c}{r}, \tag{2.10}$$

with θ_c being measured in the wetting phase. This equation is also known as the

[5]assuming that the Reynolds number and the Knudsen number are both small, i.e., $\mathrm{Re} = \rho Q/\mu r \ll 1$ and $\mathrm{Kn} = \lambda/r \ll 1$, where λ is the mean free path of a fluid molecule

[6]The identities of the fluids as wetting and nonwetting phases are determined based on the three interfacial tension values associated with the three pairwise interactions between phases, namely, γ_{wn}, γ_{sw}, and γ_{sn}, respectively, as we always have $\gamma_{sw} < \gamma_{sn}$. The equilibrium contact angle is given by **Young's equation** or the **Young–Dupré equation**, $\gamma_{\alpha\beta}\cos\theta_c + \gamma_{s\alpha} = \gamma_{s\beta}$, where α and β are labels for the two fluid phases and θ_c is measured in the wetting phase [31]. It is easy to verify that $\gamma_{s\alpha} < \gamma_{s\beta} \iff \theta_c < \pi/2$ and that $\gamma_{s\alpha} > \gamma_{s\beta} \iff \theta_c > \pi/2$, given that $\theta_c \in (0, \pi)$.

[7]assuming that the Bond number is small, i.e., $\mathrm{Bo} = |\rho_w - \rho_n| g r^2/\gamma_{wn} \ll 1$

[8]This pore-scale capillary pressure must be distinguished from the "macroscopic" capillary pressure used in continuum models, e.g., in Eq. (1.4), although the two concepts are not unrelated.

Washburn equation [32], which we will revisit in Section 4.1. Intuitively speaking, for a fixed combination of two fluids and a porous medium, the smaller the radii of pores, the larger the pressure in the nonwetting phase (relative to that in the wetting phase) required to keep the meniscus in equilibrium, and hence the more favorable for the wetting phase to imbibe and replace the nonwetting phase in those pores – that is, it is generally more favorable for the wetting fluid to occupy smaller pores and the nonwetting fluid to occupy larger pores at equilibrium[9].

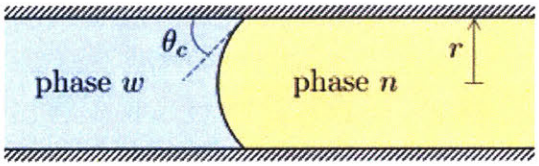

Figure 2-1: Two immiscible fluids in a straight cylindrical channel of radius r. The contact angle as measured in the wetting phase, θ_c, is less than $\pi/2$.

Having established the paramount role pore dimensions play in pore-scale physics, it would seem natural to condense the geometrical features of the pore space into a **pore-size distribution (PSD)** that delineates the pore sizes present and how prevalent each size is. Unsurprisingly, there lacks a universally accepted definition of the PSD despite its intuitive appeal, which is perhaps due to the concept being "vague and imprecise" [19]. Traditionally, the PSD is actually defined based on macroscopic measurements such as **mercury porosimetry** [32, 33, 34, 35, 36] and **nitrogen adsorption-desorption** [37, 38, 39], similar to how tortuosity is defined based on the effective tracer diffusivity in Eq. (2.7). More recently, advances in imaging methods like synchrotron X-ray computed microtomography have allowed for direct measurements of 3-D microstructures of porous materials, from which morphological data in the form of a **pore network** can be extracted using a variety of methods [40, 41], such as fitting maximally inscribed spheres in the pore space [42, 43].

In this thesis, we view the pore space as being assembled from cylindrical slices of various radii (or effective radii if the cross sections of the slices are not perfectly

[9]We arrive at the same conclusion based on an energetic argument: because $\gamma_{sw} < \gamma_{sn}$, converting an s-n interface to an s-w interface by itself is always energetically favorable (while displacing the fluid requires work); however, because the volume to surface area ratio is less in smaller pores, on a per volume basis, imbibition is more favorable in smaller pores.

cylindrical), and denote the probability density function (PDF) and the cumulative distribution function (CDF) of the volume-based PSD with $f(r)$ and $F(r)$, respectively, where r denotes the effective pore radius[10]. Hence, $f(r_0)\,\mathrm{d}r$ gives the volume fraction of pore slices whose radii lie between r_0 and $r_0 + \mathrm{d}r$, and the PDF and the CDF are related by:

$$F(r_0) = \int_0^{r_0} f(r)\,\mathrm{d}r. \tag{2.11}$$

Note that the cumulative function F is nondecreasing and right-continuous, and is typically invertible over some interval $[r_{\min}, r_{\max}]$, where $r_{\min}$ and $r_{\max}$ denote the minimum and maximum radius present, respectively[11]. Thus, in a practical sense, there is a one-to-one correspondence between pore radii and values of the CDF. It is thus acceptable to refer to any pore size r_0 by the corresponding $F_0 = F(r_0)$ value; in other words, we may say a pore slice is "of size F_0" when all pore slices of the same radius or smaller make up a volume fraction of F_0 of the pore space. As we shall see in the subsequent analyses, using F as a surrogate for pore size is particularly advantageous when the pore-scale events of interest are controlled by only the relative order of pore radii rather than their absolute magnitudes. This way, we can express the relevant results more generally and independently from specific PSDs.

2.2 Our probabilistic framework

In this section, we will establish additional continuum properties of porous materials to describe other aspects of the morphology of pore space, which we conceptualize using a new probabilistic framework.

[10]Note that we may also define length-based PSD whose density function $f_l(r)$ satisfies $f(r) = r^2 f_l(r) / \int_0^\infty r^2 f_l(r)\,\mathrm{d}r$. One can similarly define a surface area-based PSD. The logarithm of pore radius is also used as the independent variable in describing these distributions [19, 44].

[11]If F is not invertible, then we take the quantile function as its effective inverse, defined as $Q : [0,1] \to [r_{\min}, r_{\max}] : F_0 \mapsto \inf\{r_0 \in [r_{\min}, r_{\max}] : F(r_0) \geq F_0\}$.

2.2.1 Skeletal representation of pore space

We make the simplifying assumption that the relevant features of pore-space morphology can be reduced to a lower-dimensional representation based on the **pore skeleton** in the form of intersecting space curves, as we illustrate in Figure 2-2. While the precise definition of the skeletal representation may vary (see Section 7.2), the basic idea is that there is a certain axial direction associated with any location in the pore space. In this sense, a tracer – which could be a meniscus between two immiscible fluid phases, for example – can traverse the pore space by moving along the pore skeleton. At every point along on the pore skeleton, the cross section in the transverse direction can be associated with an effective pore radius[12]. To parameterize locations along the pore skeleton, we define an axial coordinate that measures the "distance" of pore-space traversal, which could be based on the cumulative pore volume, for example[13].

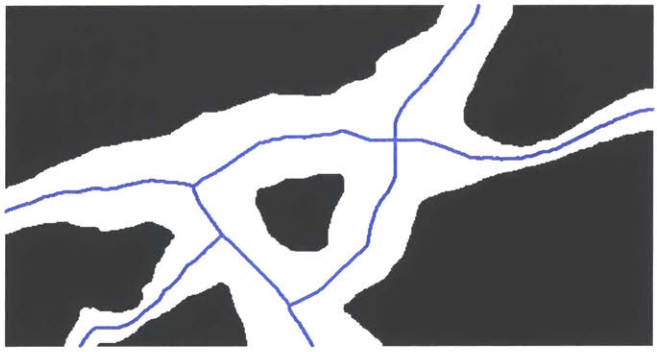

Figure 2-2: An illustration of the skeletal representation of a pore space in a hypothetical 2-D porous sample. The black and white areas corresponds to the solid matrix and the pore space, respectively, and the blue curves depict the pore skeleton. Different branches of the pore skeleton intersect at junctions, which display various coordination numbers. Reproduced from [1].

[12]There are many possible definitions of the effective pore radius for irregular cross-sectional shapes. For example, the definition could be based on capillary equilibrium, as implied by the average curvature of a meniscus at equilibrium at the given axial location. The radius of an equivalent straight cylindrical pore hosting a stationary meniscus with the same curvature under the same conditions is then taken as the effective pore radius.

[13]That is, the incremental difference in the axial coordinates of two nearby points on the pore skeleton is equal to the volume of pore space "explored" by traveling between the two points. Other measures of axial distance include the arc length of the pore skeleton and the exposed surface area of the solid.

As a tracer traverses the pore space along its skeleton, the effective pore radius may change, which we may record as a function of the axial coordinate. By compiling radius measurements across the pore skeleton weighted by the pore volume associated with each radius, we also obtain a volume-based PSD. Also, the tracer may also encounter **junctions** where parts of the skeleton that are oriented in different axial directions intersect, or where the skeleton terminates. We refer to the joining region between two adjacent junctions as a **pore branch**. The **coordination number** of a junction, denoted by z, is equal to the number of pore branches emanating from it. We have $z = 1, 3, 4, \ldots$, with $z = 1$ corresponding to a "dead end" in the pore space or an opening on the outer boundary of domain of the medium, $z = 3$ corresponding to a 3-coordinate junction, and so forth[14].

Note that the skeletal representation of pore-space morphology is expect to work best when pore branches are long and thin and have axisymmetric cross sections, so that the effective radii are readily identified along the skeleton. Aside from that, the assignment of regions of the pore space to individual branches near a junction may be ambiguous. Thus, like the determination of the PSD, the identification of pore skeleton and the assignment of pore radii at axial locations may be inherently vague for real porous media. We argue that this framework should be recognized primarily for its usefulness in motivating continuum models.

2.2.2 Pore-space instance

In order to create continuum descriptions of pore-space morphology based on the pore-scale skeletal representation introduced above, we resort to probabilistic methods. Suppose a tracer enters the pore space of a control volume of a porous medium from its boundary and traverses the pore space along its skeleton, multiplying at each junction whose $z \geq 3$ – tantamount to a **branching process** – so as to traverse each subsequent branch, until it encounters a 1-coordinate junction. Such an experiment yields a **pore-space instance**, which includes the pore space explored by the tracer

[14]Note that $z = 2$ is not considered a valid coordination number because such a junction cannot be meaningfully differentiated from an internal point on the skeleton of a pore branch

and any pore radius data. Figure 2-3 shows an example of such a pore-space instance.

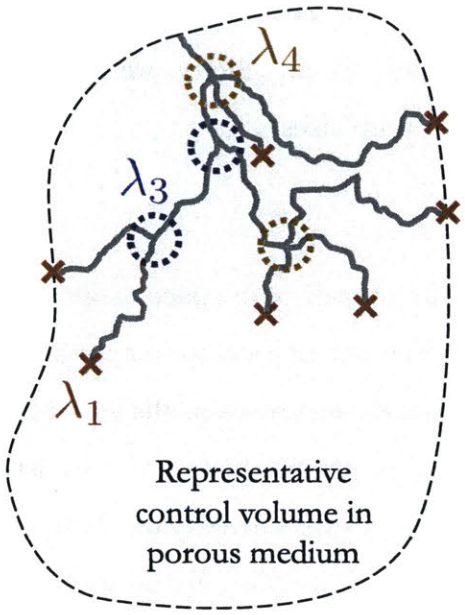

Figure 2-3: A conceptual illustration of the branching process and the resulting pore-space instance in a representative control volume of a porous medium. Junctions of various coordination numbers may occur at distinct frequencies, each following an independent homogeneous Poisson point process. The pore radius varies along the axial coordinate of every branch, which is similarly described by an independent homogeneous Poisson point process. Note the absence of loops in the instance.

As the tracer traverses the pore space, we assume that it encounters junctions of each coordination number z at a fixed rate of λ_z, which has units of the reciprocal of those of the chosen axial coordinate. Hence, the occurrence of z-coordinate junctions is described by an independent **homogeneous Poisson point process**[15] for each z.

Similarly, we assume that the variation of pore radius along a branch is described by a homogeneous Poisson point process with a constant rate of ℓ^{-1}. Strictly speaking, this results in a series of constant-radius **pore segments**, whose axial dimensions follow an exponential distribution with a mean of ℓ, and whose radii are drawn at random from a prescribed PSD. Because we expect the pore radius to vary smoothly along the axial coordinate in real porous media, ℓ may be interpreted as the typical axial distance over which the pore radius becomes uncorrelated; if we examine r as a function of the axial coordinate in the frequency domain, ℓ may correspond to the

[15]See Appendix A for discussions about properties of homogeneous Poisson point processes.

typical location of the peak signal. Of course, ℓ may in reality also depend on the instantaneous pore radius, e.g., if r varies more rapidly with respect to the axial coordinate as it becomes smaller; for simplicity, we assume that there exists some average ℓ that works across all pore sizes.

Hence, we conceptualize the overall pore space as an ensemble of all possible instances constructed from a given set of rate parameters for the Poisson processes, probabilistically weighted. Separate instances in the ensemble are accessed by tracers in parallel. Note that no loops are present in the probabilistic branching process described: within each instance, there exists exactly one path connecting any two points on the pore skeleton. In that sense, the pore instances considered in this framework resemble a **Bethe lattice** or **Cayley tree** [45, 46], although the coordination number may vary from junction to junction in our framework. Thus, the instances in our framework can be regarded as having the topology of what we may elect to call "generalized Bethe lattices".

We can derive expected properties of a pore-space instance using properties of homogeneous Poisson point processes presented in Appendix A. Using those results, we find that the expected axial dimension of a branch is given by:

$$\langle b \rangle = \frac{1}{\lambda_{\mathbb{Z}^+}}, \quad \lambda_{\mathbb{Z}^+} = \sum_{z \in \mathbb{Z}^+} \lambda_z \text{ and } \mathbb{Z}^+ = \{1, 2, 3, \ldots\}, \tag{2.12}$$

where we set $\lambda_2 = 0$ for simplicity of notation. Subsequently, we find that the expected axial dimension of an instance is given by:

$$\langle c \rangle = \frac{1}{\sum_{z \in \mathbb{Z}^+} (2 - z)\lambda_z}, \tag{2.13}$$

which is finite for an instance in a finite control volume, requiring that the denominator be greater than zero – see Appendix A.

2.2.3 Pore-space accessivity

We now have all the ingredients to introduce the first important concept of this thesis, the **pore-space accessivity**:

$$\alpha \equiv \frac{\ell}{\ell + \langle c \rangle}, \tag{2.14}$$

which can also be equivalently written in the following form:

$$\alpha = \frac{q}{1+q}, \quad q \equiv \frac{\ell}{\langle c \rangle} = \ell \sum_{z \in \mathbb{Z}^+} (2-z)\lambda_z, \tag{2.15}$$

implying that:

$$q = \frac{\alpha}{1-\alpha}. \tag{2.16}$$

We note that $q \in (0, \infty)$ and $\alpha \in (0, 1)$. Furthermore, the relationship between q and α is shown in Figure 2-4.

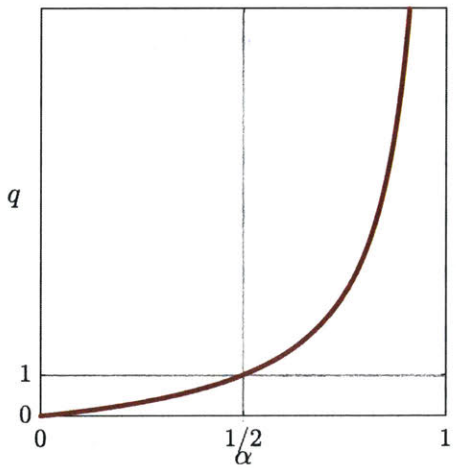

Figure 2-4: Relationship between q and α as given by Eqs. (2.15) and (2.16).

We may interpret $1/q \in (0, \infty)$ as the expected number of pore-size variation events per instance, and hence $1/\alpha = 1 + 1/q \in (1, \infty)$ as the expected number of different-radius pores found in an instance. Thus, $\alpha \in (0, 1)$ is the average volume fraction of an instance which corresponds to the constant-radius pore segments that

are immediately accessible from the exterior of the control volume.

As $\alpha \to 1$, each instance contains only one pore radius, making it entirely accessible from the exterior by a tracer without experiencing variations in pore radius, and different pore radii are only found in parallel instances in the ensemble. As $\alpha \to 0$, an infinite number of distinct pore radii are observed in each instance, making a vanishingly small fraction of the constant-radius pore segments directly accessible from the exterior, which means that different-radius pores are organized in a highly serial manner.

According to Eq. (2.15), increasing λ_1 increases the rate of encountering 1-coordinate junctions, which decreases the expected size of a pore instance with all other conditions kept unchanged, hence increasing accessivity. On the other hand, increasing λ_z for any $z \geq 3$ increases the occurrences of high-coordinate junctions, which increases $\langle c \rangle$ and decreases α. Lastly, keeping all λ_z constant, accessivity increases with increasing ℓ.

We have established a precise microscopic definition of accessivity – given by Eq. (2.14) or Eq. (2.15) – based on our probabilistic framework. Accessivity is a new continuum property of porous medium that characterizes the pore-space morphology in terms of the degree to which different-size pore segments are arranged in series versus in parallel. For real porous media, it may not be straightforward to apply this microscopic definition to compute α, but the conceptual picture may still hold. For example, consider the illustrations in Figure 2-5, which highlight qualitative features of the morphology of porous samples with low, medium, and high accessivities.

Like tortuosity, accessivity should be rigorously defined based on macroscopic observations, as we will present in Chapter 4. Nevertheless, the microscopic definition of α based on our probabilistic framework provides an intuitive starting point for incorporating the concept in continuum descriptions of porous media.

$\alpha \to 0$ $\alpha \approx 0.5$ $\alpha \to 1$

Figure 2-5: Illustrations of samples of hypothetical porous media a trimodal PSD and low, medium, and high accessivities, respectively. Black and white regions correspond to the solid matrix and the pore space, respectively. Reproduced from [1].

Chapter 3

Microscopic theory of capillary pressure hysteresis

In this chapter, we will use the probabilistic framework introduced in Section 2.2 to begin analyzing multiphase flow in porous media. We will define a new concept called the **radius-resolved saturations**, and use it to describe the pore-scale distribution of immiscible fluid phases across pore segments of various sizes. We will then use our probabilistic framework to develop a theory of capillary pressure hysteresis by analyzing quasistatic microscopic fluid redistribution.

3.1 Introduction

For certain simple physical processes in porous media, especially those involving a single fluid phase in the pore space – such as single-phase flow [47, 48] and and heat transfer [49, 50] – simple continuum formulations generally work well, and a rigorous connection between the pore-scale and continuum-scale governing equations can be sought. In comparison, it is considerably more challenging to develop predictive continuum models for processes in porous media involving multiple fluid phases [2, 51, 52, 53, 54, 55, 56, 57, 58, 59]. In terms of connecting any continuum description to pore-scale physics, while it is possible to upscale pore-scale equations by careful averaging [60, 61, 62, 63, 64], the resulting model varies depending on the macroscopic

state variables selected and the scaling laws assumed for the specific applications considered, not to mention that the mechanisms for pore-scale fluid motions are highly complex and are still actively researched [65, 66, 67, 68]. It appears that in formulating continuum models of multiphase flow in porous media, there exists a trade-off between mathematical simplicity and consideration of pore-scale physics.

In this section, we will review some current ideas in the literature on the continuum modeling of multiphase flow in porous media, and discuss pore-scale physical processes that underlie our theory of capillary pressure hysteresis.

3.1.1 Fluid saturations

In Section 2.1, we defined the function $p_s : \Omega \to \{0, 1\}$ in Eq. (2.1) to characterize the exact microstructure of a porous medium; there, $\{\mathbf{x} \in \Omega : p_s(\mathbf{x}) = 1\}$ corresponds to the pore space. In multiphase flow, the pore space may contain several fluid phases. For each phase, say, phase w in two-phase flow, we can likewise define the function:

$$p_w : \Omega \to \{0, 1\} : \mathbf{x} \mapsto \begin{cases} 1 & \text{the point } \mathbf{x} \text{ belongs to phase } w \\ 0 & \text{otherwise,} \end{cases} \tag{3.1}$$

Analogous functions for all fluids present in the pore space fully characterize the pore-scale distribution of fluid phases, which may evolve over time during flow [69]. As with $p_s(\mathbf{x})$, imaging techniques are available for estimating $p_w(\mathbf{x})$ in real porous medium under both static [70, 71] and dynamic conditions [72]. Pore-scale simulations [73, 74, 75] and micromodel experiments [76, 65, 77, 78, 68] can also generate such data (also see Section 7.2).

To describe p_w at the continuum scale, we may define a **saturation** variable for

each fluid phase in an REV (denoted by V in the equation below) surrounding $\mathbf{x}$:

$$s_w(\mathbf{x}) \equiv \frac{\int_V p_w(\mathbf{x})\,\mathrm{d}V}{\int_V p_s(\mathbf{x})\,\mathrm{d}V} = \frac{1}{\phi}\int_V p_w(\mathbf{x})\,\mathrm{d}V, \tag{3.2}$$

which is akin to the definition of porosity in Eq. (2.3), but normalized such that for each $\mathbf{x} \in \Omega$, $s_w(\mathbf{x}) \in [0, 1]$, and that saturations of all phases sum to unity[1]. Similar to how porosity does not fully characterize the pore-space morphology, fluid saturations do not perfectly describe the pore-scale distribution of fluid phases. However, they are found to be useful quantities in virtually all continuum models of multiphase processes in porous media.

3.1.2 Capillary bundle and connectivity effects

In Section 2.1.3, we have highlighted the central role played by local pore dimensions in certain physical processes in porous media. To recapitulate, as far as multiphase flow is concerned, pores with larger radii have higher hydraulic conductances, and host menisci with smaller curvatures, which are associated with smaller equilibrium Laplace pressures.

These phenomena make the PSD an intuitive concept for incorporating elements of pore-space morphology into continuum descriptions of multiphase flow in porous media. The quintessential demonstration of that can be found in the **capillary bundle** model, which conceptualizes the pore space as a bundle of straight capillaries that are directly accessible from the surface of the sample, where the volume fractions of capillaries of different radii are given by the PSD. Because the capillaries are arranged in parallel, they behave independently from one another. In our probabilistic framework, the capillary bundle model may correspond to the following limits:

$$\ell\lambda_1 \to \infty \quad \text{and} \quad \frac{\lambda_z}{\lambda_1} \to 0, \forall z \in \{3, 4, \ldots\} \implies \alpha \to 1, \tag{3.3}$$

[1] e.g., Eq. (1.5) for two-phase flow

so that there is negligible branching and virtually no pore-radius variation along a pore branch, rendering each pore-space instance a constant-radius pore branch. These capillaries behave rather predictably during many pore-scale physical processes, thus promising simple continuum descriptions of the corresponding ensemble of instances.

The simplistic nature of the capillary bundle model draws much criticism [79, 80], while at the same time engendering widespread use in practice, e.g., in the standard laboratory interpretation of mercury intrusion porosimetry data [32] and sorption isotherms [38]. In particular, the capillary bundle model is unable to predict capillary pressure hysteresis[2] due to its neglect of **connectivity effects**, meaning that serial connections between different-radius pore segments are completely absent.

To illustrate, we will derive the capillary pressure–saturation relationship entailed by the capillary bundle model. Consider the process of **primary drainage**, where the nonwetting fluid enters a porous specimen whose pore space is initially filled with the wetting fluid, corresponding to an initial saturation of $s_w = 1$. The pressure in the nonwetting phase is sufficiently low compared to that in the wetting phase at first, e.g., $p_c = 0$, so that a meniscus separating the two phases cannot exist in equilibrium in a capillary of any radius. As we gradually raise p_c, the corresponding equilibrium capillary radius, given by Eq. (2.10) and denoted here by r_c, decreases. Hence, any capillary whose radius is greater than r_c will undergo complete drainage and become filled with the nonwetting fluid. The volume fraction of the pore space filled with the wetting phase is thus equal to the volume fraction of capillaries with radii that are less than r_c, which is given by $F_c \equiv F(r_c)$, or the CDF of the PSD evaluated at the equilibrium capillary radius. That is:

$$s_w = F_c, \tag{3.4}$$

[2]barring other explanations for hysteresis such as **contact-angle hysteresis** [44], which we will consider in the context of mercury porosimetry in Chapter 4

which gives the following p_c–s_w relationship:

$$s_w = F\left(\frac{2\gamma_{wn}\cos\theta_c}{p_c}\right). \tag{3.5}$$

In fact, the capillary bundle model predicts the same, nonhysteretic capillary pressure–saturation relationship as written above during arbitrary drainage–imbibition cycles, as capillaries of all radii are accessible by both fluid phases at all times.

These assumptions are generally not applicable in real porous media, where some different-size pore slices may be arranged in series and hence not accessed completely independently. For example, during primary drainage, pore slices whose radii are larger than F_c at some imposed capillary pressure[3] will not drain if they are preceded by a pore slice that is smaller than F_c, which the invading nonwetting phase cannot enter. This means that, during primary drainage, the saturation of the wetting phase may be higher than the volume fraction of pore slices with radii smaller than F_c, or:

$$s_w \geq F_c, \tag{3.6}$$

and conversely, during **primary imbibition**, the wetting fluid may not be able to imbibe into some pore slices that are smaller than F_c if they are preceded by pore slices larger than F_c, meaning that:

$$s_w \leq F_c. \tag{3.7}$$

Either of the above may be true during arbitrary drainage–imbibition cycles. Thus, the p_c–s_w relationship is generally hysteretic when serial connectivity between different-size pore slices is present – which implies $\alpha < 1$ in our probabilistic framework. This phenomenon, which is often referred to as the **ink-bottle effect** [81, 82, 83, 15], exemplifies the link between pore-space morphology and capillary pressure hysteresis and serves as the basis for our microscopic theory.

[3]Recall from Section 2.1.3 that we may use the CDF of the PSD, F, as a surrogate for relative pore radii.

3.1.3 Continuum models based on saturations

In conventional models of two-phase flow that are widely accepted in practice, saturation is the primary state variable, as we may recall from Chapter 1. Empirical constitutive relationships are ordinarily employed to relate saturation to both capillary pressure and relative permeabilities. Focusing on capillary pressure for the purpose of this chapter, popular formulae include the Brooks–Corey model [84]:

$$s_w = \begin{cases} 1 & p_c \in [0, p_b) \\ (p_b/p_c)^m & p_c \in [p_b, \infty)\,, \end{cases} \tag{3.8}$$

where p_b and λ are model parameters[4], and the van Genuchten model [85]:

$$s_w = \left(\frac{1}{1+(ap_c)^n}\right)^m, \tag{3.9}$$

where a, n, and m are model parameters[5]. Such empirical models do not capture hysteresis, but instead produces a single p_c–s_w curve, which is generally thought to represent primary drainage. Nevertheless, they are widely used in practice for they are often able to fit experimental data well by virtue of having several adjustable model parameters [15].

There are also simple scaling laws that relate the p_c–s_w relationships for closely related porous media. A classical example is the Leverett J-function [86, 87, 88]:

$$J(s_w) = \frac{p_c}{\gamma_{wn}}\sqrt{\frac{k_s}{\phi}}. \tag{3.10}$$

Leverett finds that the $p_c(s_w)$ curves for a number of sands form two branches when plotted as J-functions, one for imbibition and the other for drainage. The form of the scaling law can also be obtained from a dimensional analysis. We note that the

[4]Here, p_b is called the bubbling pressure, which is equal to the lowest value of p_c below which s_w becomes less than unity, and λ is called the pore-size distribution index.

[5]Sometimes the **effective saturation**, which may be given by $s_{we} \equiv (s_w - s_{wi})/(1 - s_{wi})$ during primary drainage, is used in place of s_w, where s_{wi}, referred to as the **irreducible saturation** of the wetting phase, constitutes an additional model parameter.

J-function does not predict the extent of hysteresis, but may be used to extrapolate p_c–s_w data to similar systems. Also, the domain theory of hysteresis also results in scaling laws that predict hysteresis in the p_c–s_w relationships based on primary drainage data [89, 90, 91, 92, 93, 94, 95].

Many other popular continuum constitutive relationships in the literature are expressed in terms of the PSD, conceptualizing the pore space as interconnected "pores" of various sizes and certain shapes, either implicitly or explicitly [96, 97]. The simplest example is the capillary bundle model already discussed in Section 3.1.2, which, as we have noted, does not predict hysteresis in either capillary pressure or relative permeabilities due to its neglect of connectivity effects. Additionally, if one were to interpret the conceptual picture of the capillary bundle in a literal manner, they may conclude that the porous medium that it represent must be highly anisotropic because flow is only allowed in the direction of the bundle [30], which appears unrealistic. In order to address the shortcomings of the capillary bundle model, many have sought its extensions or considered alternative geometrical representations of pore elements. Examples include assuming that the pore radius fluctuates sinusoidally over its axial length [98], approximating the solid matrix as a packing of spheres by utilizing the grain-size distribution [99, 100, 101, 102], treating the appearance of pores as some random stochastic process [54, 103], deriving analytical formulae based on simple percolation models [45, 104, 46, 105], and others [96].

3.1.4 Continuum models based on additional state variables

Let us, for a moment, view hysteresis from a mathematical perspective. Suppose we have a function of two variables, $f : X_1 \times X_2 \to Y$. It follows that for any $x_1 \in X_1, x_2 \in X_2$, we have a unique corresponding $y = f(x_1, x_2) \in Y$. However, for each given $x_1 \in X_1$, there could be several $y \in \{f(x_1, x_2) : x_2 \in X_2\}$; thus, if we were to plot the trajectory of $y \in Y$ versus $x_1 \in X_1$, we would find that the relationship is not unique and possibly history-dependent.

As we have alluded to in Chapter 1, conventional models of multiphase flow in porous media suffer from hysteresis, suggesting that additional macroscopic state

variables may be required to eliminate hysteresis. This is consistent with the physical understanding that saturation alone is unable to fully characterize the pore-scale distribution of fluid phases in the pore space, as we have shown in Section 3.1.1. In this section, we will review additional continuum state variables proposed in the literature for describing multiphase flow in porous media (also see [106]).

To begin with, many authors make the assumption that capillary pressure depends on not only saturation, but also the "rate of saturation", $\partial s_w/\partial t$, or at least its sign, thereby attributing hysteresis to nonequilibrium effects [107, 108, 109, 110, 111].

Others have, on thermodynamic grounds, identified the "specific interfacial area", a_{wn}, or the interfacial area between the wetting and nonwetting phases per unit volume of the porous medium[6], as a physically relevant state variable, and have advocated for its inclusion in continuum models to reduce capillary pressure hysteresis [113, 109, 112, 114, 115]. This hypothesis seems to hold in many but not all cases, as revealed by micromodel experiments [116, 117, 118, 78], lattice-Boltzmann simulations [119], pore-network simulations [120, 121, 122, 123], and analysis [124], while the exact form of any new constitutive relationships required may not be completely clear.

More recently, Hilfer put forth a new class of continuum models for two-phase flow in porous media [125, 126, 127] involving four fluid saturation variables, $\{s_1, s_2, s_3, s_4\}$, as opposed the conventional two, $\{s_w, s_n\}$, for the two fluid phases (in either case, all saturation variables must sum to unity); we have $s_w = s_1 + s_2$ and $s_n = s_3 + s_4$, where s_1 and s_3 correspond to "percolating regions" of the respective fluid phases, and s_2 and s_4 correspond to "non-percolating regions". By differentiating between the contributions of percolating and non-percolating fluid "subphases", Hilfer's model naturally predicts hysteresis as a result of the dynamics of these new state variables. Because the model is not derived from the principles of the microscopic physics, phenomenological assumptions are still required to, say, model the "mass transfer rates" between s_1 and s_2, or s_3 and s_4 – namely, percolating fluid regions becoming non-percolating and vice versa. These assumptions lead to model parameters that

[6]While the specific interfacial areas between w and s and between n and s may also be of interest, some authors argue that the dependencies of p_c on a_{ws} and a_{ns} may be dropped under certain conditions, making a_{wn} the only relevant specific interfacial area [109, 112].

may be difficult to interpret physically, though they can potentially be determined from experiments.

It appears that modeling multiphase flow in porous media at the continuum scale is an inherently difficult problem. It is likely that any continuum model to come in the foreseeable future will not be able to match the performance of pore-scale methods in terms of either predictability or connection to first principles. On the one hand, conventional models continue to dominate continuum simulations of multiphase flow in porous media for practical applications, despite their neglect or empirical treatment of hysteresis. On the other hand, new continuum models, despite having rightly introduced new and physically meaningful state variables so as to naturally predict hysteresis, deviate significantly from conventional models. They involve somewhat abstract constitutive laws with phenomenological constants which lack a clear connection to pore-scale concepts, possibly due to the emphasis placed on reproducing certain macroscopic observations. In this thesis, we would like to identify new physically meaningful concepts that can be readily incorporated into existing continuum models of multiphase flow in porous media to capture hysteresis.

3.2 Our theory

In this section, we will continue to develop our theoretical framework to consider the pore-scale redistribution of fluid phases under capillary forces. Our goal is to characterize the pore-scale distribution of fluid phases at the continuum scale using functions such as p_w that are introduced in Section 3.1.1. The concepts we propose here are general and can in principle be readily extended to systems involving any number of immiscible fluids, though for simplicity, we shall confine our discussion to two-phase systems.

3.2.1 Radius-resolved saturations

We propose the **radius-resolved saturations**, $\psi_w(F)$ and $\psi_n(F)$, to characterize the distribution of fluids across pore slices of different sizes. Among all pore slices

of a particular radius $F_0 = F(r_0)$, by definition, $\psi_w(F_0)$ is the volume fraction of pore slices filled with the wetting phase, and $\psi_n(F_0)$ is the fraction of pores filled with the nonwetting phase. As with conventional saturations, we have $\psi_w(F) + \psi_n(F) = 1, \forall F \in [0, 1]$. The name "radius-resolved saturations" reflects the fact that the conventional saturations are easily recovered by integrating the radius-resolved saturations:

$$s_w = \int_0^1 \psi_w(F)\,\mathrm{d}F, \quad s_n = \int_0^1 \psi_n(F)\,\mathrm{d}F. \tag{3.11}$$

Namely, conventional saturations are simply averaged radius-resolved saturations, weighted by the volume fraction of each pore radius[7].

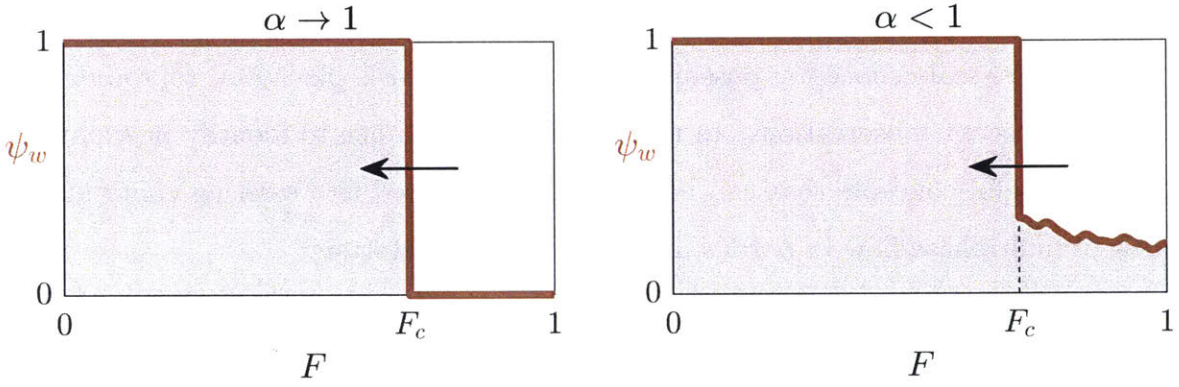

Figure 3-1: Examples of the radius-resolved saturation of the wetting phase, $\psi_w(F)$, at some imposed F_c during quasistatic primary drainage. The shaded and unshaded areas correspond to the conventional saturations of the wetting and nonwetting phases, respectively, following Eq. (3.11). When accessivity is nearly unity (left panel), all pores with radii larger than F_c are accessible by the nonwetting phase and will undergo drainage; when accessivity is less than unity (right panel), although all pores larger than F_c still favor drainage, only a fraction of them ends up draining due to the ink-bottle effect, which is captured by the $\psi_w(F)$ function. Adapted from [1].

In Section 3.1.2, we have shown that, in the limit of the capillary bundle model (which implies $\alpha \to 1$ in our framework), the saturation of the wetting phase is equal to the CDF of the PSD evaluated at the equilibrium capillary radius even during

[7]Alternatively, we could have expressed radius-resolved saturations as functions of pore radius r, i.e., $\psi_w(r)$ and $\psi_n(r)$, which would imply $s_w = \int_0^\infty \psi_w(r)f(r)\,\mathrm{d}r$ and $s_n = \int_0^\infty \psi_n(r)f(r)\,\mathrm{d}r$ because $\mathrm{d}F = f(r)\mathrm{d}r$; also, $\psi_w(r)f(r)$ (or $\psi_n(r)f(r)$) would then be PDF of the distribution of radii of pore slices filled with the wetting (or nonwetting) phase.

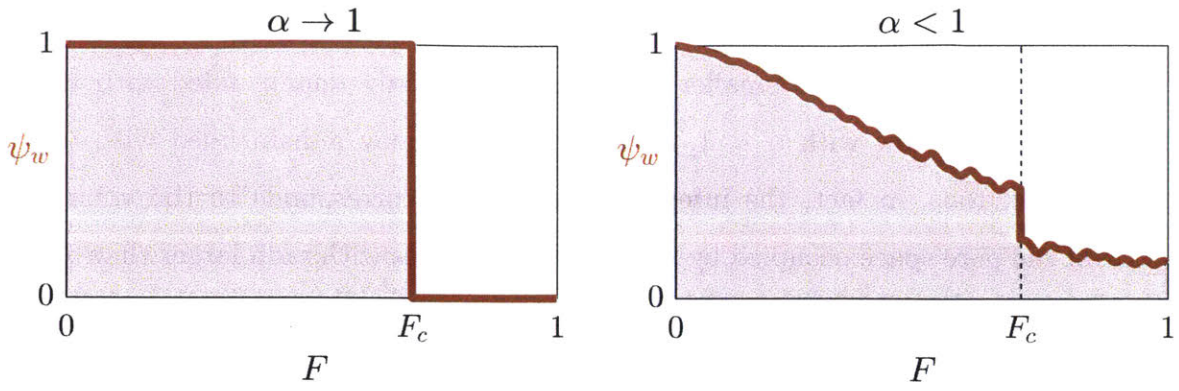

Figure 3-2: Examples of the radius-resolved saturation of the wetting phase, $\psi_w(F)$, at some imposed F_c during arbitrary drainage–imbibition cycles. The shaded and unshaded areas correspond to the conventional saturations of the wetting and nonwetting phases, respectively, following Eq. (3.11). When accessivity is nearly unity (left panel), all pores with radii larger than F_c are occupied by the nonwetting phase, and all smaller pores the wetting phase; when accessivity is less than unity (right panel), both phases may be found in pore slices of each radius due to connectivity effects, which are captured by the $\psi_w(F)$ function. Adapted from [1].

arbitrary drainage–imbibition cycles, i.e., Eq. (3.4). At the pore scale, all pores with radii smaller than F_c will become filled with the wetting phase, and all larger pores the nonwetting phase. This corresponds to the following radius-resolved saturation of the wetting phase:

$$\psi_w(F; F_c) = \begin{cases} 1 & F \leq F_c \\ 0 & F > F_c, \end{cases} \tag{3.12}$$

which, according to Eq. (3.11), gives $s_w = F_c$ and $s_n = 1 - F_c$, as expected. See Figure 3-1.

Conversely, if some serial connectivity between different-size pores is present (which implies $\alpha < 1$ in our framework), then the radius-resolved saturation will generally evolve differently. During primary drainage, we would expect, in general:

$$\psi_w\left(F; F_c\right) = \begin{cases} 1, & F \leq F_c \\ \text{varies between 0 and 1} & F > F_c. \end{cases} \tag{3.13}$$

Since the pore space is saturated with the wetting fluid at the beginning of primary drainage, all pores with radii smaller than F_c will certainly remain filled with the wetting phase, but now with $\alpha < 1$, some larger pores may remain filled with the wetting phase, too. In fact, the integral $\int_{F_c}^{1} \psi_w(F)\,\mathrm{d}F$ corresponds to the volume fraction of the pore space occupied by wetting fluid in pores with radii larger than F_c, which favor drainage yet cannot drain because they are blocked from the nonwetting fluid by pores smaller than F_c. In the context of primary drainage, this quantity is precisely Hilfer's "s_2", or the saturation of the "non-percolating water subphase"[8] [125, 126]. Because $s_2 > 0$, we have $s_w > F_c$ and $s_n < 1 - F_c$, which is clear from Figure 3-1.

Now, consider the general case where a control volume that has undergone a number of arbitrary drainage–imbibition cycles before the capillary pressure is finally brought to p_c. Figure 3-2 depicts the expected $\psi_w(F)$ profiles for porous media with different accessivities. For $\alpha \to 1$, the radius-resolved saturation $\psi_w(F)$ is identical to that during primary drainage (given by Eq. (3.12) and plotted in the left panel of Figure 3-1) because pores of all radii correspond to straight capillaries that are directly accessible by both fluid phases, so that all pores with radii smaller (larger) than F_c are filled with the wetting (nonwetting) phase. There is a one-to-one correspondence between s_w and $\psi_w(F)$, i.e., one can reproduce the radius-resolved saturation function from the conventional saturation at any capillary pressure, which correctly implies that the capillary bundle model does not predict ink-bottle effect–based hysteresis in $p_c(s_w)$.

On the other hand, in a real porous medium with an accessivity lower than unity, $\psi_w(F)$ can acquire nontrivial profiles after arbitrary cycles of drainage and imbibition, which is illustrated in the right panel of Figure 3-2. We see that $\psi_w(F)$ is a better representation of the microscopic state of porous medium than s_w, as the former registers the effects of the flow history on the current pore-scale distribution of fluid phases.

Interestingly, $\psi_w(F)$ may have some loose connection to Hilfer's four saturation

[8] assuming the solid matrix is water-wet, or that "water" refers to the wetting fluid here

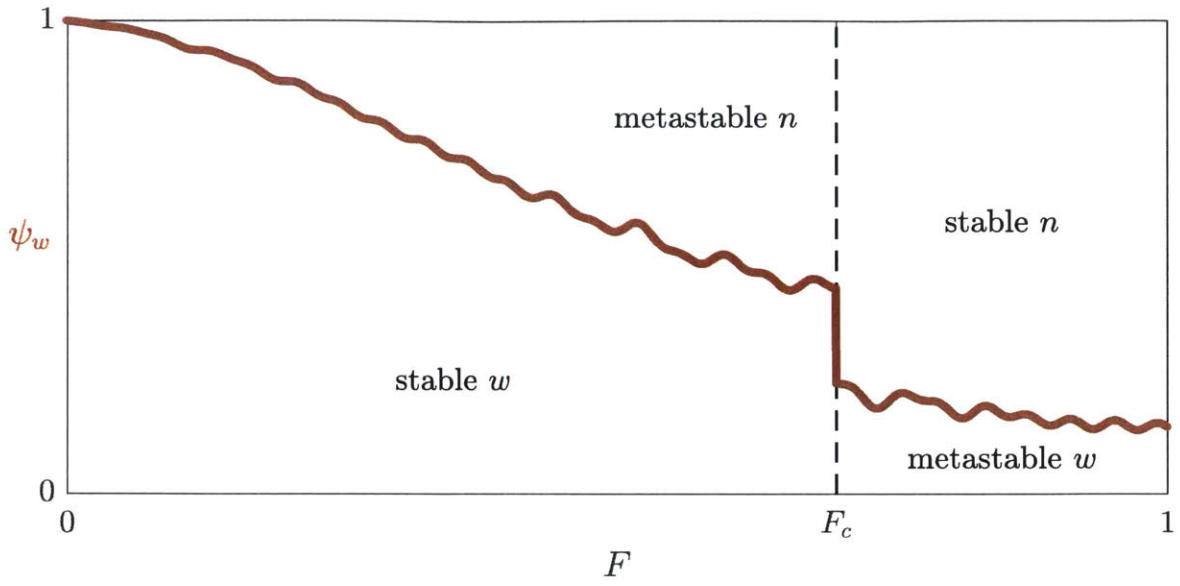

Figure 3-3: The four "quadrants" in the right panel of Figure 3-2, whose areas define four saturation-like variables with distinct physical interpretations. These lumped saturation variables are reminiscent of (but different from) Hilfer's four saturation variables based on percolation, yet lack the precise connection to the PSD found in the radius-resolved saturation profile, $\psi_w(F)$. Adapted from [1].

variables, $s_1, \ldots, s_4$ [125, 126]. We note that in the right panel of Figure 3-2, the $[0,1] \times [0,1]$ area is divided into four "quadrants" by the red $\psi_w(F)$ curve and the vertical dashed line at F_c. By recalling that each point in the shaded (unshaded) area corresponds to a pore filled with the wetting (nonwetting) phase, and that a point to the left (right) of the $F = F_c$ line corresponds to a pore that favors imbibition (drainage), we find it appealing to interpret the areas of the four "quadrants" as follows:

$$\int_0^{F_c} \psi_w(F)\,\mathrm{d}F \text{ (stable } w \text{ phase)} \sim \text{Hilfer's } s_1, \tag{3.14}$$

$$\int_{F_c}^1 \psi_w(F)\,\mathrm{d}F \text{ (metastable } w \text{ phase)} \sim \text{Hilfer's } s_2, \tag{3.15}$$

$$\int_{F_c}^1 1 - \psi_w(F)\,\mathrm{d}F \text{ (stable } n \text{ phase)} \sim \text{Hilfer's } s_3, \tag{3.16}$$

$$\int_0^{F_c} 1 - \psi_w(F)\,\mathrm{d}F \text{ (metastable } n \text{ phase)} \sim \text{Hilfer's } s_4, \tag{3.17}$$

as shown in Figure 3-3.

For instance, the integral in Eq. (3.15) corresponds to the area of the lower-right "quadrant" in Figure 3-3, which gives the volume fraction of pores that are w-filled but have large enough radii to favor drainage at the imposed F_c. We say these pores contain "metastable w phase" because the wetting fluid would have drained out of these pores if they were accessed by mobile menisci. In other words, the wetting phase is trapped in these larger pores that are blocked by smaller pores, and is not truly "stable" – like the wetting fluid in pores with radii smaller than F_c, corresponding to the lower-left quadrant – because it would be spontaneously replaced by the nonwetting phase if the pore were brought in direct equilibrium contact with the nonwetting phase. We note that the four integrals identified in Eq. (3.14)–(3.17) are not identical to Hilfer's definitions of $s_1, \ldots, s_4$, which are based on percolation rather than pore size. For instance, a pore with "stable n phase" is not necessarily percolating to an external reservoir of the nonwetting fluid, and could be part of a trapped ganglion. Nevertheless, it is remarkable that the conventional saturations (s_w and s_n) can be intuitively subdivided into four saturation-like variables in either case. Our framework is different in that it also affords an intuitive and precise connection to the PSD, and, in fact, goes beyond a four-variable description by characterizing the microscopic distribution of fluid phases across a spectrum of pore radii using the function $\psi_w(F)$.

3.2.2 Quasistatic fluid redistribution during primary drainage

Now that we have established the concept of the radius-resolved saturations, which are denoted by $\psi_w(F)$ and $\psi_n(F)$ for two-phase flow, we will analyze quasistatic[9] fluid redistribution at the pore scale using our probabilistic framework introduced in Section 2.2. Our goal is to derive formulae for updating the radius-resolved saturations in response to quasistatic changes in the imposed F_c, where the pore-space accessivity controls the morphology of the pore space. To make our discussions more instructive, we will begin by analyzing the comparatively simpler case of quasistatic primary

[9]meaning that the imposed capillary pressure is varied in infinitesimally small steps, which allows the control volume to reach new metastable states in response

drainage before generalizing the results to arbitrary drainage–imbibition cycles.

During primary drainage, F_c is lowered from 1 to 0, causing s_w to also decrease from 1 to 0. We assume that any drainage that occurs can be attributed to the advancement of menisci into the ensemble of pore-space instances that make up the pore space. We use ω to denote the number of menisci per instance that may contribute to further drainage, and assume $\omega(F_c = 1) = 1$, i.e., there is one meniscus per instance, located at the surface of the control volume, at the beginning of primary drainage. We shall then consider how s_w and ω change in response to differential changes $\mathrm{d}Fc$, which are negative because F_c decreases during drainage.

Since s_w will not change if F_c remains unchanged[10], we deduce that every meniscus must be immediately upstream from a pore slice whose radius is smaller than F_c, which would prevent the nonwetting phase from intruding further into that pore. We say such a meniscus is in the **pinned** state. When F_c is reduced to $F_c + \mathrm{d}F_c$, only menisci that are adjacent to a pore whose size falls in the interval $[F_c + \mathrm{d}F_c, F_c)$ will advance downstream. Thus, the number of menisci per instance that move in response to the differential change in F_c is equal to:

$$\delta\omega_{\mathrm{adv}} = \omega\frac{-\mathrm{d}F_c}{F_c}, \tag{3.18}$$

where the fraction $-\mathrm{d}F_c/F_c$ is the conditional probability that the size of the pore next to the meniscus is in $[F_c + \mathrm{d}F_c, F_c)$, given that it is in $[0, F_c)$.

Next, a meniscus that begins moving in response to $\mathrm{d}F_c$ may experience either of the following two independent events as it travels along the pore axial coordinate:

- The meniscus encounters a pore with a radius smaller than F_c and returns to the pinned state, which occurs according to a homogeneous Poisson point process with a rate parameter of[11]:

$$\lambda_{r_c^-} \equiv \frac{F_c}{\ell}; \tag{3.19}$$

[10] which follows from the premise that F_c changes quasistatically

[11] Recall the definition of ℓ from Section 2.2.2.

- The meniscus encounters a junction (of any coordination number), which occurs according to a homogeneous Poisson point process with a rate parameter of $\lambda_{\mathbb{Z}^+}$ (see Eq. (2.12)).

We denote the mean total displacement of an advancing meniscus and all its descendants by $\langle d \rangle$. It must follow the relation[12]:

$$\langle d \rangle = \frac{1}{\lambda_{r_c^-} + \lambda_{\mathbb{Z}^+}} + \sum_{z \in \mathbb{Z}^+} \left(\frac{\lambda_z}{\lambda_{r_c^-} + \lambda_{\mathbb{Z}^+}} \right) (z-1) \langle d \rangle \tag{3.20}$$

$$\implies \langle d \rangle = \frac{1}{\lambda_{r_c^-} + \sum\limits_{z \in \mathbb{Z}^+} (2-z) \lambda_z} = \frac{1}{F_c/\ell + q/\ell}, \tag{3.21}$$

which we obtain by inserting the definitions of $\lambda_{r_c^-}$ and q found in Eqs. (3.19) and (2.15), respectively.

We have seen that an advancing meniscus can potentially transform into many descendent menisci. The mean number of descendants found in a pore-space instance (including their progenitor), which we denote by $\langle n \rangle$, is given by[13]:

$$\langle n \rangle = \left(\frac{\lambda_{r_c^-}}{\lambda_{r_c^-} + \lambda_{\mathbb{Z}^+}} \right) (1) + \sum_{z \in \mathbb{Z}^+} \left(\frac{\lambda_z}{\lambda_{r_c^-} + \lambda_{\mathbb{Z}^+}} \right) (z-1) \langle n \rangle \tag{3.22}$$

$$\implies \langle n \rangle = \frac{\lambda_{r_c^-}}{\lambda_{r_c^-} + \sum\limits_{z \in \mathbb{Z}^+} (2-z) \lambda_z} = \frac{F_c/\ell}{F_c/\ell + q/\ell} = \frac{F_c}{F_c + q}, \tag{3.23}$$

which we obtain by inserting the definitions of $\lambda_{r_c^-}$ and q found in Eqs. (3.19) and (2.15), respectively.

[12]See Appendix A for a general discussion of the derivation of relations of this form. Here, $1/\left(\lambda_{r_c^-} + \lambda_{\mathbb{Z}^+}\right)$ is the rate at which the advancing meniscus either becomes pinned or encounters a junction. Given that, it may be the case that the meniscus encounters a z-coordinate junction before it gets pinned, which occurs with conditional probability $\lambda_z/\left(\lambda_{r_c^-} + \lambda_{\mathbb{Z}^+}\right)$; this would transform the meniscus into $(z-1)$ independent menisci, each of which independently traverses one of the additional pore branches, and is subject to the same two events described above. Note that in the case of $z = 1$, the meniscus either encounters a dead end or exits the domain of the porous medium, thereby reducing the number menisci responsible for further drainage to zero. On the other hand, if the meniscus gets pinned before it encounters a junction, which occurs with conditional probability $\lambda_{r_c^-}/\left(\lambda_{r_c^-} + \lambda_{\mathbb{Z}^+}\right)$, drainage will stop, resulting in no further increase in $\langle d \rangle$.

[13]Again, see Appendix A for a general discussion of the derivation of relations of this form. Here, an advancing meniscus remains one meniscus in the case that it becomes pinned, but becomes $(z-1)\langle n \rangle$ menisci if it encounters a z-coordinate junction.

Now, we will combine the above results to write a system of Ordinary Differential Equations (ODEs) for $s_n(F_c)$ and $\omega(F_c)$. Firstly, as F_c is reduced to $F_c + \mathrm{d}F_c$, the differential change in the saturation of the wetting phase, $\mathrm{d}s_n$, must satisfy:

$$-\langle c\rangle \mathrm{d}s_w = \delta\omega_{\mathrm{adv}}\langle d\rangle. \tag{3.24}$$

In other words, $-\langle c\rangle \mathrm{d}s_w$ is the differential amount of wetting fluid drained out of each instance in response to $\mathrm{d}F_c$, measured in the unit of the pore axial coordinate. It is equal to the product of the number of advancing menisci per instance, $\delta\omega_{\mathrm{adv}}$, and the mean total displacement of each meniscus, $\langle d\rangle$. Substituting Eqs. (2.15), (3.18), and (3.21) into Eq. (3.24), we obtain an ODE for $s_w\,(F_c)$:

$$\begin{aligned} -\left(\frac{\ell}{q}\right)\mathrm{d}s_w &= \left(\omega\frac{-\mathrm{d}F_c}{F_c}\right)\left(\frac{1}{F_c/\ell + q/\ell}\right) \\ \frac{\mathrm{d}s_w}{\mathrm{d}F_c} &= \frac{\omega}{F_c}\frac{q}{F_c+q}. \end{aligned} \tag{3.25}$$

Secondly, as F_c is reduced to $F_c + \mathrm{d}F_c$, the differential change in the number of menisci per instance available for further mercury intrusion is equal to:

$$\mathrm{d}\omega = \delta\omega_{\mathrm{adv}}\left(\langle n\rangle - 1\right), \tag{3.26}$$

where $(\langle n\rangle - 1)$ gives the net growth in the number of menisci per advancing meniscus. Substituting Eqs. (3.18) and (3.23) into Eq. (3.24), we obtain an ODE for $\omega\,(F_c)$:

$$\begin{aligned} \mathrm{d}\omega &= \left(\omega\frac{-\mathrm{d}F_c}{F_c}\right)\left(\frac{F_c}{F_c+q} - 1\right) \\ \frac{\mathrm{d}\omega}{\mathrm{d}F_c} &= \frac{\omega}{F_c}\frac{q}{F_c+q}. \end{aligned} \tag{3.27}$$

Solving Eqs. (3.25) and (3.27) simultaneously, subject to $s_w(F_c = 1) = 1$ and

$\omega(F_c = 1) = 1$, we obtain the following solutions[14]:

$$s_w(F_c) = \omega(F_c) = 1 - \frac{q\,(1 - F_c)}{F_c + q} = 1 - \frac{\alpha(1 - F_c)}{(1 - \alpha)F_c + \alpha}. \tag{3.28}$$

Eq. (3.28) is our formula for the $s_w\,(F_c)$ relationship during primary drainage, where the accessivity, α, serves as a model parameter for controlling connectivity effects[15]. The limit of the formula as $\alpha \to 1$:

$$\lim_{\alpha \to 1} s_w(F_c) = 1 - \lim_{\alpha \to 1} \frac{\alpha(1 - F_c)}{(1 - \alpha)F_c + \alpha} = F_c, \tag{3.29}$$

coincides with the prediction of the capillary bundle model given by Eq. (3.4).

We may write $s_w\,(F_c)$ for quasistatic primary imbibition by simply replacing F_c with $(1 - F_c)$ and s_w with $(1 - s_w)$ in Eq. (3.28), which gives:

$$s_w(F_c) = \frac{\alpha F_c}{(1 - \alpha)(1 - F_c) + \alpha}, \tag{3.30}$$

where exactly the same reasoning used to derive Eq. (3.30) applies[16], except that F_c is now quasistatically raised instead of lowered, causing imbibition into increasingly larger pores and hence increasing s_w. Setting $\alpha \to 1$ in Eq. (3.30) similarly recovers $s_w(F_c) = F_c$, or the capillary bundle limit found in Eq. (3.4).

Figure 3-4 shows the $s_w\,(F_c)$ relationship for both quasistatic primary drainage and quasistatic primary imbibition, corresponding to Eqs. (3.28) and (3.30), respectively, for porous media of low, medium, and high accessivities.

As $\alpha \to 1$, both the drainage and imbibition curves tend toward the $s_w(F_c) = F_c$ line (given by Eq. (3.4)), and capillary pressure hysteresis is completely absent.

---

[14]We integrate Eq. (3.27) as follows: $\int_1^{\omega} \frac{\mathrm{d}\hat{\omega}}{\hat{\omega}} = \int_1^{F_c} \left(\frac{1}{\hat{F}} - \frac{1}{\hat{F}+q}\right) \mathrm{d}\hat{F} \implies \ln\omega = \ln F_c - \ln\left(\frac{F_c+q}{q+1}\right) \implies \omega(F_c) = \frac{(q+1)F_c}{F_c+1} = 1 - \frac{q(1-F_c)}{F_c+q}$. On the other hand, comparing Eqs. (3.25) and (3.27), we find: $\frac{\mathrm{d}s_w}{\mathrm{d}F_c} = \frac{\mathrm{d}\omega}{\mathrm{d}F_c} \implies \frac{\mathrm{d}s_w}{\mathrm{d}\omega} = 1 \implies s_w(F_c) = \omega(F_c)$.

[15]The solution for ω, while not central to our microscopic theory of capillary pressure hysteresis, may be useful as an indicator of the specific interfacial area between the two immiscible fluid phases.

[16]Note that by this simply analogy with primary drainage, Eq. (3.30) will not predict entrapment of the nonwetting phase during imbibition, which is due to other pore-scale mechanisms such as snap-off [65] unaccounted for in this simple analysis.

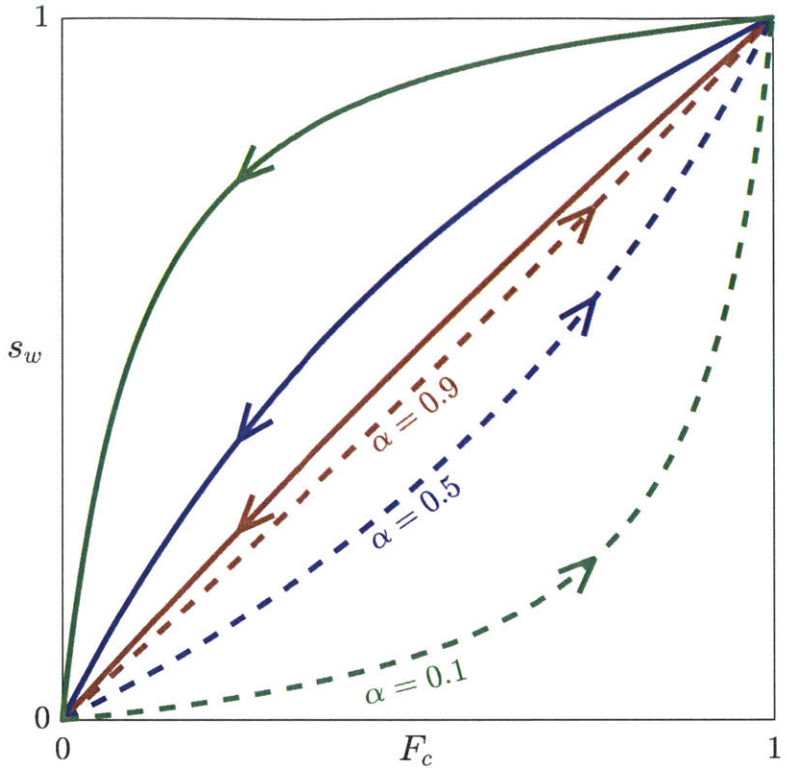

Figure 3-4: Plots of $s_w(F_c)$ for quasistatic primary drainage (solid curves, given by Eq. (3.28)) and quasistatic primary imbibition (dashed curves, given by Eq. (3.30)) for $\alpha = 0.1$ (green curves), $\alpha = 0.5$ (blue curves), and $\alpha = 0.9$ (red curves). The area of the hysteresis loop between the primary drainage and primary imbibition curves decreases as α increases. In the limit of $\alpha \to 1$, we expect to recover $s_w(F_c) = F_c$ for both primary drainage and primary imbibition, which is consistent with the prediction of the capillary bundle model, given by Eq. (3.4). Adapted from [1].

This is a result of different-size pores becoming overwhelmingly arranged in parallel, which is the case in the capillary bundle model. When $\alpha < 1$, serial connectivity between different-size pores render $s_w > F_c$ for all F_c except the end points during primary drainage (as seen in Eq. (3.6)), and $s_w < F_c$ for all F_c except the end points during primary imbibition (as seen in Eq. (3.7)). This widens the hysteresis loop between the drainage and imbibition curves, leading to more prominent hysteresis. Connectivity effects become the strongest as $\alpha \to 0$, which corresponds to highly serial connections between different-size pores. Primary drainage does not occur to an appreciable extent when F_c is lowered at first because most larger pores are only accessible through smaller ones. As F_c approaches zero, a larger fraction of pores

become penetrable, resulting in a rapid drop in s_w, which is reminiscent of a 1-D critical percolation transition [45, 46]. The primary imbibition curves mirror these behaviors for increasing F_c.

We note that for quasistatic primary drainage, it is possible to algebraically derive Eq. (3.28) without constructing ODEs. Instead of analyzing how s_w responds to differential changes in F_c, we can lower F_c from an initial value of 1 to its final value directly, and consider the independent displacements of all advancing menisci at once. Menisci pinned at pores whose radii falls within $(F_c, 1]$ will begin advancing as a result. The fraction of pore-space instances where this occurs is given by:

$$\Delta\omega_{\text{adv}} = 1 - F_c. \tag{3.31}$$

We have already derived the mean displacement of an advancing meniscus that becomes pinned at a rate of F_c/ℓ; the result is given by Eq. (3.21). The amount of drainage in response to the abrupt lowering of F_c is thus equal to[17]:

$$\langle c \rangle s = \Delta\omega_{\text{adv}} \langle d \rangle. \tag{3.32}$$

Substituting Eqs. (2.15), (3.31), and (3.21) into Eq. (3.32) gives Eq. (3.28) again. Eq. (3.30) can also be similarly derived.

We would now like to express the above results in terms of radius-resolved saturations. Based on the our probabilistic framework, during primary drainage, we expect the radius-resolved saturation of the wetting phase to take the following form:

$$\psi_w(F; F_c) = \begin{cases} 1 & F \leq F_c \\ \psi_0(F_c) & F > F_c, \end{cases} \tag{3.33}$$

which is a special case of Eq. (3.13) where pores that are larger in radius than F_c are all filled to the same extent because they are effectively indistinguishable to an advancing meniscus, denoted here by ψ_0, while smaller pores all remain filled exclusively with

[17] cf. Eq. (3.24) for the differential lowering of F_c

the wetting phase. Comparing with Eq. (3.28)[18], we obtain the following formulae for updating $\psi_w(F)$ in response to quasistatic changes in F_c:

$$\psi_w(F;F_c) = \begin{cases} 1 & F \le F_c \\ 1-\alpha/\left[(1-\alpha)F_c+\alpha\right] & F > F_c. \end{cases} \tag{3.34}$$

Similarly, for primary imbibition, we find:

$$\psi_w(F;F_c) = \begin{cases} \alpha/\left[(1-\alpha)(1-F_c)+\alpha\right] & F \le F_c \\ 0 & F > F_c, \end{cases} \tag{3.35}$$

which can be obtained by ostensibly exploiting the symmetry between the two fluid phases in our framework, i.e., replacing F_c with $(1-F_c)$, F with $(1-F)$, and ψ_w with $(1-\psi_w)$ in Eq. (3.34). The radius-resolved saturations predicted by Eqs. (3.34) and (3.35) are shown in Figures 3-5 and 3-6, respectively, for high, moderate, and low accessivities.

3.2.3 Quasistatic fluid redistribution during arbitrary drainage–imbibition cycles

Having analyzed primary drainage and primary imbibition, we can generalize the above results to describe arbitrary quasistatic drainage–imbibition cycles using radius-resolved saturation. Suppose a porous sample acquires a certain $\psi_w(F;F_c)$ after begin subject to arbitrary drainage and imbibition steps. We are interested in predicting changes in $\psi_w(F;F_c)$ from its current state for quasistatic changes in F_c. Specifically, we will modify Eqs. (3.34) and (3.35) by considering how general drainage and imbibition compare with their primary counterparts.

The first point to consider is that, under quasistatic conditions, pores with radii smaller (or larger) than F_c may only undergo imbibition (or drainage), respectively,

[18]Integrating Eq. (3.33) and comparing with Eq. (3.28), we write: $F_c + \int_{F_c}^{1} \psi_0(F_c)\,\mathrm{d}F = 1 - \frac{\alpha(1-F_c)}{(1-\alpha)F_c+\alpha} \implies F_c + (1-F_c)\psi_0(F_c) = 1 - \frac{\alpha(1-F_c)}{(1-\alpha)F_c+\alpha} \implies \psi_0(F_c) = 1 - \frac{\alpha}{(1-\alpha)F_c+\alpha}$.

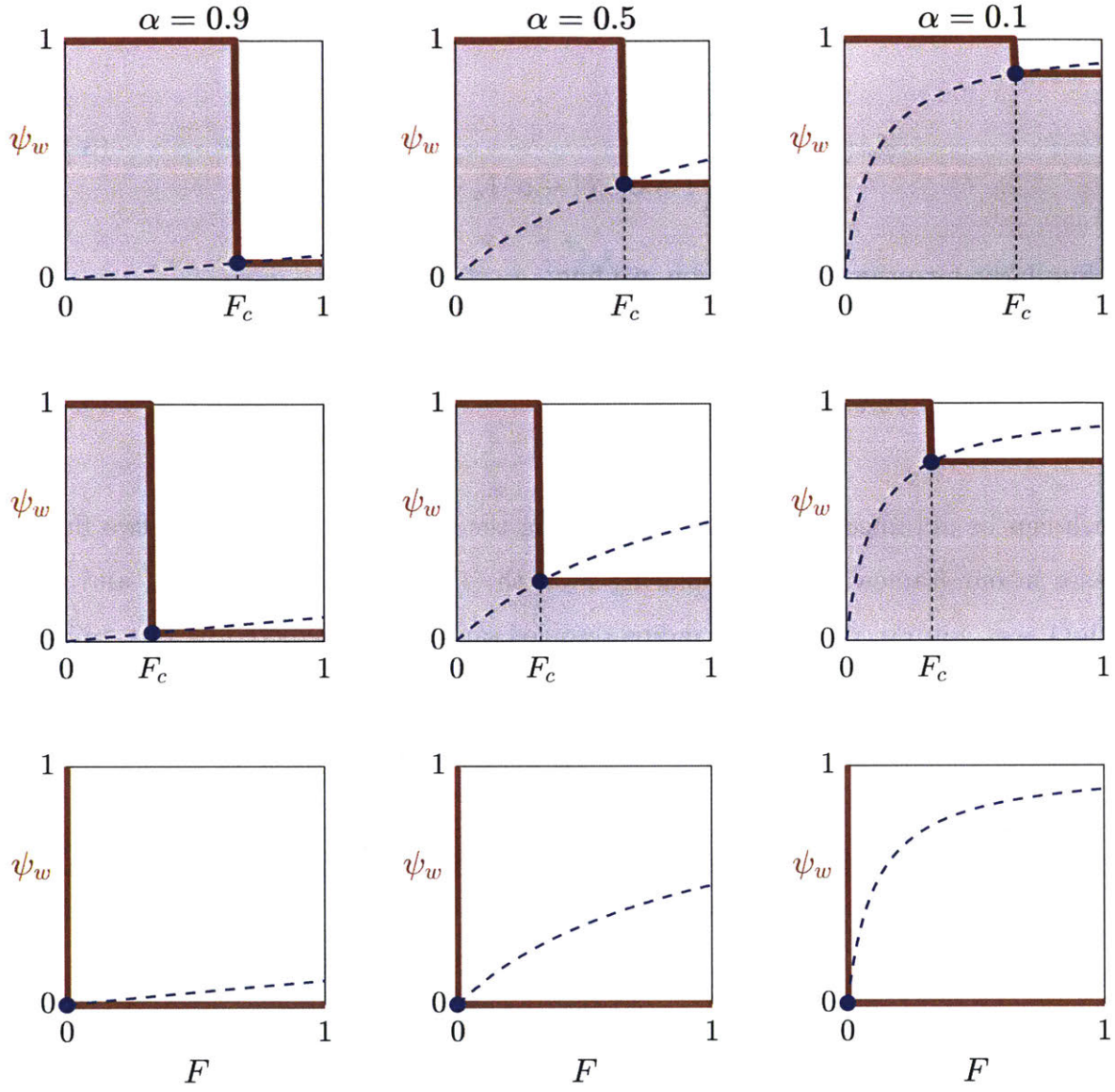

Figure 3-5: Evolution of the radius-resolved saturation of the wetting phase, $\psi_w(F)$, during quasistatic primary drainage, according to Eq. (3.34). The shaded and unshaded areas correspond to the conventional saturations of the wetting and nonwetting phases, respectively, following Eq. (3.11) and corresponding to the solid curves in Figure 3-4. The blue dashed curve represents the trajectory of $1-\alpha/\left[(1-\alpha)F_c+\alpha\right]$ versus F_c. The left, middle, and right columns correspond to $\alpha = 0.9$, $\alpha = 0.5$, and $\alpha = 0.1$. During primary drainage, all nonwetting fluid remains "stable" according to the categorization scheme in Figure 3-3, but "metastable" wetting fluid occurs in pores larger than F_c due to the connectivity effects, whose amount increases as α becomes lower. Adapted from [1].

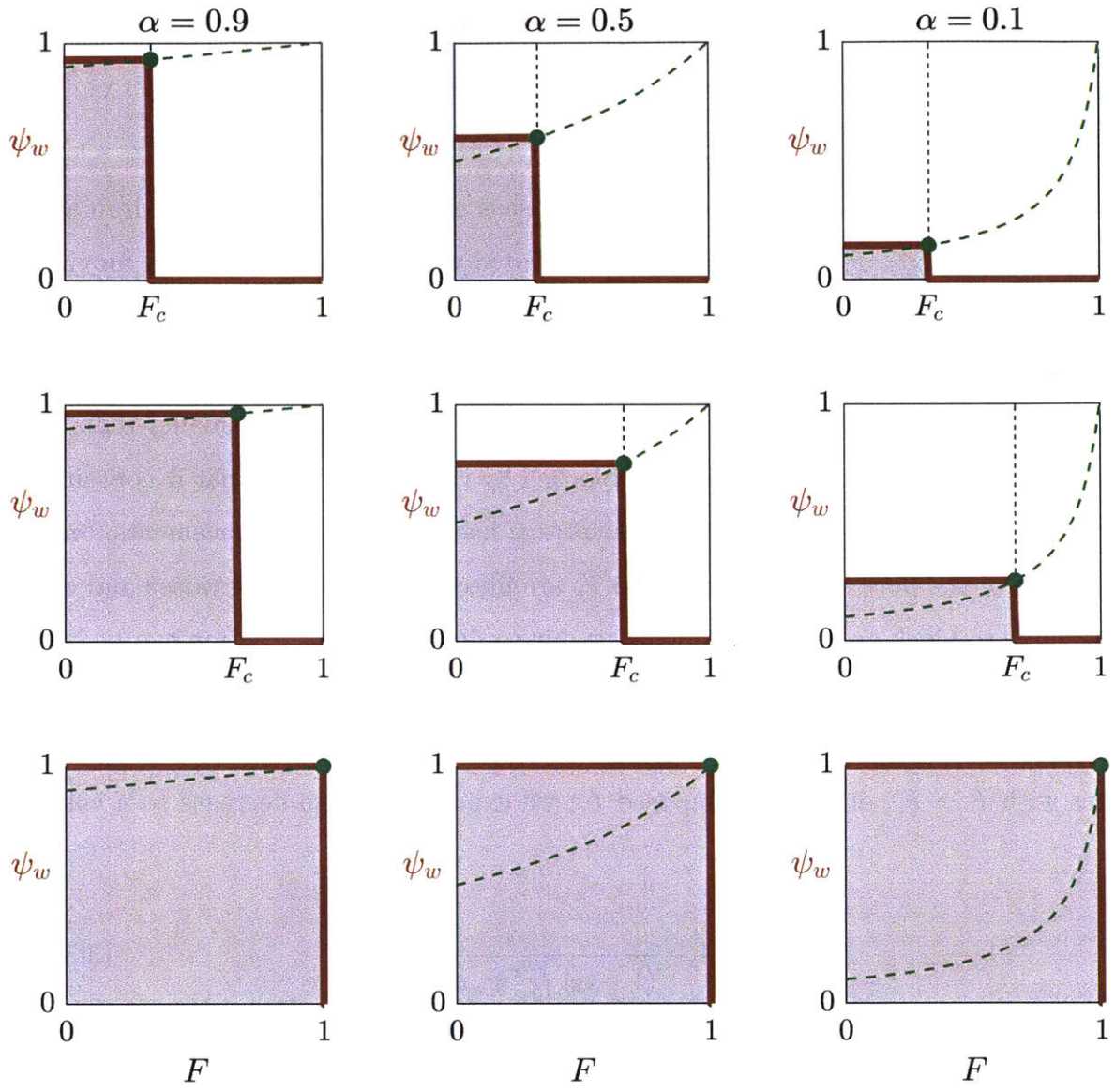

Figure 3-6: Evolution of the radius-resolved saturation of the wetting phase, $\psi_w(F)$, during quasistatic primary imbibition, according to Eq. (3.35). The shaded and unshaded areas correspond to the conventional saturations of the wetting and nonwetting phases, respectively, following Eq. (3.11) and corresponding to the dashed curves in Figure 3-4. The green dashed curve represents the trajectory of $\alpha/\left[(1-\alpha)(1-F_c)+\alpha\right]$ versus F_c. The left, middle, and right columns correspond to $\alpha = 0.9$, $\alpha = 0.5$, and $\alpha = 0.1$. During primary imbibition, all wetting fluid remains "stable" according to the categorization scheme in Figure 3-3, but "metastable" nonwetting fluid occurs in pores smaller than F_c due to the connectivity effects, whose amount increases as α becomes lower. Adapted from [1].

due to local capillary equilibria. Thus, when and only when the imposed F_c changes, $\psi_w(F)$ may only increase or remain unchanged for any $F \leq F_c$, and may only decrease or remain unchanged for $F > F_c$. These observations are consistent with Eqs. (3.28) and (3.30), respectively.

The second point concerns the rate of meniscus pinning. In our primary drainage formula, Eq. (3.34), F_c is thought to be associated with the rate at which a moving meniscus becomes "pinned" – see Eq. (3.19). Since all pores with $F \leq F_c$ are occupied by the wetting phase during primary drainage (as we demonstrated in Eqs. (3.13) and (3.34)), a moving meniscus that encounters a pore slice with a radius smaller than F_c during primary drainage will indeed be blocked by the wetting fluid that it contains. However, in a control volume with an arbitrary history of fluid displacements, only a fraction of the pore slices smaller than F_c are filled with the wetting phase and are hence able to block an advancing meniscus during drainage. This fraction can be calculated given the current $\psi_w(F)$ from the definite integral in Eq. (3.14), which would replace F_c to describe the true rate of pinning of advancing menisci. Accordingly, for pores with $F > F_c$, at a newly imposed F_c, we expect $\psi_w(F)$ to decrease to a value of:

$$\psi_{w,\mathrm{dr}} = 1 - \frac{\alpha}{(1-\alpha)\int_0^{F_c} \psi_w \, \mathrm{d}F + \alpha}. \tag{3.36}$$

Likewise, for quasistatic imbibition starting from an arbitrary $\psi_w(F)$, we expect pores with $F \leq F_c$ to potentially acquire higher values of $\psi_w(F)$ given by:

$$\psi_{w,\mathrm{im}} = \frac{\alpha}{(1-\alpha)\int_{F_c}^{1} (1-\psi_w) \, \mathrm{d}F + \alpha}, \tag{3.37}$$

where, the definite integral, as given by Eq. (3.16), represents the fraction of pore segments that are larger than F_c and filled with the nonwetting phase, and, likewise, replaces $(1 - F_c)$ in Eq. (3.35), which would be the value of the definite integral for primary imbibition.

Lastly, we combine the above results to arrive at an algebraic formula for updating

the radius-resolved saturation of the wetting phase in response to quasistatic capillary pressure variations during arbitrary drainage–imbibition scanning cycles:

$$\psi_w\left(F;F_c\right)=\begin{cases}\max\left\{\psi_w,\psi_{w,\mathrm{im}}\right\}=\max\left\{\psi_w,\frac{\alpha}{(1-\alpha)\int_{F_c}^{1}(1-\psi_w)\,\mathrm{d}F+\alpha}\right\} & F\leq F_c\\ \min\left\{\psi_w,\psi_{w,\mathrm{dr}}\right\}=\min\left\{\psi_w,1-\frac{\alpha}{(1-\alpha)\int_{0}^{F_c}\psi_w\,\mathrm{d}F+\alpha}\right\} & F>F_c,\end{cases}\tag{3.38}$$

where $\psi_{w,\mathrm{dr}}$ and $\psi_{w,\mathrm{im}}$ are given by Eqs. (3.36) and (3.37), respectively. As we vary p_c and hence F_c quasistatically, $\psi_{w,\mathrm{dr}}$ and $\psi_{w,\mathrm{im}}$ change correspondingly, which indicate the degree to which pores larger and smaller in radius than F_c can undergo drainage and imbibition, respectively, based on the pore-space accessivity, α. We update $\psi_w(F)$ at the new F_c by comparing its previous value at each F with either $\psi_{w,\mathrm{dr}}$ or $\psi_{w,\mathrm{im}}$, depending on whether $F>F_c$ or $F\leq F_c$. That is, since pores larger than F_c may only undergo drainage under quasistatic conditions, ψ_w for any $F>F_c$ may only decrease from its previous value, without becoming less than $\psi_{w,\mathrm{dr}}$, which is the lower bound for the extent of drainage based on accessivity; on the other hand, pores smaller than F_c may only undergo imbibition, so ψ_w for any $F\leq F_c$ may only increase, but never exceeding an upper bound of $\psi_{w,\mathrm{im}}$.

Eq. (3.38) simplifies to Eqs. (3.34) and (3.35) for primary drainage and primary imbibition, respectively. Taking primary drainage for example, initially we have $\psi_w(F)=0,\forall F\in[0,1]$ when the pore space is filled exclusively with the wetting phase in pore slices of all radii, and the capillary pressure is its minimum value, or $F_c=1$. As we reduce F_c from 1 to 0, ψ_w for any $F\leq F_c$ must remain at 0, while ψ_w for $F>F_c$ readily decreases to $\psi_{w,\mathrm{dr}}$, which itself increases as F_c decreases according to Eq. (3.36), where the definite integral simply evaluates to F_c. Consequently, we recover the simpler result given by Eq. (3.34).

To illustrate, we apply Eq. (3.38) to a drainage–imbibition scanning cycle where F_c is varied quasistatically as follows: starting at $F_c=1$, it is lowered to $2/6$, then raised to $5/6$, then lowered to $1/6$, then raised to $5/6$, then lowered to $2/6$ and subsequently to 0. The evolution of the radius-resolved saturation of the wetting phase as well as that of the corresponding convention saturation are shown in Figure 3-7 for high,

moderate, and low accessivities. We see that our model inherently predicts hysteresis in the p_c–s_w relationship as a result of the evolution of $\psi_w(F)$, with α controlling the amount of hysteresis present.

We would like to note that the key formulae that we have derived in this chapter can also be expressed in terms of the conventional and radius-resolved saturations of the nonwetting phase. The formula for updating the radius-resolved saturation of the nonwetting phase during arbitrary drainage–imbibition scanning cycles becomes[19]:

$$\psi_n\left(F;F_c\right)=\begin{cases}\min\left\{\psi_n,\psi_{n,\mathrm{im}}\right\}=\min\left\{\psi_n,1-\frac{\alpha}{(1-\alpha)\int_{F_c}^{1}\psi_n\,\mathrm{d}F+\alpha}\right\} & F\leq F_c\\ \max\left\{\psi_n,\psi_{n,\mathrm{dr}}\right\}=\max\left\{\psi_n,\frac{\alpha}{(1-\alpha)\int_{0}^{F_c}(1-\psi_n)\,\mathrm{d}F+\alpha}\right\} & F>F_c.\end{cases}\tag{3.39}$$

During quasistatic primary drainage where $\psi_n\left(F\right)=1,\forall F\in[0,1]$ initially, the conventional saturation of the nonwetting phase is given by[20]:

$$s_n(F_c)=\frac{\alpha(1-F_c)}{(1-\alpha)F_c+\alpha},\tag{3.40}$$

and for primary imbibition, we have[21]:

$$s_n(F_c)=1-\frac{\alpha F_c}{(1-\alpha)(1-F_c)+\alpha}.\tag{3.41}$$

In the limit of $\alpha\to 1$, both Eqs. (3.40) and (3.41) become[22]:

$$s_n(F_c)=1-F_c,\tag{3.42}$$

which holds for arbitrary drainage–imbibition cycles as well, since Eq. (3.39) simplifies

[19] cf. Eq. (3.38)
[20] cf. Eq. (3.28)
[21] cf. Eq. (3.30)
[22] cf. Eq. (3.4)

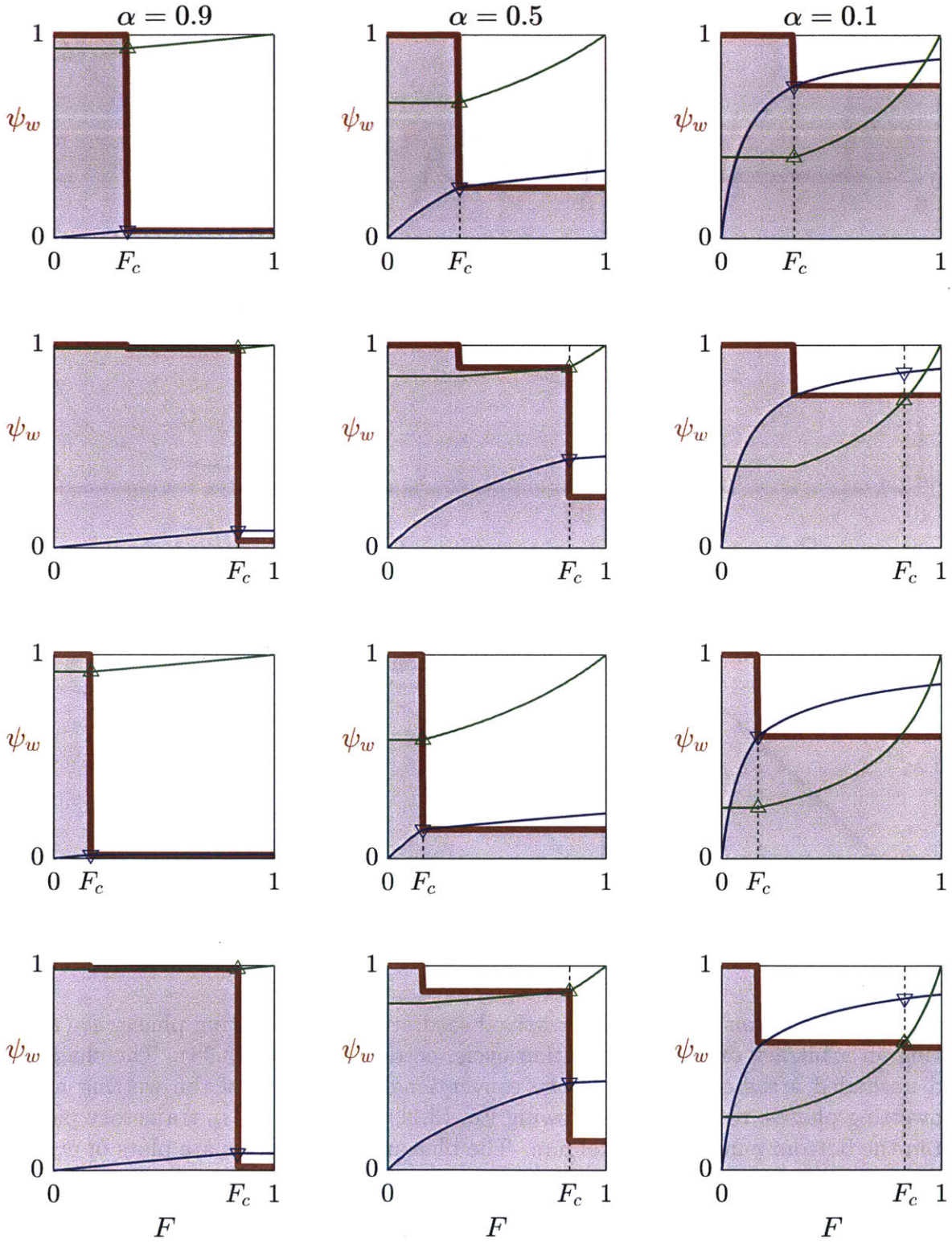
$\alpha = 0.9$
$\alpha = 0.5$
$\alpha = 0.1$
ψ_w
1
0
F_c
F

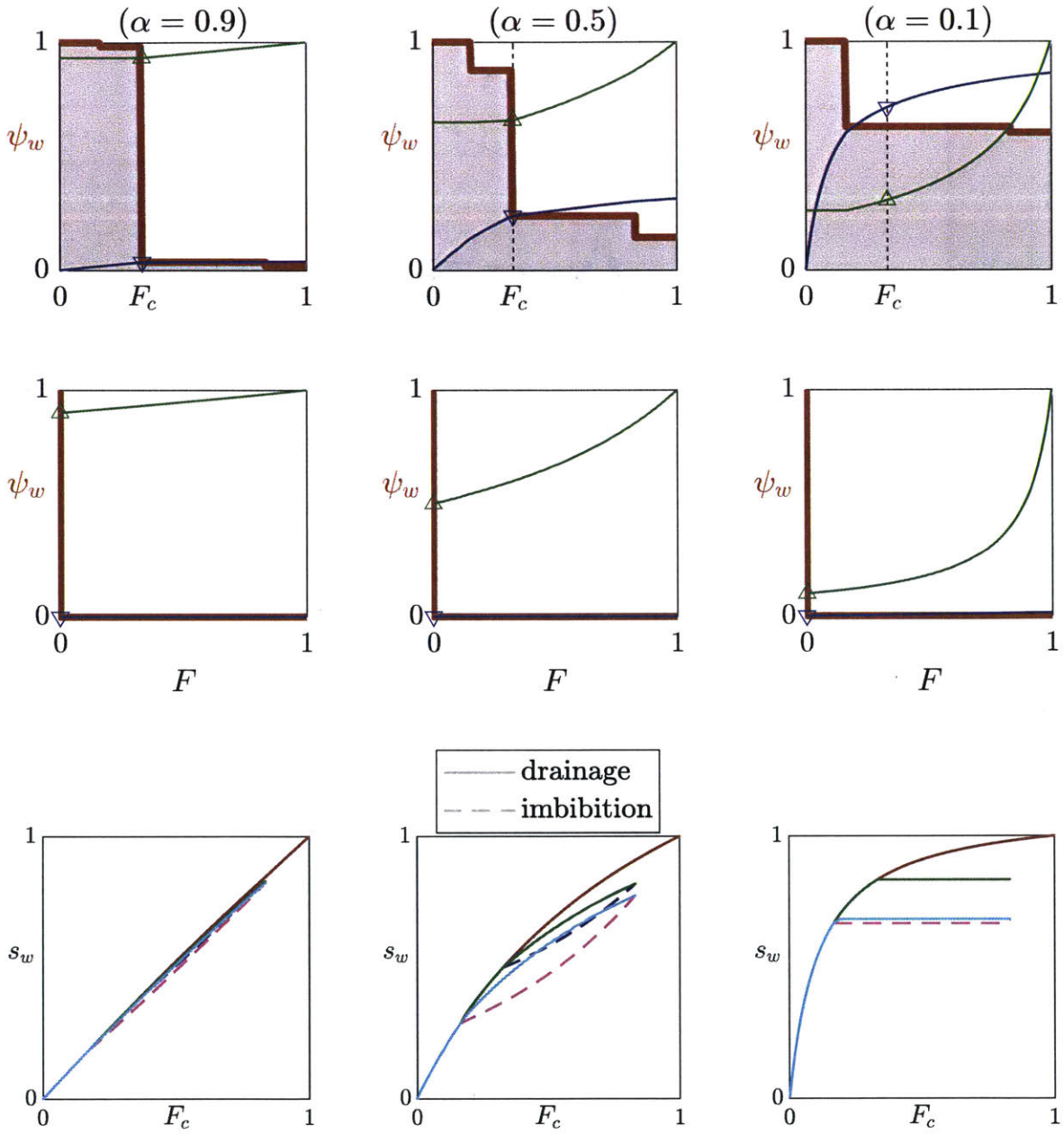

Figure 3-7: Evolution of the radius-resolved saturation of the wetting phase, $\psi_w(F)$, during an arbitrary drainage–imbibition cycle, according to Eq. (3.38). The shaded and unshaded areas correspond to the conventional saturations of the wetting and nonwetting phases, respectively, following Eq. (3.11), with the F_c–s_w trajectory plotted in the bottom panel of each column. The blue and green curves are plots of $\psi_{w,\mathrm{dr}}$ and $\psi_{w,\mathrm{im}}$ versus F_c evaluated using the current $\psi_w(F)$, which are given by Eqs. (3.36) and (3.37), respectively, with their values at $F = F_c$ marked with an upward-pointing and a downward-pointing triangle, respectively. The left, middle, and right columns correspond to $\alpha = 0.9$, $\alpha = 0.5$, and $\alpha = 0.1$. In general, the lower α is, the more "metastable" fluids are produced due to meniscus pinning, as per our categorization scheme in Figure 3-3. Adapted from [1].

to[23]:

$$\psi_n(F; F_c) = \begin{cases} 0 & F \leq F_c \\ 1 & F > F_c, \end{cases} \tag{3.43}$$

whose definite integral over $F \in [0, 1]$ equals $(1 - F_c)$.

[23]cf. Eq. (3.43)

Chapter 4

Application to mercury cyclic porosimetry

Before integrating our microscopic theory of capillary pressure hysteresis into simulations of multiphase flow in porous media, we would like to take a moment to consider its application to **mercury porosimetry** in this chapter. The reason is twofold: on the one hand, our simple algebraic formulae for quasistatic primary drainage and imbibition, Eqs. (3.40) and (3.41), can be readily adapted to improve the interpretation of mercury porosimetry data, even without the explicit use of radius-resolved saturations; on the other hand, as we have mentioned in the closing remarks of Chapter 2, we would like to establish a standard method of measuring pore-space accessivity based on macroscopic experimental observations, and the results in this chapter seem to suggest that mercury porosimetry could be that experimental method.

We will begin this chapter by introducing the experimental technique of mercury porosimetry, as well as the various ways it is modeled in the literature. We will then propose our approaches to conducting mercury porosimetry measurements and interpreting the resulting data based on an extension of our microscopic theory of capillary pressure hysteresis presented in Chapter 3. We will then apply our theory to a set of experimental measurements to demonstrate the determination of the pore-space accessivity and the PSD from mercury cyclic porosimetry.

4.1 Introduction

Mercury porosimetry is a standard characterization technique that is routinely used to infer a number of properties of porous materials, including the porosity, the specific surface area, and the PSD. The sample, whose pore space is first evacuated, is immersed in mercury. As the applied pressure in mercury, p, is gradually raised, an increasing volume of mercury, V, penetrates into the vacuum that pervades the pore space of the sample; this step is known as **mercury intrusion** or **pressurization**. After p reaches the maximum desired value, a subsequent **mercury extrusion** or **depressurization** step is sometimes carried out, which involves the gradual lowering of p. The pressure–volume relationship is generally hysteretic, meaning that the p–V trajectories during intrusion and extrusion do not coincide. The reader is referred to a great number of reviews [128, 129, 130, 131, 132, 133, 44] for the diverse experimental protocols and applications of mercury porosimetry.

The method of mercury porosimetry was first conceived by Washburn in 1921 [32], before it was realized and subsequently improved upon by others [33, 34, 35, 36]. Washburn noted that the pressure required to force mercury into a (cylindrical) capillary pore is related to its radius r by:

$$p = \frac{-2\gamma \cos\theta}{r}, \tag{4.1}$$

where γ is the surface tension of mercury[1], and θ is the contact angle as measured in the mercury phase, which is greater than $\pi/2$ in most systems, making mercury the nonwetting phase and the vacuum the "wetting phase". Eq. (4.1) readily follows from Eq. (2.10) by recognizing that the pressure of a vacuum is approximately zero[2], and that the contact angles in the wetting and nonwetting phases are supplementary. Referred to as the **Washburn equation** in the mercury porosimetry literature, Eq. (4.1) expresses the condition for capillary equilibrium in a single straight cylin-

[1]There may be some uncertainty in the value of γ in Eq. (4.1), although a value of $\gamma = 0.485\ \mathrm{N\ m^{-1}}$ at room temperature is generally accepted [130, 132].

[2]The vapor pressure of mercury under typical experimental conditions of mercury porosimetry [134] is many orders of magnitudes lower than the pressures applied to the mercury phase.

drical pore, and serves as the theoretical basis for determining PSDs in the standard interpretation of mercury intrusion measurements, which associates the differential volume of mercury that penetrates into the sample near pressure p with pores whose radii are near the corresponding r calculated from Eq. (4.1).

The chief assumption in the standard interpretation is that the pore space may be conceptualized as a parallel bundle of straight cylindrical[3] capillaries that are directly accessible by the mercury surrounding the sample [131, 79]; in other words, we are assuming that Eq. (3.42) holds during mercury intrusion – or primary drainage, borrowing terminologies from Chapter 3. However, as we have examined at length in Section 3.1.2, it is possible that some pores are only reachable from the outer surface of the sample via pores of dissimilar sizes, which, if smaller, would block mercury intrusion into pores that the Washburn equation would predict to be penetrable – these are referred to as "ink-bottle pores" [131, 133], "throats" [130, 132], "necks" [128], and other terminologies in the mercury porosimetry literature. The ink-bottle effect is thought to be responsible for the hysteresis commonly observed between mercury intrusion and extrusion curves [130, 45, 131, 132, 133]. Also, when only the intrusion curve is used to compute the PSD in the standard interpretation using Eq. (4.1), the result may be biased toward smaller pores [131, 79]. This is because, in reality, we have $s_n \leq 1 - F_c$ during primary drainage (cf. Eq. (3.42)), so s_n may be an underestimator of the volume fraction of pores with radii larger than that predicted by the Washburn equation. An common alternative view is that the radius distribution calculated from mercury intrusion data corresponds to only the "pore throats", whereas that calculated from extrusion measurements corresponds to only the complementary "pore bodies" [128, 132], so that an intrusion–extrusion experiment results in two PSDs associated with the same porous specimen.

Aside from connectivity effects, hysteresis in porosimetry measurements is also attributed to a phenomenon known as **contact-angle hysteresis**[4] [130, 131, 132, 133,

[3]Some authors argue that cylindrical pore shapes may poorly represent pore geometries found in real porous media [132], and should thus be regarded as "effective" values [129, 130] – recall our assessment of this matter in Section 2.2.

[4]aka. the raindrop effect [2]

44]. That is, θ in Eq. (4.1) may take on different values during intrusion (known as the **advancing contact angle**, θ_{intr}) and extrusion (known as the **receding contact angle**, θ_{extr}), in addition to any variability from material to material. Both values are referred to as **dynamical contact angles** to contrast with their static counterpart. It is observed that the contact angle measured in the mercury phase may be lower during extrusion than during intrusion [44]:

$$\theta_{\text{intr}} \geq \theta_{\text{extr}} \geq 90^{\circ}, \tag{4.2}$$

while the static contact angle may lie somewhere in between θ_{intr} and θ_{extr} [2]. According to Eq. (4.1), contact-angle hysteresis would alter the pore-scale capillary equilibrium condition: pores of a certain radius would correspond to a lower equilibrium capillary pressure during extrusion than during intrusion. Some authors claim that contact-angle hysteresis may be sufficient for explaining the hysteresis in mercury porosimetry in at least some cases [135, 44], but that is likely untrue generally [136, 132].

Pore-network modeling (see Sections 7.1, 7.2, and 7.3) is frequently used to numerically model mercury porosimetry [137, 138, 139, 140, 141, 142, 143, 144], as is classical percolation theory [145, 146, 147, 148, 45, 19]. For the latter, calculations based on the Bethe lattice may yield analytical formulae, such as by considering the concept of the accessibility function[5] in supercritical percolation [145][6]. However, in these models, separate PSDs are typically defined for the pore bodies and the pore throats, which, unlike the PSD determined from Eq. (4.1), may be more difficult to interpret without considering specific pore networks. Moreover, in supercritical percolation, infinite clusters only arise when the occupation probability exceeds the percolation threshold for the network considered; as a result, it may not be possible to obtain the complete PSD in some cases [45].

[5]defined as the map from a given occupation probability at a site to the fraction of sites belonging to an infinite cluster

[6]sites belonging to an infinite clusters are said to be percolating and are considered to be connected to the mercury reservoir via a continuous, mercury-filled path, allowing the accessibility to be interpreted as s_n

Another interesting approach in the literature, called the Random Corrugated Pore Structure Model, also produces analytical formulae for porosimetry curves [149, 150]. The authors consider a collection of "corrugated pores" of equal length, where each pore consists of a fixed number of equal-length cylindrical segments, whose radii are randomly assigned based on a prescribed PSD[7]. A pore is then exposed to mercury at both of its openings simultaneously, and the capillary pressure is varied to facilitate intrusion and extrusion. A critical pore constriction ratio is also specified as the criterion for **snap-off**[8], thereby causing some mercury to become **trapped** during extrusion [153]. The ratio of the volume of mercury withdrawn at the end of depressurization to the volume of mercury injected at the end of pressurization is referred to as the **withdrawal efficiency** [76]. It is equal to one minus the **residual saturation**[9], denoted by s_R, assuming that mercury fills the entire pore space of interest at the end of pressurization.

4.2 Theory and methods

We will apply our theory of capillary pressure hysteresis presented in Chapter 3, with some minor modifications for contact-angle hysteresis and mercury trapping, to **mercury cyclic porosimetry**, which includes not only the initial pressurization and depressurization steps, but also additional subsequent cycles. We define the saturation of mercury as:

$$s = \frac{V}{V_{\max}}, \tag{4.3}$$

[7]A corrugated pore qualitatively resembles a single pore branch, or a pore-space instance with no branching, in our probabilistic framework.

[8]Snap-off is a pore-scale mechanism that depends strongly on the local geometry of the pore space, and involves the formation of a saddle-shaped interface between the wetting and nonwetting fluids during imbibition, leading to the nonwetting phase splitting into discontinuous regions [65]. It is affected by the so-called pore body–to–pore throat size ratio, pore throat–to–pore body coordination number, the dynamical contact angles, and other factors [151, 152], and is thought to be responsible for the trapping of the nonwetting fluid during imbibition.

[9]The term residual saturation is reserved for the nonwetting phase to contrast with the irreducible saturation introduced in Section 3.1.3, which is reserved for the wetting phase.

where $V_{\max}$ is the maximum volume of mercury injected into the sample at any point in during the experiment. Here, and for the remainder of this chapter, we omit the subscript "n" and use s to refer to the saturation of the mercury phase.

We denote the PSD of the porous specimen by $F(r)$, as defined in Section 2.1.3 and to be determined from the mercury cyclic porosimetry data. Note that $r_{\min}$ may be limited by the maximum pressure reached during measurement, $p_{\max}$. We also assume that $V_{\max}$ reflects the true accessible volume of the pore space.

To model connectivity effects, we adapt the formulae derived in Chapter 3. For primary mercury intrusion, i.e., pressurization, we have:

$$s(F_c) = \frac{\alpha(1 - F_c)}{(1 - \alpha)F_c + \alpha}, \tag{4.4}$$

for primary mercury extrusion, i.e., depressurization, we have:

$$s(F_c) = 1 - \frac{\alpha F_c}{(1 - \alpha)(1 - F_c) + \alpha/(1 - s_R)}, \tag{4.5}$$

and for secondary mercury intrusion, i.e., repressurization, we have:

$$s(F_c) = s_0 + \frac{\alpha(F_0 - F_c)}{(1 - \alpha)(1 - (F_0 - F_c)) + \alpha/(1 - s_R)}, \tag{4.6}$$

where F_0 and s_0 represent the starting conditions for secondary intrusion. Here, Eq. (4.4) is identical to Eq. (3.40). Eq. (4.5) is derived from Eq. (3.41) by incorporating the residual saturation, s_R; when $s_R = 0$, Eq. (4.5) becomes the same as Eq. (3.41). Eq. (4.6) is derived from Eq. (3.40); given $(F_c, s) = (F_0, s_0)$ satisfies Eq. (4.5), in Eq. (4.6) we always have $s(0) = 1$ – that is, secondary intrusion following incomplete extrusion achieves the same maximum injection volume as primary intrusion; and for $s_0 = 0$, $F_0 = 1$, and $s_R = 0$, Eq. (4.6) simplifies to Eq. (4.4). Figure 4-1 contains examples of the $s(F)$ curves given by these equations. Note that for $\alpha \to 1$ and $s_R = 0$, all of Eqs. (4.4), (4.5), and (4.6) collapse onto the $s(F) = 1 - F$ line given by Eq. (3.42).

Finally, we account for contact-angle hysteresis by using different values for θ in

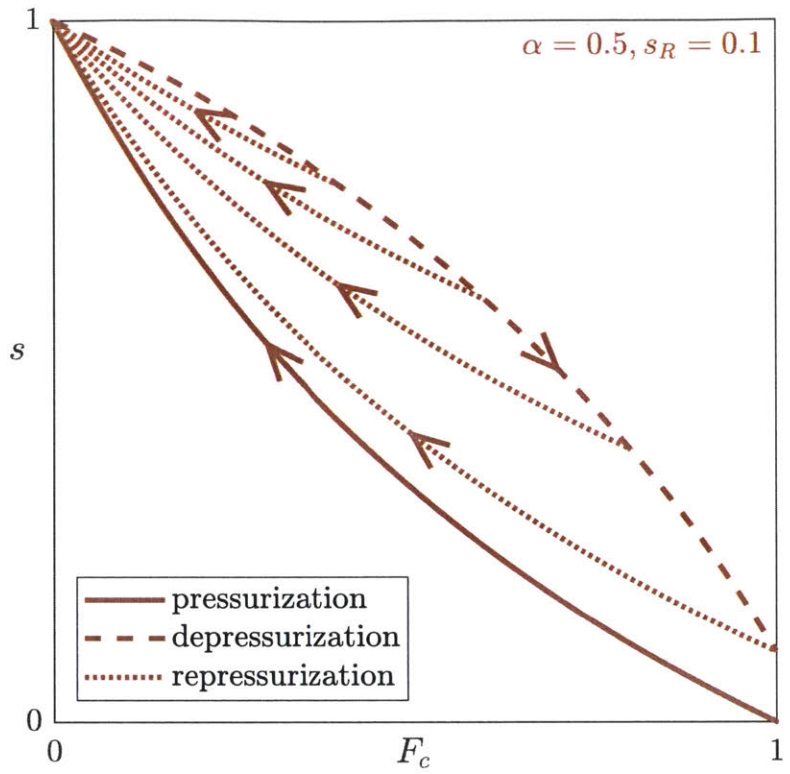

Figure 4-1: Plots of $s\,(F_c)$ for pressurization, depressurization, and repressurization from different starting values of F_c, given by Eqs. (4.4), (4.5), and (4.6), respectively, with $\alpha = 0.5$ and $s_R = 0.1$.

Eq. 4.1 for intrusion and extrusion. We define the parameter:

$$\kappa \equiv \frac{\cos\theta_{\text{extr}}}{\cos\theta_{\text{intr}}}, \tag{4.7}$$

which is less than unity. Figure 4-2 is a contour plot of κ for feasible values of θ_{intr} and θ_{extr}. Contact-angle hysteresis is absent when $\kappa = 1$.

Thus, in addition to the PSD, whose CDF we denote by $F(r)$, there are a total of four parameters in our model of mercury cyclic porosimetry: accessivity, $\alpha \in [0, 1]$; parameter for contact-angle hysteresis, $\kappa \in [0, 1]$; residual saturation, $s_R \in [0, 1]$; and the advancing contact angle, $\theta_{\text{intr}} \in [90°, 180°]$.

Given the primary intrusion curve, we require only α, κ, and s_R to predict the primary extrusion curve and all secondary intrusion curves (given the starting value of F_c for each). Therefore, we can determine a set of optimal values for α, κ, and s_R given

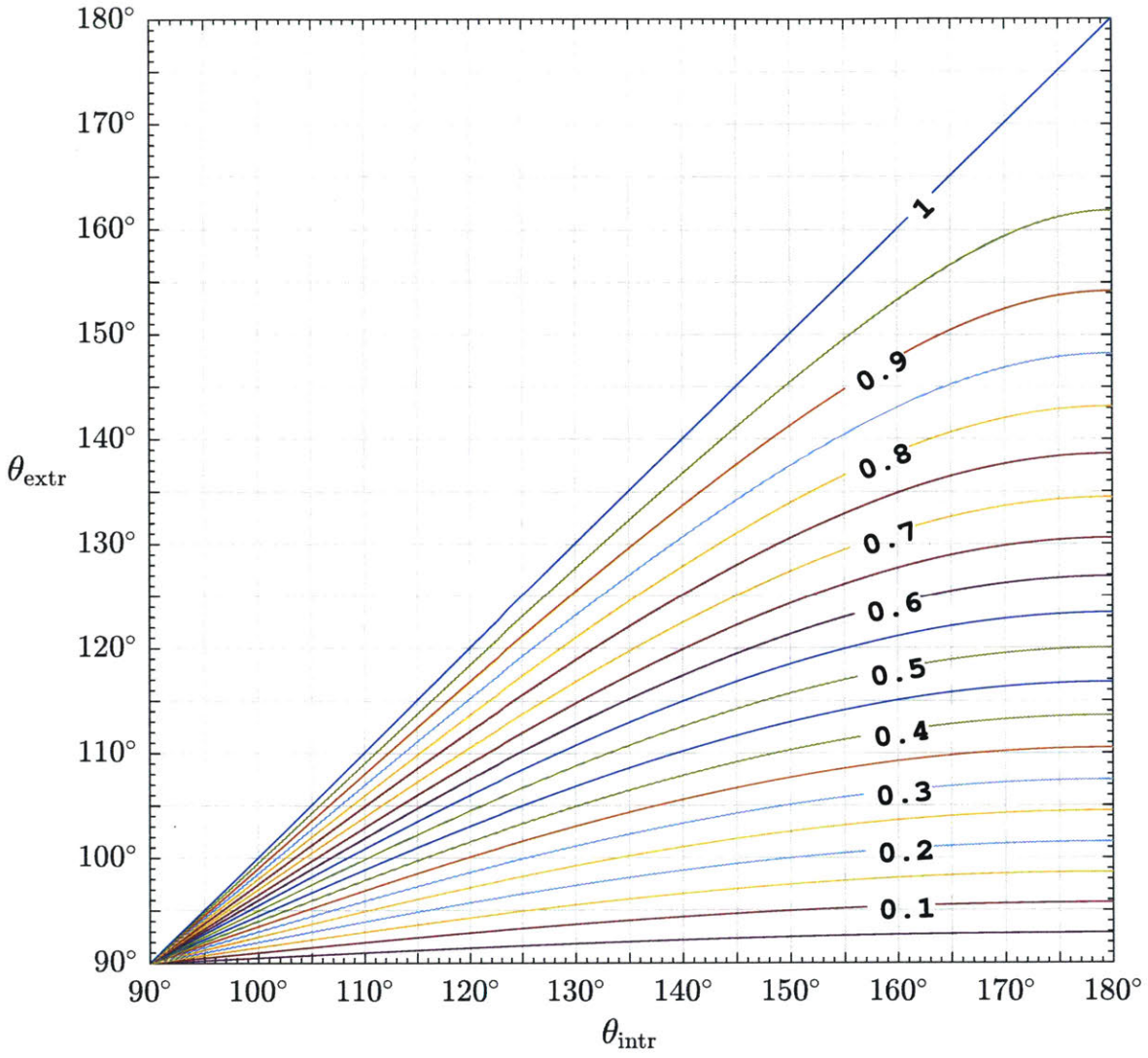

Figure 4-2: Contour plot of κ versus the advancing and receding contact angles, following Eq. (4.7). For a fixed θ_{intr}, the closer to θ_{intr} and the larger θ_{extr} is, the larger κ is.

the mercury cyclic porosimetry data for a porous material. Note that the end point of the pressurization curve and the starting point of the depressurization curve share the same s, but the p of the latter is lower at κ times that of the former. Analogously, the end point of the depressurization curve and the corresponding repressurization curve also share the same s, while p of the latter is higher at $1/\kappa$ times that of the former. These changes in p at constant s between curves are caused by the contact angle adapting to the reversal of the direction of change of p.

On the other hand, given the primary intrusion curve, we require only α and θ_{intr}

to compute the CDF of the PSD. Since α is determined based on fitting the mercury cyclic porosimetry data, we may vary θ_{intr} freely to shift the mean radius of the PSD[10]. To convert s to F, we solve for F_c in our formula for primary intrusion, Eq. (4.4), to obtain:

$$F_c = \frac{\alpha(1-s)}{(1-\alpha)s+\alpha}, \tag{4.8}$$

which, curiously, has the same form as Eq. (4.4), suggesting that the function $s(F_c)$ in Eq. (4.4) an involution [154]. The variable p is converted to r using Eq. (4.1).

Mercury porosimetry measurements were taken for numerous samples of a total of four different commercially available porous materials[11], which we shall refer to as:

- "CPG": SCHOTT CoralPor® porous glass 1000, produced from a borosilicate mother glass that is subjected to thermal and chemical treatments, with the typical average pore diameter ranging from 4 to 10 nm, according to the manufacturer [155];
- "Boehmite": SASOL Pural® 200, a high purity boehmite alumina (80% Al_2O_3) synthesized from aluminum metal, with a typical particle size (d_{50}) of 40 nm, according to the manufacturer [156];
- "Darco": an activated carbon;
- "GBac": an activated carbon.

Only a cursory examination of Darco and GBac were carried out, resulting in a single mercury intrusion–extrusion porosimetry experiment for each material. Thus, for the purpose of this thesis, we shall disregard those two materials and instead focus on CPG and boehmite.

Mercury porosimetry measurements were taken in a commercial penotrometer using mercury at a temperature of about 19 degrees Celsius. Each sample was initially subjected to an evacuation pressure of 7 Pa for 5 min, before submerged in mercury

[10]Varying γ in Eq. (4.1) has the same effect.
[11]supplied by coauthor Remi Goulet

Table 4.1: Summary of the mercury porosimetry data sets for CPG and boehmite.

#	Material	Sample mass (g)	Pressurization	Depressurization	Repressurization	Plot
1	CPG	0.4960	once	once	–	Figure 4-3, red curves
2	boehmite	0.2611	once	once	–	Figure 4-4, red curves
3	CPG	0.2728	once	twice	once	Figure 4-3, blue curves
4	boehmite	0.3131	once	twice	once	Figure 4-4, blue curves
5	CPG	0.4789	once	four times	three times	Figure 4-3, green curves
6	boehmite	0.5100	once	four times	three times	Figure 4-4, green curves

at a pressure of anywhere from 3.5×10^3 to 4.0×10^3 Pa. Primary intrusion was then carried out, where the pressure of mercury was raised in hundreds of small increments before reaching the maximum value, $p_{\max}$, which was different for each experiment but never exceeded 4.1×10^8 Pa. On a logarithmic scale, the magnitudes of the majority of the pressure increments and decrements were comparable[12]. An equilibration time of 30 s was allowed after each pressure step change was effected. The mass of each specimen ranged from 0.2611 to 0.5100 g.

4.3 Results and discussions

Mercury porosimetry measurements were conducted on a total of six specimens of CPG and boehmite – three for either material. We summarize these experiments in Table 4.1. The normalized porosimetry curves[13] for specimens of either material are plotted on the same set of axes, resulting in Figures 4-3 and 4-4. The normalized data

[12]meaning that monotonic portions of the sequences of pressure readings may resemble a geometric sequence

[13]Low pressure data were discarded for both materials where V rises steeply at the beginning of primary intrusion, which can be believably attributed to the spacing between grains that make up the solid matrix, or the so-called macropores [157]. High pressure data for boehmite were also discarded due to the lack of change in the intrusion volume in that regime.

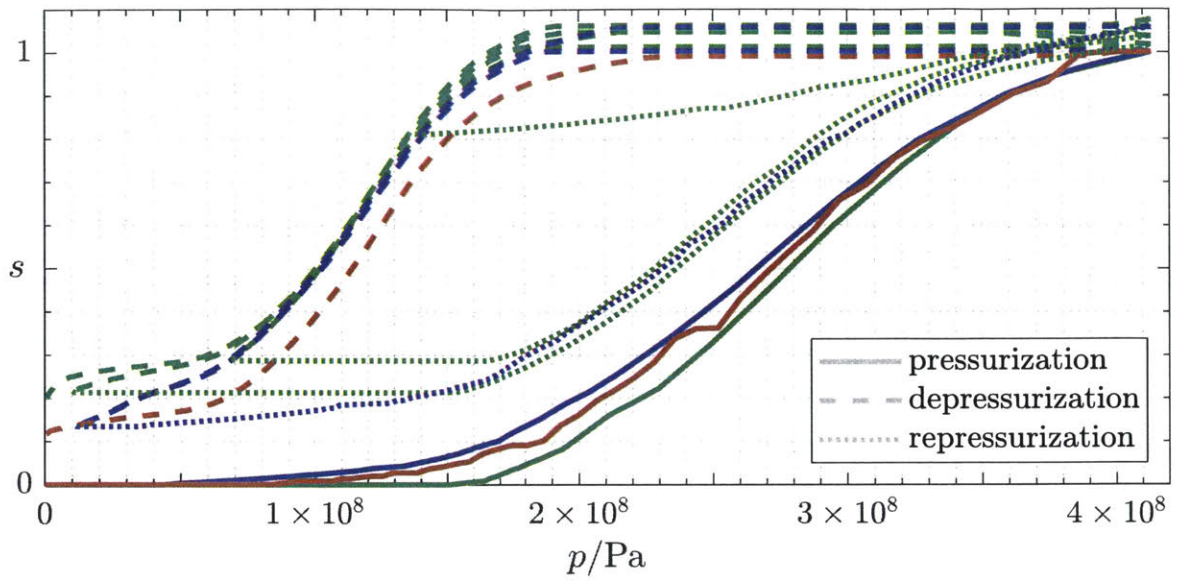

Figure 4-3: Normalized mercury cyclic porosimetry data for CPG. The red, blue, and green curves correspond to independent measurements on three different specimens of CPG, and the solid, dashed, while dotted curves represent pressurization, depressurization, and repressurization steps. Data points with pressures below 8.2×10^5 Pa are not shown.

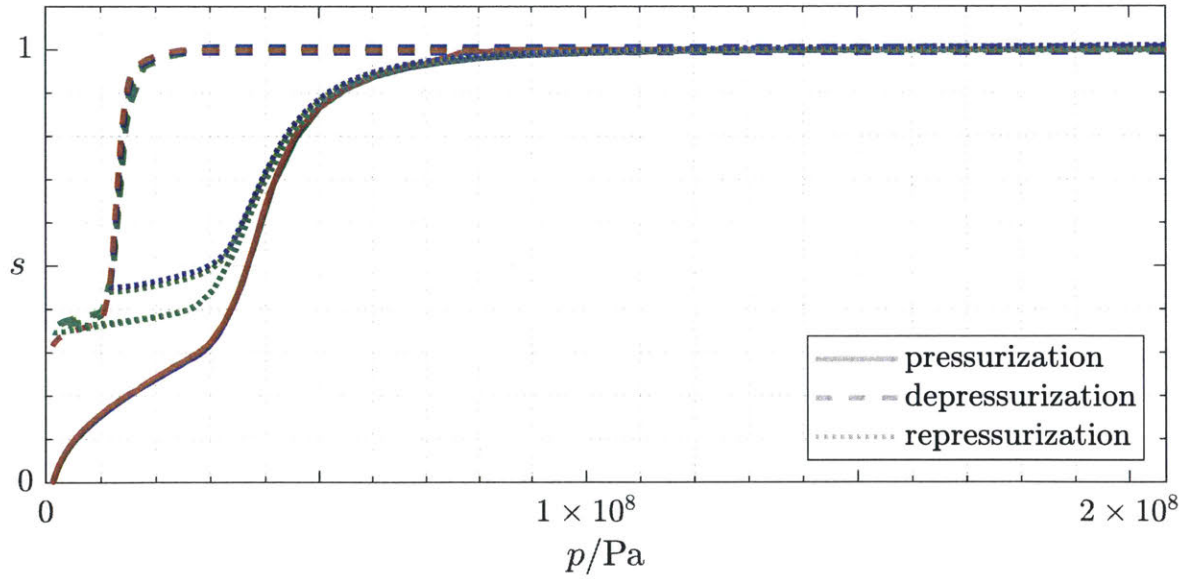

Figure 4-4: Normalized mercury cyclic porosimetry data for boehmite. The red, blue, and green curves correspond to independent measurements on three different specimens of boehmite, while the solid, dashed, and dotted curves represent pressurization, depressurization, and repressurization steps. Data points with pressures below 1.3×10^6 Pa or above 2.1×10^8 Pa are not shown.

agree well between specimens of the same material, and especially so for boehmite.

4.3.1 Determination of model parameters

For each material, we take the average of curves for different specimen that share the same pressure end points, and use them to determine the best-fit model parameters by minimizing the sum of squared errors of prediction. The best-fit predictions for CPG and boehmite are plotted over the experimental measurements in Figures 4-5 and 4-4, respectively. For CPG, the best-fit parameters are $\alpha = 0.2626$, $\kappa = 0.6511$, and $s_R = 0.1944$; for boehmite, we have $\alpha \to 1.0000$, $\kappa = 0.3601$, and $s_R = 0.2011$.

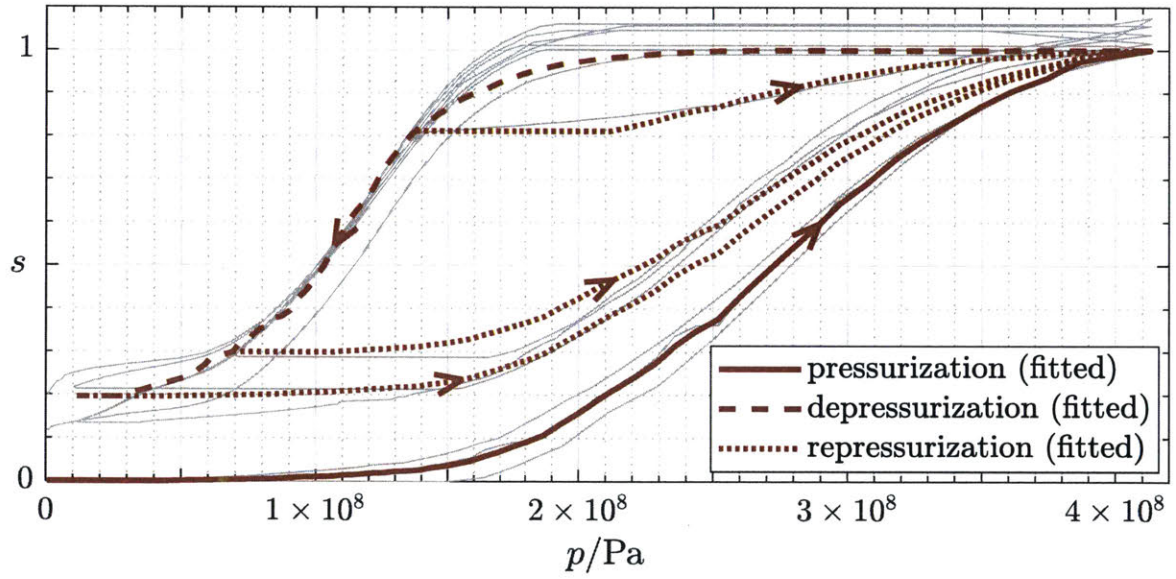

Figure 4-5: Plot of the best-fit model ($\alpha = 0.2626$, $\kappa = 0.6511$, and $s_R = 0.1944$) compared against all experimental data for CPG.

We explore the sensitivity of the goodness of fit with respect to model parameters in Figure 4-7. For each material, we fix α and κ, and minimize the sum of squared errors with respect to s_R; we then produce a contour plot of the exponential of minus the optimal solution value in the α–κ plane near the point that represents the best-fit solution.

We see that there is relatively little uncertainty in the numerical values of the best-fit parameters. For CPG, the shapes of the contours imply that the goodness of fit is not significantly worsened by simultaneously increasing α and decreasing κ;

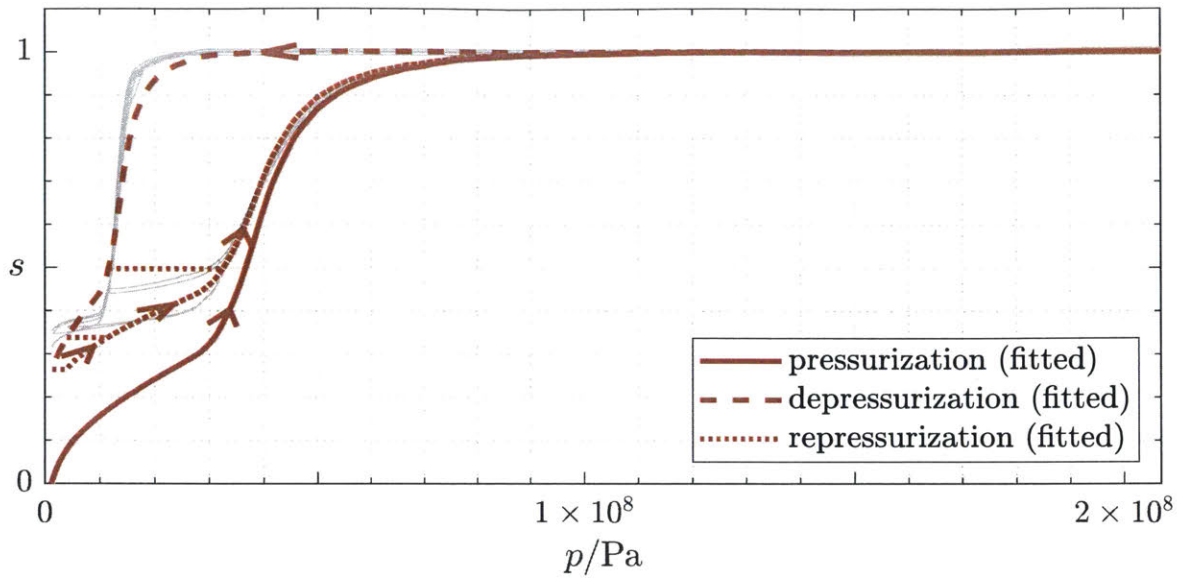

Figure 4-6: Plot of the best-fit model ($\alpha \to 1.0000$, $\kappa = 0.3601$, and $s_R = 0.2011$) compared against all experimental data for boehmite.

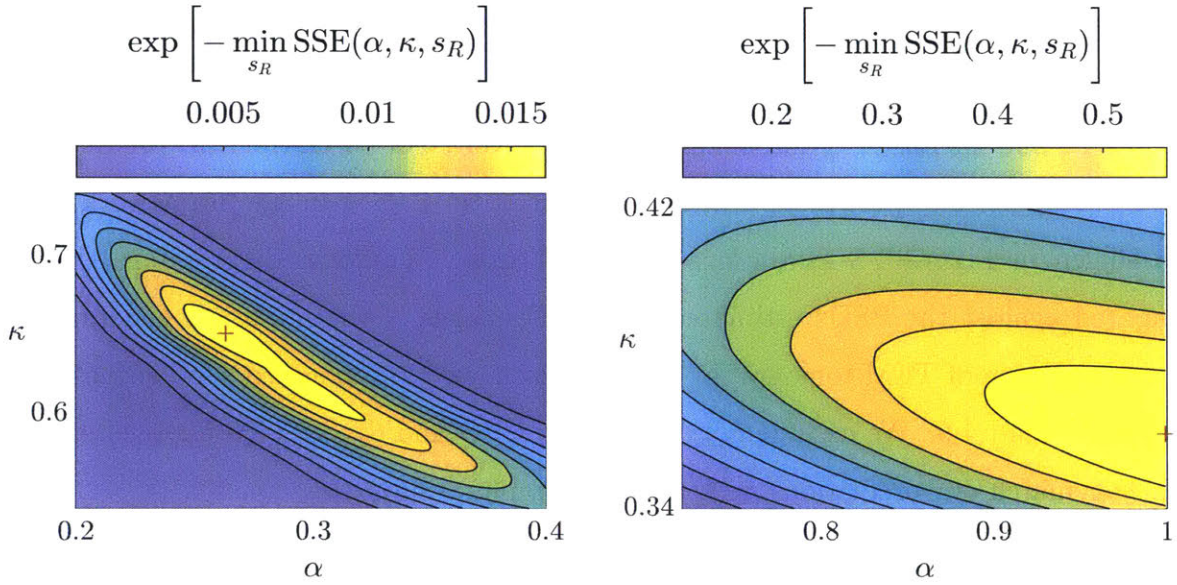

Figure 4-7: Sensitivity of the goodness of fit to model parameters. The left and right panels correspond to CPG and boehmite, respectively. The maximum in the α–κ plane (corresponding to the best-fit solution) is marked with a red plus sign. The fit is worse outside of the shown α–κ domain.

nevertheless, α is expected to remain far below 0.5, indicating significant connectivity effects or serial connectivity between different-size pore slices. For boehmite, the best-fit α is approximately unity, indicating the complete absence of connectivity effects;

however, our model does not perfectly fit the experimental data at lower pressures[14], as seen in Figure 4-6.

We note that the effects of varying α and κ are "orthogonal" to each other: changing α affects the relationship between s and F_c (via Eqs. (4.4), (4.5), and (4.6)) and hence shifts the predicted points on the depressurization and repressurization curves vertically, changing κ affects the relationship between p and r (via Eqs. (4.1) and (4.7)) and hence shifts those points horizontally. Consequently, we are able to distinguish between the contributions of the ink-bottle effect and contact-angle hysteresis to the overall hysteresis observed in the cyclic porosimetry measurements by fitting our model.

4.3.2 Determination of the pore-size distribution

We compute the PSDs of the two materials using estimates of accessivities obtained from mercury cyclic porosimetry. The results are plotted as solid blue curves in Figures 4-8 and 4-9 for CPG and boehmite, respectively. For CPG, the PSD predicted by the standard interpretation, which corresponds to $\alpha \to 1$ in our framework, is also shown in Figure 4-8 as the green dashed curve. These predictions are then compared against the PSDs estimated from 3-D images of the materials generated by segmentation of TEM tomography data[15], which are plotted as red solid curves in Figures 4-8 and 4-9. We assume $\theta_{\text{intr}} = 115°$ for CPG and $\theta_{\text{intr}} = 140°$ for boehmite to better match our predictions with the tomography results.

For CPG, the low accessivity estimated from mercury porosimetry accentuates the contrast between the PSDs predicted by our approach and by the standard interpretation. The PSD predicted with $\alpha \to 1$ is narrower and is biased toward smaller pore radii compared to that predicted with the best-fit value of $\alpha = 0.2626$, which matches the estimate obtained from TEM tomography more closely. This is consistent with

[14]Note that the shapes of the depressurization and repressurization curves at lower pressures are notably different from that of the pressurization curve. A better fit may be obtained by discarding the pressurization curve and considering the depressurization and repressurization curves only (after renormailization), but that does not significantly affect our key findings for boehmite.

[15]supplied by coauthor Pierre Levitz

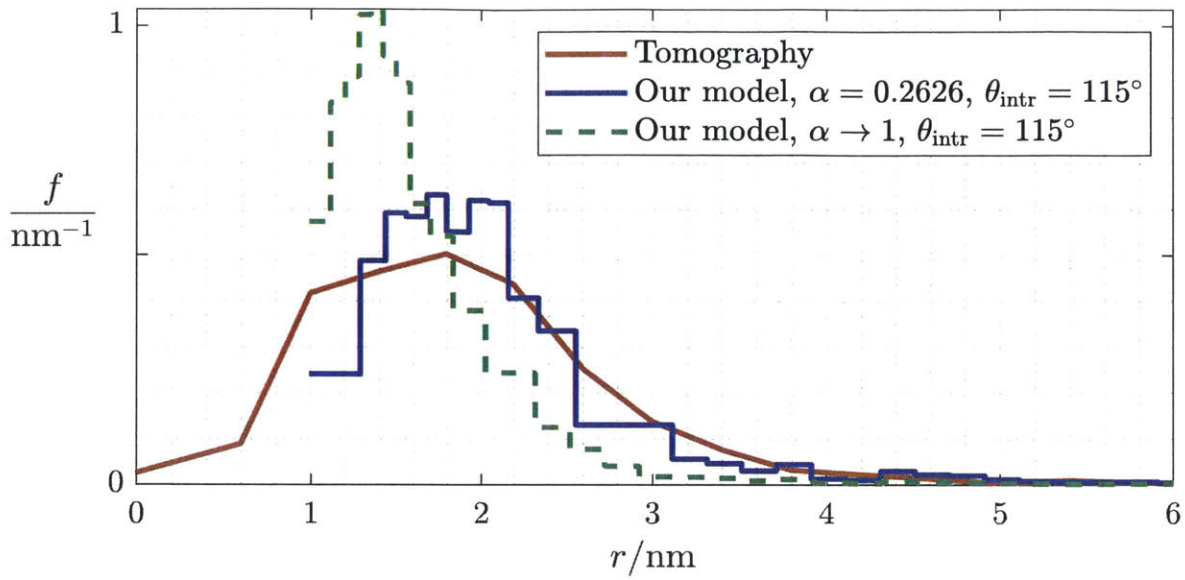

Figure 4-8: Comparison of PDFs of PSDs of CPG extracted from TEM tomography data (solid red curve), predicted by our approach with $\alpha = 0.2626$ (solid blue curve), and predicted by the standard interpretation, i.e., $\alpha \to 1$ in our approach (dashed green curve). The PSD predicted using the best-fit value of accessivity obtained by fitting mercury porosimetry data matches the TEM tomography results more closely than that obtained from the standard interpretation, which overestimates the volume fraction of smaller pores.

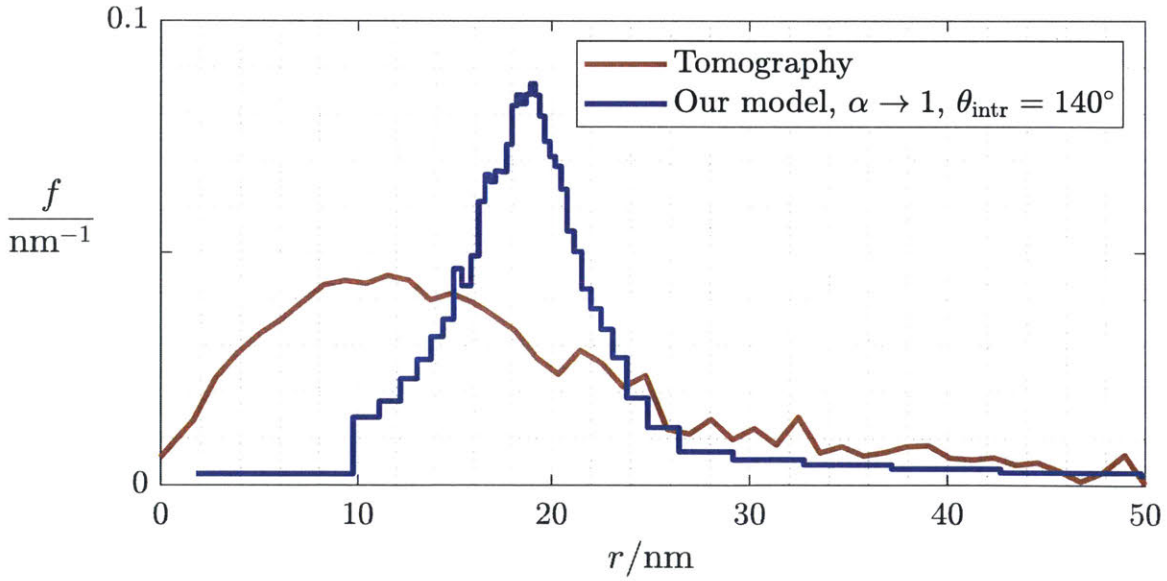

Figure 4-9: Comparison of PDFs of PSDs of boehmite extracted from TEM tomography data (solid red curve) and predicted by our approach with $\alpha \to 1$ (solid blue curve), which coincides with that predicted by the standard interpretation. The mismatch of these PSD predictions is not explained by our model.

the consensus in the literature that the standard interpretation of mercury intrusion porosimetry tends to overestimates the volume fraction of smaller pores [131, 79].

For boehmite, the PSD predicted from mercury porosimetry is notably different from that estimated from the tomography data. While the tomography analysis suggests that pore slices with radii smaller than 10 nm make up about 27% of the pore volume, the mercury porosimetry measurements imply the near-complete absent of such small pores, which is evinced by the plateauing of the intrusion curve past a mercury pressure of approximately 1×10^8 Pa. It would appear that this discrepancy cannot be explained by our theory: the advancing contact angle would have to be usually low[16] for mercury porosimetry to predict a significant volume fraction of pores with radii in the 1–10 nm range, even with $\alpha = 1$. Therefore, we suspect that the mismatch of the PSDs obtained from the two approaches may be due to different definitions of pore radius, or isolated pores which are delectable in a 3-D image of the material but inaccessible by mercury even at pressures as high as 4.1×10^8 Pa. As we will see later in Figure 7-14, the water sorption isotherms for boehmite appear nonhysteretic, which may corroborate our claim that connectivity effects are negligible for this material.

Recall that only α and θ_{intr} are required to transform the mercury intrusion data into the PSD, using only two simple algebraic formulae, i.e., Eqs. (4.1) and (4.8). Therefore, we can be assured that the PSDs obtained by our approach is no worse than that obtained by the standard interpretation using Eq. (4.1) alone, as long as we have a reasonable estimate for the pore-space accessivity, which can be obtained by fitting mercury cyclic porosimetry measurements or, potentially, from other characterization techniques for porous materials, e.g., vapor soprtion–desorption [158, 159, 160, 161, 105, 162, 163], water intrusion–withdrawal in gas diffusion layers [164, 165, 166, 167, 168], Wood's metal porosimetry [169, 170, 171], etc..

[16]The value of θ_{intr} required for a pressure of 1×10^8 Pa to correspond to an equilibrium capillary pore radius of 1×10^{-9} m is, according to Eq. (4.1), as low as 96°.

Chapter 5

Microscopic theory of relative permeability hysteresis

In this chapter, we will begin our examination of relative permeability hysteresis in multiphase flow in porous media. Like capillary pressure hysteresis, for which we have presented a microscopic theory in Chapter 3, hysteresis in relative permeabilities also depends strongly on pore-space morphology and pore-scale fluid distribution; modeling them from first principles, however, turns out to be much more challenging. There are several reasons for this. Firstly, the relationship between pore-space morphology and permeabilities is highly nonlinear even for the idealized pore-space instances considered in our probabilistic framework because the hydraulic resistances of pore slices are summed both in series and in parallel. Secondly, relative permeabilities pertain to the dynamics of fluid flow, which is inherently a nonequilibrium process and may be less amenable to a simpler quasistatic analysis. Thirdly, the pore-scale mechanics of fluid flow are not yet fully understood, and may vary dramatically depending on the local geometries of the pore space and the properties of the solid matrix and the fluid phases.

Despite these challenges, we would like to apply our probabilistic framework to relative permeabilities to arrive at simple continuum models of hysteresis with some connection to microscopic physics. We will then propose models of varying degrees of complexity and discuss their strengths as well inadequacies.

5.1 Introduction

Recall from Chapter 1 that relative permeabilities are responsible for describing the deviations of Darcy velocities in two-phase flow relative to single-phase flow. In fact, we can already deduce several salient attributes in the relationships between relative permeabilities and saturation based on the form of Eq. (1.3).

Firstly, when $s_w = 0$, we must have $k_{rw} = 0$ because the Darcy velocity of the wetting phase must be zero when the phase is absent from the pore space, while it is also the case that $k_{rn} = 1$ so we recover the single-phase Darcy law, i.e., Eq. (1.1), for the nonwetting phase. Conversely, when $s_w = 1$, we must have $k_{rw} = 1$ and $k_{rn} = 0$.

Secondly, for intermediate values of s_w, we generally expect $k_{rw}, k_{rn} \in [0, 1]$ as well as $k_{rw} + k_{rn} \in [0, 1]$ – intuitively speaking, the pore space should not become more permeable overall by hosting multiple immiscible fluid phases, not to mention that pinned interfaces and trapped fluids may further reduce relative permeabilities by blocking off flow channels that would contribute to k_s in single-phase flow [15].

Thirdly, the relative permeabilities of the wetting and nonwetting phases are generally not symmetric with respect to saturation – that is, it is typically the case that $k_{rw}(s_w) < k_{rn}(1 - s_w)$. This is because the wetting phase tends to occupy pore slices with smaller radii [15], which have lower hydraulic conductances, as we have pointed out in Section 2.1.3.

Lastly, the relative permeability of the nonwetting phase usually exhibits more hysteresis than that of the wetting phase. Additionally, at the same saturation, k_{rn} is usually higher during drainage than during imbibition [15]. We note that all of the above features can be observed in the illustration in the right panel of Figure 1-1.

In practice, simple power laws are commonly used to produce relative permeability curves with the desired characteristics. An example is given by Corey [172]:

$$k_{rw} = {s_w}^4, \quad k_{rn} = (1 - s_w)^2(1 - {s_w}^2), \tag{5.1}$$

where, as detailed in Section 3.1.3, the effective saturation is often used in place of saturation, as is the case in most other models in the literature to be discussed below.

It is possible to adjust these empirical laws, e.g., by altering the scaling exponents [173, 174, 84, 175, 176], to fit experimentally measured relative permeability data, including those that involve hysteresis [177, 15].

Some authors have developed a set of methods that seek to predict relative permeability curves from capillary pressure curves. These methods are essentially based on the capillary bundle model or its basic variants, and are widely celebrated in practice[1] [34, 54, 179, 180, 172, 181, 178]. For example, the Burdine equations [180], as presented in [84], write:

$$k_{rw} = {s_w}^2 \frac{\displaystyle\int_0^{s_w} \frac{\mathrm{d}\hat{s}_w}{\left[p_c(\hat{s}_w)\right]^2}}{\displaystyle\int_0^1 \frac{\mathrm{d}\hat{s}_w}{\left[p_c(\hat{s}_w)\right]^2}}, \quad k_{rn} = (1-s_w)^2 \frac{\displaystyle\int_{s_w}^1 \frac{\mathrm{d}\hat{s}_w}{\left[p_c(\hat{s}_w)\right]^2}}{\displaystyle\int_0^1 \frac{\mathrm{d}\hat{s}_w}{\left[p_c(\hat{s}_w)\right]^2}}, \tag{5.2}$$

where $p_c(s_w)$ represents the capillary pressure data for the porous medium, and $\hat{s}_w$ denotes the dummy variable of integration. By considering two random cylindrical capillary elements connected in series, Mualem proposed the following modified formula for the wetting phase:

$$k_{rw} = {s_w}^n \left[\frac{\displaystyle\int_0^{s_w} \frac{\mathrm{d}\hat{s}_w}{p_c(\hat{s}_w)}}{\displaystyle\int_0^1 \frac{\mathrm{d}\hat{s}_w}{p_c(\hat{s}_w)}} \right]^2, \tag{5.3}$$

where the exponent n is allowed to vary as a model parameter, and may be either positive or negative [178].

The pore-space morphology in real porous media are, of course, much more complex, with different-size pore slices arranged both in parallel and in series. Even in single-phase flow, establishing a simple theory that relates pore-space morphology to the intrinsic permeability, k_s, is already challenging, although certain limiting cases may be more amenable to analysis [30]. Recalling from our general discussion in Section 2.2, coefficients of transport in composite materials cannot be determined

[1]The paper of Mualem [178], for example, has received an impressive total of 6922 citations on Google Scholar as of the submission of this thesis.

uniquely based on its makeup, but only up to certain theoretical bounds. Similarly, for resistors connected in an electrical network (i.e., both in series and in parallel), which may represent the electrical analogy of the problem of intrinsic permeability in porous media [182], it is also challenging to arrive at theoretical statements regarding the total conductance of the network, e.g., [183], not to mention the complications that arise when multiple immiscible phases are present [184].

Nevertheless, we would like to study the implication of our probabilistic framework on relative permeabilities in multiphase flow in porous media. Our goal is to create simple continuum models for relative permeabilities that not only bear some connection to pore-scale morphology via concepts in our probabilistic framework, but also allow for the natural inclusion of hysteresis in conventional continuum simulations of multiphase flow.

5.2 Our theory

Suppose we have a total of N resistors of resistances $\Phi_1, \ldots, \Phi_N$. The total resistance of all resistors connected in series is given by:

$$\Phi_{\text{series}} = \sum_{i=1}^{N} \Phi_i, \tag{5.4}$$

while that of the resistors arranged in parallel is:

$$\Phi_{\text{parallel}} = \left(\sum_{i=1}^{N} {\Phi_i}^{-1} \right)^{-1}. \tag{5.5}$$

Recall from Sections 2.2 and 3.2 that the pore-space instances in our probabilistic framework are arranged in parallel and accessed by fluid phases independently. Thus, conceptually speaking, the mean relative permeabilities of both fluid phases in the ensemble of instances must take the form:

$$k_{rw} = \frac{T_w \langle 1/\varphi_{I,w} \rangle}{\langle 1/\varphi_{I,\text{sat}} \rangle}, \quad k_{rn} = \frac{T_n \langle 1/\varphi_{I,n} \rangle}{\langle 1/\varphi_{I,\text{sat}} \rangle}. \tag{5.6}$$

Here, $\varphi_{I,\text{sat}}$ denotes the hydraulic resistance of an instance if it were saturated by a single fluid, while $\varphi_{I,w}$ (or $\varphi_{I,n}$) denotes the hydraulic resistance of an instance that allows the wetting (or nonwetting) phase to flow through given the current pore-scale distribution of fluid phases[2]. The reciprocals of these hydraulic resistances are then averaged to give the mean hydraulic conductances of instances of each type. Note that $\langle 1/\varphi_{I,\text{sat}} \rangle$ can be thought of as a measure of the intrinsic permeability of the porous medium that the ensemble represents. Finally, T_w (or T_n) is the expected fraction of instances that are "w-conducting" (or "n-conducting"), i.e., instances that allow the wetting (or nonwetting) phase to flow through[3].

Let us contrast the hydraulic resistance of any instance against that of an instance that is conducting to a particular fluid phase. Take $\Phi_{I,\text{sat}}$ and $\Phi_{I,w}$ for example – the two random variables follow different probability distributions for two separate reasons: firstly, w-conducting instances may contain pore branches that are blocked and thus not w-conducting, i.e., only a fraction t_w of branches in a w-conducting instance may allow the wetting fluid to flow through; secondly, pore slices found in w-conducting branches may have a different radius distribution than in the entire ensemble of instances since the wetting fluids tend to preferentially occupy smaller pores. To facilitate our subsequent discussions, we will call these two effects **branch blocking** and **pore-radius bias**, respectively. Because branch blocking is the root cause for entire instances to be blocked, i.e., t_w and T_w are related, we refer to them collectively as **percolation effects**.

Now, we will use these ideas to rationalize the aforementioned formulae of Burdine (Eq. (5.2)), Mualem (Eq. (5.3)), and others. We will then propose a straightforward modification to their formulae using the concept of radius-resolved saturation in our framework to enable the prediction of hysteresis. After that, we will reexamine Eq. (5.6) and link it to our probabilistic framework more concretely and quantita-

[2]Note that the hydraulic resistances of such instances are described by random variables designated by $\Phi_{I,\text{sat}}$, $\Phi_{I,w}$, and $\Phi_{I,n}$, while their lower-case counterparts refer to specific values assumed by the respective random variables.

[3]In words, Eq. (5.6) asserts that0 the relative permeability of phase w, say, is equal to the ratio of the mean hydraulic conductance of an w-conducting instance to that of any instance, multiplied by the fraction of instances in the ensemble that are w-conducting.

tively.

5.2.1 Semi-empirical modification of the formulae of Burdine and Mualem

We may rewrite Eqs. (5.2) and (5.3) in terms of the PSD by applying a theory of capillary pressure, the simplest of which is the capillary bundle model, which corresponds to the $\alpha \to 1$ limit in our theory detailed in Chapter 3. In this limit, it follows from Eqs. (3.4) that:

$$\mathrm{d}s_w = \mathrm{d}F_c. \tag{5.7}$$

Also, we know from Eq. (2.10) that:

$$p_c \propto \frac{1}{r_c}. \tag{5.8}$$

Thus, we may rewrite Eq. (5.2) as:

$$k_{rw}(s_w) = {s_w}^2 \frac{\int_0^{F_c} r^2 \,\mathrm{d}F}{\int_0^1 r^2 \,\mathrm{d}F}, \quad k_{rn}(s_w) = (1 - s_w)^2 \frac{\int_{F_c}^1 r^2 \,\mathrm{d}F}{\int_0^1 r^2 \,\mathrm{d}F}, \tag{5.9}$$

where r is evaluated from F via the effective inverse of the CDF of the PSD defined in Section 2.1.3.

The definite integrals that appear in Eq. (5.9) represent PSD-weighted averages of r^2 over different ranges of pore radii[4], while the physical significance of the quantity r^2 is revealed through the definition of the PSD and Eq. (2.9). Consider a capillary bundle consisting of straight cylindrical capillaries with the same length and subject to the same pressure drop. Given the CDF of the volume-based PSD, F, the number fraction of capillaries whose radii are near r is given by $r^{-2}\,\mathrm{d}F$, while the volumetric

[4]This may seem more obvious if we change the variable of integration to r, e.g., $\int_0^{F_c} r^2 \,\mathrm{d}F = \int_0^{r_c} r^2 f(r) \,\mathrm{d}r$, where f denotes the PDF of the PSD.

flow rate through such a capillary is proportional to r^4. Thus, the volumetric flow rate through all capillaries whose radii are near r is proportional to the product of the two, namely, $r^2\,\mathrm{d}F$. Integrating this quantity over a particular range of pore radius gives the partial permeability associated with the corresponding subset of the capillary bundle.

Instead, if we assume that the capillary bundle consists of capillaries that are of the same volume, then there would be an equal number of capillaries of each radius in the ensemble, but the length of each capillary becomes proportional to r^{-2}. Then, according to Eq. (2.9), the volumetric flow rate through capillaries with radii near r becomes proportional to $r^6\,\mathrm{d}F$. Hence, depending on the assumptions associated with variations in the pore radius, which has to do with the pore axial coordinate chosen to measure ℓ in our probabilistic framework, the scaling exponent in the integrand in Eq. (5.9) could conceivably vary, and thus be treated as a free parameter.

In any case, we see that the ratio of the definite integrals for the relative permeability of either phase in Eq. (5.9) accounts for the combined effects of pore-radius bias and T_w: in the $\alpha \to 1$ limit, all capillaries smaller than F_c are filled with the wetting fluid and hence w-conducting, while all remaining capillaries are n-conducting. In fact, we note that:

$$\frac{\displaystyle\int_0^{F_c} r^2\,\mathrm{d}F}{\displaystyle\int_0^1 r^2\,\mathrm{d}F} + \frac{\displaystyle\int_{F_c}^1 r^2\,\mathrm{d}F}{\displaystyle\int_0^1 r^2\,\mathrm{d}F} = 1, \tag{5.10}$$

meaning that all pore slices in the pore space are contributing to the flow of either one of the two phases. Given that, the factors ${s_w}^2$ and $(1-s_w)^2$ in Eq. (5.9) can be taken as empirical descriptions of percolation effects. Without them, the relative permeabilities of the two phases would always sum to unity, which is not typical for real porous media, as explained in Section 5.1.

Now, we propose a modified form of these semi-empirical formulae for relative

permeabilities:

$$k_{rw}[\psi_w(F)] = \left(\frac{\alpha F_c}{(1-\alpha)\int_{F_c}^{1}(1-\psi_w(F))\,\mathrm{d}F + \alpha} \right)^2 \frac{\int_0^1 r^2 \psi_w(F)\,\mathrm{d}F}{\int_0^1 r^2\,\mathrm{d}F}, \tag{5.11}$$

$$k_{rn}[\psi_w(F)] = \left(\frac{\alpha(1-F_c)}{(1-\alpha)\int_0^{F_c}\psi_w(F)\,\mathrm{d}F + \alpha} \right)^2 \frac{\int_0^1 r^2 (1-\psi_w(F))\,\mathrm{d}F}{\int_0^1 r^2\,\mathrm{d}F}, \tag{5.12}$$

where the relative permeabilities are now written as functionals of the radius-resolved saturations[5], which contains information about precisely which pore slices contain the wetting phase. We replace the power-law factors for percolation effects with $\psi_{\mathrm{im},w}F_c$ and $\psi_{\mathrm{dr},n}(1-F_c)$ from Eqs. (3.38) and (3.39) for k_{rw} and k_{rn}, respectively, and account for pore-size radius based on $\psi_w(F)$. Because the evolution of $\psi_w(F)$ inherently captures any capillary pressure hysteresis according to our microscopic theory, the trajectories of k_{rw} and k_{rn} also become naturally hysteretic for $\alpha < 1$. In the limit of $\alpha \to 1$, we recover Eq. (5.9) and thereby Eq. (5.2).

Note that:

$$\frac{\int_0^1 r^2 \psi_w(F)\,\mathrm{d}F}{\int_0^1 r^2\,\mathrm{d}F} + \frac{\int_0^1 r^2 (1-\psi_w(F))\,\mathrm{d}F}{\int_0^1 r^2\,\mathrm{d}F} = 1, \tag{5.13}$$

so as before, if it were not for the semi-empirical factors for percolation effects, all pore slices would be contributing to the flow of at least one fluid phase, even for $\alpha < 1$, which contradicts with the pore-scale picture entailed by our probabilistic framework. This observation highlights the semi-empirical nature of Eqs. (5.11) and (5.12). Nevertheless, we maintain that our formulae represent an incremental improvement over the formulae of Burdine, Mualem, and others: by setting $\alpha < 1$, the model naturally predict hysteresis in relative permeability hysteresis thanks to the information contained in $\psi_w(F)$ about the pore-scale distribution of fluids.

[5]which, as we recall, are related to the conventional saturations, s_w and s_n, via Eq. (3.11)

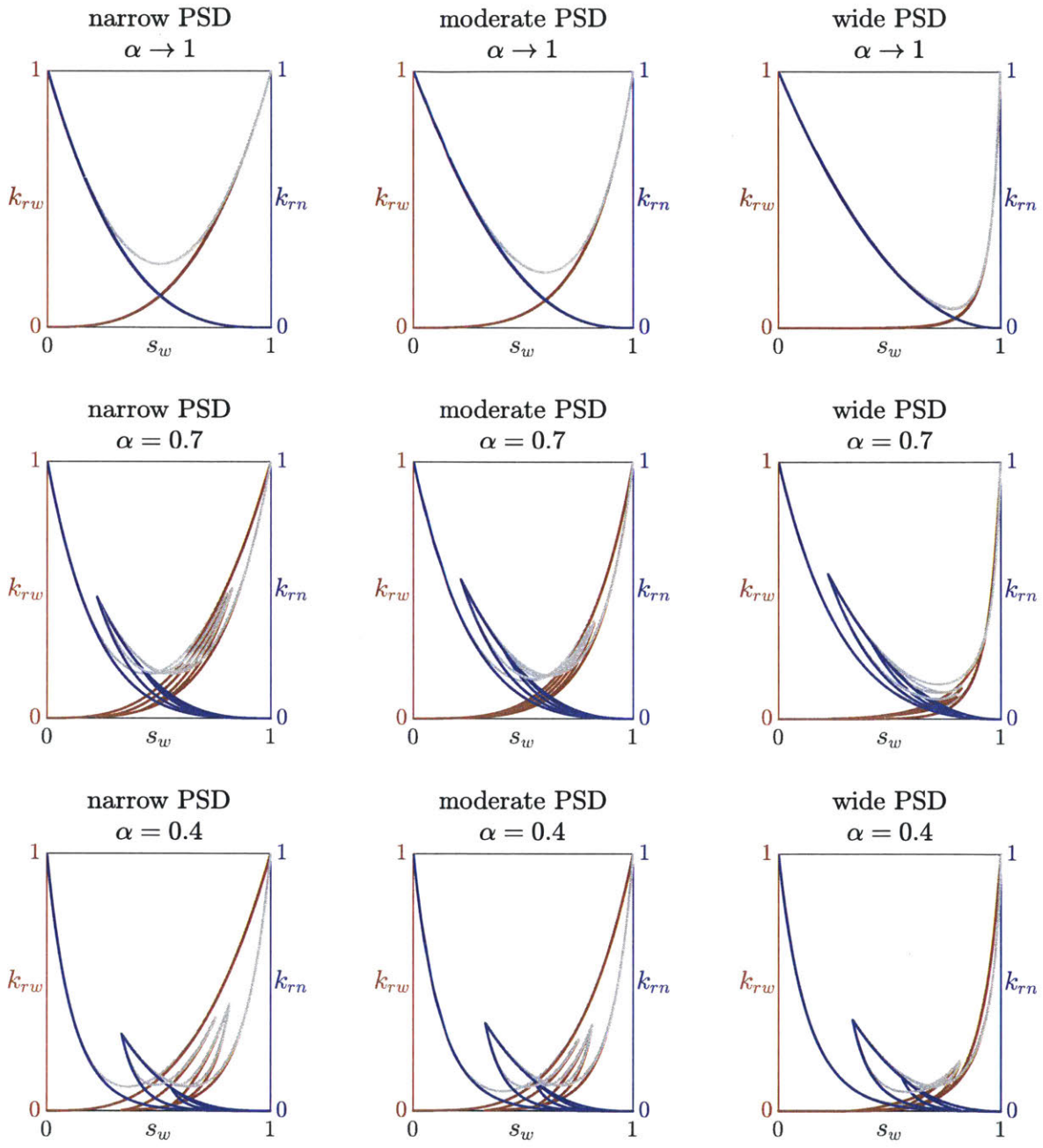

Figure 5-1: Scanning curves of k_{rw} (red curves), k_{rn} (blue curves), as well as $k_{rw} + k_{rn}$ (gray curves) versus s_w predicted by Eqs. (5.11) and (5.12) for three different accessivities ($\alpha \to 1$, $\alpha = 0.7$, and $\alpha = 0.4$) and three different PSDs (log-normal distribution with $\mu = 0$ and $\sigma = 0.01$, $\sigma = 0.5$, and $\sigma = 2$, where μ and σ are the mean and standard deviation of the associated normal distribution).

Figure 5-1 contains predictions of our semi-empirical formulae for relative permeability hysteresis. The scanning curves are generated by varying F_c between the following end points in the order they are listed: 0, 1, 2/6, 5/6, 1/6, and 5/6. We observe that hysteresis in the relative permeability of both phases vanishes in the limit of $\alpha \to 1$, hence recovering the formulae of Burdine, given by Eq. (5.9) or Eq. (5.2). The sum of k_{rw} and k_{rn} remains lower than unity even in this limit, which is due to the semi-empirical power-law factors for percolation effects. As the PSD becomes narrower, the there is a greater degree of symmetry between k_{rw} and k_{rn} with respect to the saturation of either phase, which is attributed to the reduced pore-radius bias.

5.2.2 Toward a microscopic theory

To achieve a more rigorous connection to our theoretical framework, we will relate the quantities in Eq. (5.6) to descriptions of pore-space morphology based on our probabilistic framework. Specifically, we will consider the relationships among the hydraulic resistances of a constant-radius pore segment, a pore branch, and a pore instance (see Section 2.2.2) in single-phase flow, which we represent with random variables $\Phi_{S,\text{sat}}$, $\Phi_{B,\text{sat}}$, and $\Phi_{I,\text{sat}}$. We will then revise these relationships when the control volume is partially saturated as described by some radius-resolved saturation of $\psi_w(F)$, and derive similar expressions for the hydraulic resistances of w-conducting (or n-conducting) constant-radius pore segments, branches, and instances, which are denoted by $\Phi_{S,w}$, $\Phi_{B,w}$, and $\Phi_{I,w}$ (or $\Phi_{S,n}$, $\Phi_{B,n}$, and $\Phi_{I,n}$), respectively. Finally, we will also model percolation effects by evaluating t_w, t_n, T_w, and T_n.

In our probabilistic framework, the axial dimension of a constant-radius pore segment follows the exponential distribution; according to Eq. (A.3), the mean axial dimension of a segment on a branch[6] is given by $1/(\lambda_{\mathbb{Z}^+} + 1/\ell)$. As explained in Section 5.2.1, depending on the definition of the pore axial coordinate, the hydraulic conductance of the pore segment may be proportional to r^m, where the scaling ex-

[6]termination of a segment on a branch can be caused by either the variation of the pore radius or the occurrence of a junction, which each follows an independent homogeneous Poisson point process (see Appendix A)

ponent may reasonable vary between 2 and 6. The distribution of $\Phi_{S,\text{sat}}$ can thus be related to the PSD following our discussion on pore-radius bias in Section 5.2.1, while the mean hydraulic resistance of a segment is proportional to and hence defined to be[7]:

$$\langle 1/\varphi_{S,\text{sat}} \rangle = \int_0^1 r^m \, \mathrm{d}F. \tag{5.14}$$

Next, we note that the hydraulic resistance of a branch is equal to the sum of its constitutive constant-radius pore segments, while the number of such segments is related to the sizes of the branch and each segment. Hence, we may approximate[8] the relationship between $\Phi_{B,\text{sat}}$ and $\Phi_{S,\text{sat}}$ with:

$$\Phi_{B,\text{sat}} = \frac{1}{1+w} \left(\Phi_{S,\text{sat}} \star \Phi_{B,\text{sat}} \right) + \frac{w}{1+w} \Phi_{S,\text{sat}}, \tag{5.15}$$

where we find it helpful to define the quantity[9]:

$$w \equiv \frac{\ell}{\langle b \rangle} = \ell \lambda_{\mathbb{Z}^+}, \tag{5.16}$$

which is analogous to the definition of q in Eq. (2.15), but concerns a pore branch rather than an entire pore-space instance. In Eq. (5.15), the "$\star$" operator denotes the convolution of the PDFs of the two random variables. Eq. (5.15) can be solved using Fourier transform, resulting in:

$$\Phi_{B,\text{sat}} = \mathscr{F}^{-1} \left\{ \frac{w \mathscr{F}\{\Phi_{S,\text{sat}}\}}{1 + w - \mathscr{F}\{\Phi_{S,\text{sat}}\}} \right\}, \tag{5.17}$$

where "$\mathscr{F}$" and "$\mathscr{F}^{-1}$" denote the Fourier transform and the inverse Fourier transform, respectively. In the limit of $w \to \infty$, each branch contains just one a constant-radius

[7]Our expressions for hydraulic conductances and resistances may be varied up to a multiplicative constant for the same porous medium because our goal here is not to derive a predictive expression for the intrinsic permeability, but rather to contrast it with the effective permeability in an unsaturated medium.

[8]The occurrences of $\Phi_{B,\text{sat}}$ and $\Phi_{S,\text{sat}}$ in Eq. (5.15) should in fact be uncorrelated. See our discussion in Appendix A.

[9]considering the result in Eq. (A.4)

pore segment, and the distributions of $\Phi_{B,\text{sat}}$ and $\Phi_{S,\text{sat}}$ collapse into one. Comparing the mean hydraulic conductances of a branch to that of a segment, we find that $\langle 1/\varphi_{B,\text{sat}} \rangle \,/\, \langle 1/\varphi_{S,\text{sat}} \rangle \in (0, 1]$, but approaches unity as $w \to \infty$.

The relationship between $\Phi_{B,\text{sat}}$ and $\Phi_{I,\text{sat}}$ follows from our discussions about branching process in Appendix A. The mean hydraulic conductances of a branch and an instance are related by[10]:

$$\Phi_{I,\text{sat}} = \Phi_{B,\text{sat}} + \sum_{z \in \mathbb{Z}^+ \setminus \{1\}} \frac{\lambda_z}{\lambda_{\mathbb{Z}^+}} \frac{1}{z-1} \Phi_{I,\text{sat}}, \tag{5.18}$$

which gives:

$$\langle 1/\varphi_{I,\text{sat}} \rangle = \left[1 - \sum_{z \in \mathbb{Z}^+ \setminus \{1\}} \frac{\lambda_z}{\lambda_{\mathbb{Z}^+}} \frac{1}{z-1} \right] \langle 1/\varphi_{B,\text{sat}} \rangle \,. \tag{5.19}$$

We will now analyze cases where the pore space is only partially saturated. A pore branch is w-conducting if and only if it does not include a pore segment containing stable nonwetting fluid. Thus, we have:

$$t_w = \frac{F_c \, \lambda_{\mathbb{Z}^+}}{\int_{F_c}^1 (1 - \psi_w(F)) \, \mathrm{d}F/\ell + \lambda_{\mathbb{Z}^+}} = \frac{w F_c}{\int_{F_c}^1 (1 - \psi_w(F)) \, \mathrm{d}F + w}, \tag{5.20}$$

which is analogous to $F_c \psi_{w,\text{im}}$ in Eq. (3.38) except that q (related to α via Eq. (2.16)) is replaced by w. Now, an instance is w-conducting if an only if its parent branch is conducting and at least one of $z-1$ the descendant instances past the z-coordinate junction is w-conducting. We have the recursion formula:

$$T_w = t_w \left(\frac{\lambda_1}{\lambda_{\mathbb{Z}^+}} + \sum_{z \in \mathbb{Z}^+} \frac{\lambda_z}{\lambda_{\mathbb{Z}^+}} (1 - (1 - T_w)^{z-1}) \right). \tag{5.21}$$

Note that it is generally not possible to derive a closed-form formula for T_w, although it is always the case that $T_w \leq t_w$. Additionally, if $\lambda_z = 0$ for $z \geq 3$, we have $T_w = t_w$ because every pore-space instance becomes a pore branch in the limit of no branching.

[10] Again, the different occurrences of $\Phi_{I,\text{sat}}$ here should in fact be independent.

The relationship between the mean hydraulic conductances of a w-conducting branch and a w-conducting instance is obtained by modifying Eq. (5.19). We have:

$$\langle 1/\varphi_{I,w} \rangle = \left[1 - \sum_{z \in \mathbb{Z}^+ \setminus \{1\}} \frac{\lambda_z}{\lambda_{\mathbb{Z}^+}} \nu(z; T_w) \right] \langle 1/\varphi_{B,w} \rangle \,, \tag{5.22}$$

where

$$\nu(z; T_w) = \sum_{y=1}^{z-1} \frac{\binom{z-1}{y} {T_w}^y (1 - T_w)^{z-1-y}}{1 - (1 - T_w)^{z-1}} \frac{1}{y}, \quad z = 3, 4, \ldots, \tag{5.23}$$

which, for a fixed T_w, attains its maximum value when $z = 3$, given by:

$$\nu(3; T_w) = \frac{-\frac{3}{2} {T_w}^2 + 2T_w}{1 - (1 - T_w)^2} = \frac{4 - 3T_w}{4 - 2T_w}. \tag{5.24}$$

The conductances of a w-conducting segment and a w-conducting branch may follow a relationship similar to Eq. (5.17); here, we make the simplifying assumption that:

$$\frac{\langle 1/\varphi_{B,\text{sat}} \rangle}{\langle 1/\varphi_{S,\text{sat}} \rangle} \approx \frac{\langle 1/\varphi_{B,w} \rangle}{\langle 1/\varphi_{S,w} \rangle}. \tag{5.25}$$

Finally, the mean hydraulic resistance of all w-conducting segment can be found given the radius-resolved saturation of the wetting phase, as explained in Section 5.2.1. We have:

$$\langle 1/\varphi_{S,w} \rangle = \frac{1}{s_w} \int_0^1 r^m \psi_w(F) \, \mathrm{d}F. \tag{5.26}$$

Substituting all of the above results into our initial proposition in Eq. (5.6), we

have:

$$
\begin{aligned}
k_{rw} &= \frac{T_w \langle 1/\varphi_{I,w} \rangle}{\langle 1/\varphi_{I,\text{sat}} \rangle} \\
&= T_w \frac{\left[1 - \sum_{z \in \mathbb{Z}^+ \setminus \{1\}} \frac{\lambda_z}{\lambda_{\mathbb{Z}^+}} \nu(z; T_w)\right] \langle 1/\varphi_{B,w} \rangle}{\left[1 - \sum_{z \in \mathbb{Z}^+ \setminus \{1\}} \frac{\lambda_z}{\lambda_{\mathbb{Z}^+}} \frac{1}{z-1}\right] \langle 1/\varphi_{B,\text{sat}} \rangle} \\
&= T_w \frac{1 - \sum_{z \in \mathbb{Z}^+ \setminus \{1\}} \frac{\lambda_z}{\lambda_{\mathbb{Z}^+}} \nu(z; T_w)}{1 - \sum_{z \in \mathbb{Z}^+ \setminus \{1\}} \frac{\lambda_z}{\lambda_{\mathbb{Z}^+}} \frac{1}{z-1}} \frac{\langle 1/\varphi_{S,w} \rangle}{\langle 1/\varphi_{S,\text{sat}} \rangle} \\
&= \frac{1 - \sum_{z \in \mathbb{Z}^+ \setminus \{1\}} \frac{\lambda_z}{\lambda_{\mathbb{Z}^+}} \nu(z; T_w)}{1 - \sum_{z \in \mathbb{Z}^+ \setminus \{1\}} \frac{\lambda_z}{\lambda_{\mathbb{Z}^+}} \frac{1}{z-1}} \frac{T_w}{s_w} \frac{\int_0^1 r^m \psi_w(F) \, \mathrm{d}F}{\int_0^1 r^m \, \mathrm{d}F},
\end{aligned}
\tag{5.27}
$$

which is still too complex to be of any practical utility. Thus, we consider the simplifications resulting from the assumption that $\lambda_z = 0$ for all $z \geq 4$. Recall that an ensemble of pore-space instances is completely characterized given λ_z for $z = 1, 3, 4, \ldots$, and ℓ. Thus, the number of parameters required to fully specify an ensemble where $\lambda_z = 0$ for all $z \geq 4$ is equal to 3. We define:

$$
\beta \equiv \frac{\langle b \rangle}{\langle c \rangle} = \frac{q}{w} \in [0, 1], \tag{5.28}
$$

which gives:

$$
\frac{\lambda_1}{\lambda_{\mathbb{Z}^+}} = \frac{1+\beta}{2}, \quad \frac{\lambda_3}{\lambda_{\mathbb{Z}^+}} = \frac{1-\beta}{2}. \tag{5.29}
$$

The ensemble is fully determined given $\alpha \in (0, 1)$, $\beta \in [0, 1]$, and ℓ (in units of the pore axial coordinate). Now we may revisit and solve Eq. (5.21) for the expected

fraction of w-conducting instances:

$$\begin{aligned} T_w &= t_w \left(\frac{\lambda_1}{\lambda_{\mathbb{Z}^+}} + \frac{\lambda_3}{\lambda_{\mathbb{Z}^+}} (1 - (1 - T_w)^{3-1}) \right) \\ 1 - \frac{T_w}{t_w} &= \frac{1-\beta}{2} (1 - T_w)^2 \\ T_w &\sim t_w \left[1 - \frac{1-\beta}{2} (1 - t_w)^2 \right], \end{aligned} \tag{5.30}$$

which is obtained by performing a regular perturbation expansion of T_w in $\lambda_3/\lambda_{\mathbb{Z}^+}$. The expression slightly overestimates T_w.

Also, with $\lambda_z = 0$ for all $z \geq 4$, the sum in Eq. (5.22) is reduced to a single term. Our simplified formula writes:

$$\begin{aligned} k_{rw} &= \frac{1 - \frac{4-3T_w}{4-2T_w} \frac{1-\beta}{2}}{1 - \frac{1}{2} \frac{1-\beta}{2}} \frac{T_w}{s_w} \frac{\int_0^1 r^m \psi_w(F) \, \mathrm{d}F}{\int_0^1 r^m \, \mathrm{d}F} \\ &= \frac{4(2 - T_w) - (1-\beta)(4 - 3T_w)}{(3+\beta)(2 - T_w)} \frac{T_w}{s_w} \frac{\int_0^1 r^m \psi_w(F) \, \mathrm{d}F}{\int_0^1 r^m \, \mathrm{d}F}, \end{aligned} \tag{5.31}$$

which, together with Eqs. (5.30) and (5.20), is our set of formulae for the relative permeability of the wetting phase. The formula for the nonwetting phase can be similarly derived, and is given by:

$$k_{rn} = \frac{4(2 - T_n) - (1-\beta)(4 - 3T_n)}{(3+\beta)(2 - T_n)} \frac{T_n}{1 - s_w} \frac{\int_0^1 r^m (1 - \psi_w(F)) \, \mathrm{d}F}{\int_0^1 r^m \, \mathrm{d}F}, \tag{5.32}$$

where, similar to Eq. (5.30), we have:

$$T_n \sim t_n \left[1 - \frac{1-\beta}{2} (1 - t_n)^2 \right], \tag{5.33}$$

and similar to Eq. (5.20), we have:

$$t_n = \frac{w(1 - F_c)}{\int_0^{F_c} \psi_w(F)\,\mathrm{d}F + w}. \tag{5.34}$$

Eqs. (5.31) and (5.32) are plotted in Figure 5-2 for various α, β, and PSDs. We select $m = 2$ as before. Compared to our semi-empirical formulae (Eqs. (5.11) and (5.12)) and the formulae of Burdine (Eq. (5.2)) and Mualem (Eq. (5.3)), the model produces a much richer set of behaviors.

Firstly, the true capillary bundle limit is reached when $\alpha \to 1$ and $\beta = 1$, which corresponds to negligible pore-radius variation and branching. The result is that we have $k_{rw} + k_{rn} = 1$ for all $s_w \in [0, 1]$, as shown in three panels in the top row of Figure 5-2, meaning that percolation effects are completely absent and all of the pore space is invariably contributing to the flow of either one of the fluid phases. In the limit where the PDF of the PSD becomes a delta function, we obtain $k_{rw} = s_w$ and $k_{rn} = 1 - s_w$.

Secondly, with $\alpha \to 1$, hysteresis in relative permeability hysteresis is always absent, but reducing β lowers the value of $k_{rw} + k_{rn}$ for intermediate saturations, which may achieve a similar effect as the empirical power-law factors in the formulae of Burdine (Eq. (5.2)) and Mualem (Eq. (5.3)). We can observe this effect by comparing panels in the first, fourth, and seventh rows of Figure 5-2.

Thirdly, as the PSD grows wider, we clearly observe an increase in pore-radius bias, with the asymmetry between k_{rw} and k_{rn} becoming more prominent. This is especially true when α is simultaneously lowered, where the hysteresis in k_{rn} is greatly enhanced compared to that in k_{rw}.

Despite the extensive simplifying assumptions involved in the derivation of Eqs. (5.31) and (5.32), we find that these formulae produce relative permeability curves that possess a number of features that can be linked to concepts in pore-space morphology in our probabilistic framework. In future research, these connections can be investigated further, and the formulae should be tested and potentially validated by macroscopic data, although it would admittedly be much more difficult than what we have done

with mercury porosimetry in Chapter 4 for capillary pressure hysteresis.

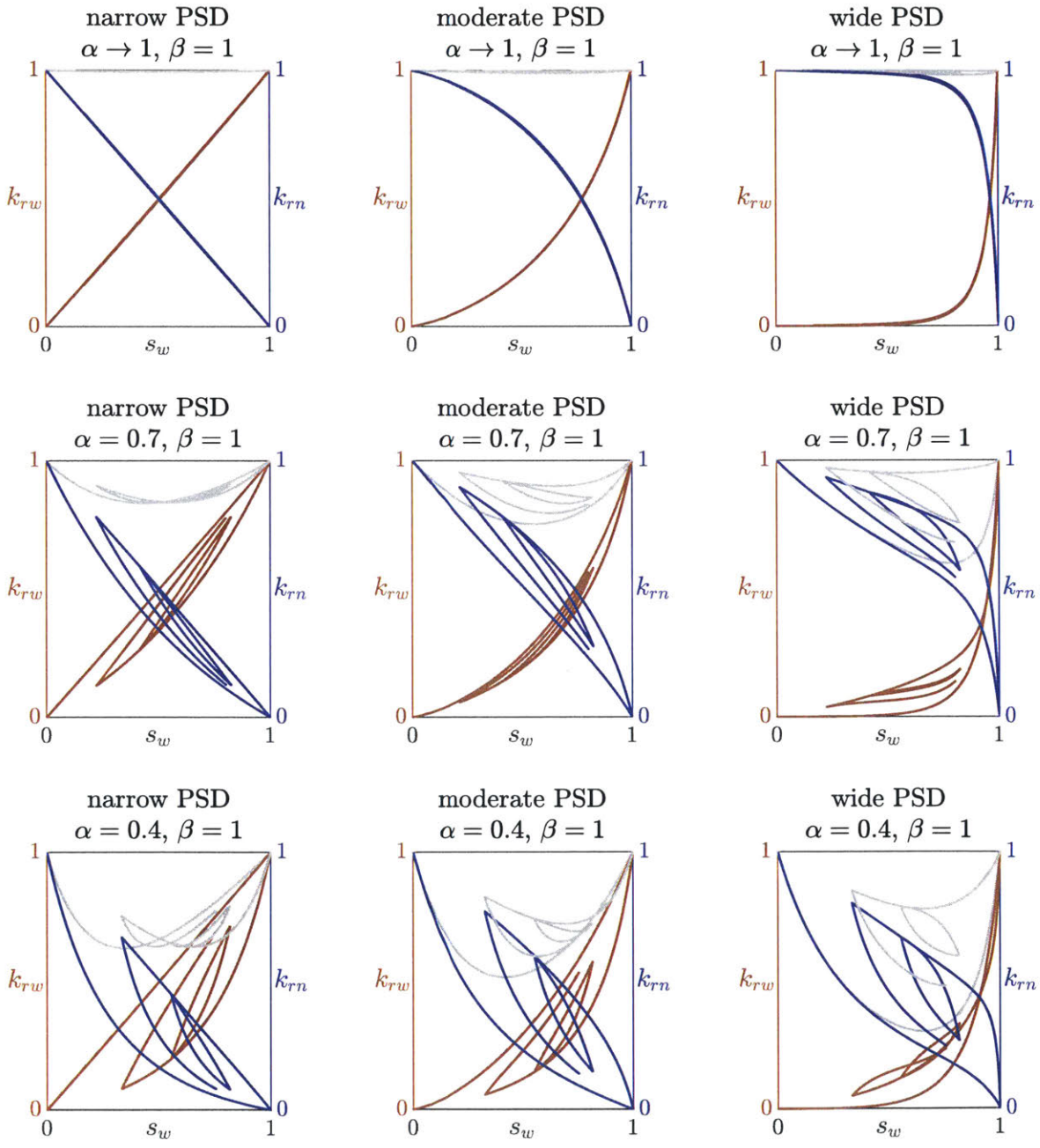
narrow PSD
$\alpha \to 1,\ \beta = 1$
moderate PSD
$\alpha \to 1,\ \beta = 1$
wide PSD
$\alpha \to 1,\ \beta = 1$
narrow PSD
$\alpha = 0.7,\ \beta = 1$
moderate PSD
$\alpha = 0.7,\ \beta = 1$
wide PSD
$\alpha = 0.7,\ \beta = 1$
narrow PSD
$\alpha = 0.4,\ \beta = 1$
moderate PSD
$\alpha = 0.4,\ \beta = 1$
wide PSD
$\alpha = 0.4,\ \beta = 1$
k_{rw}
k_{rn}
s_w
0
1

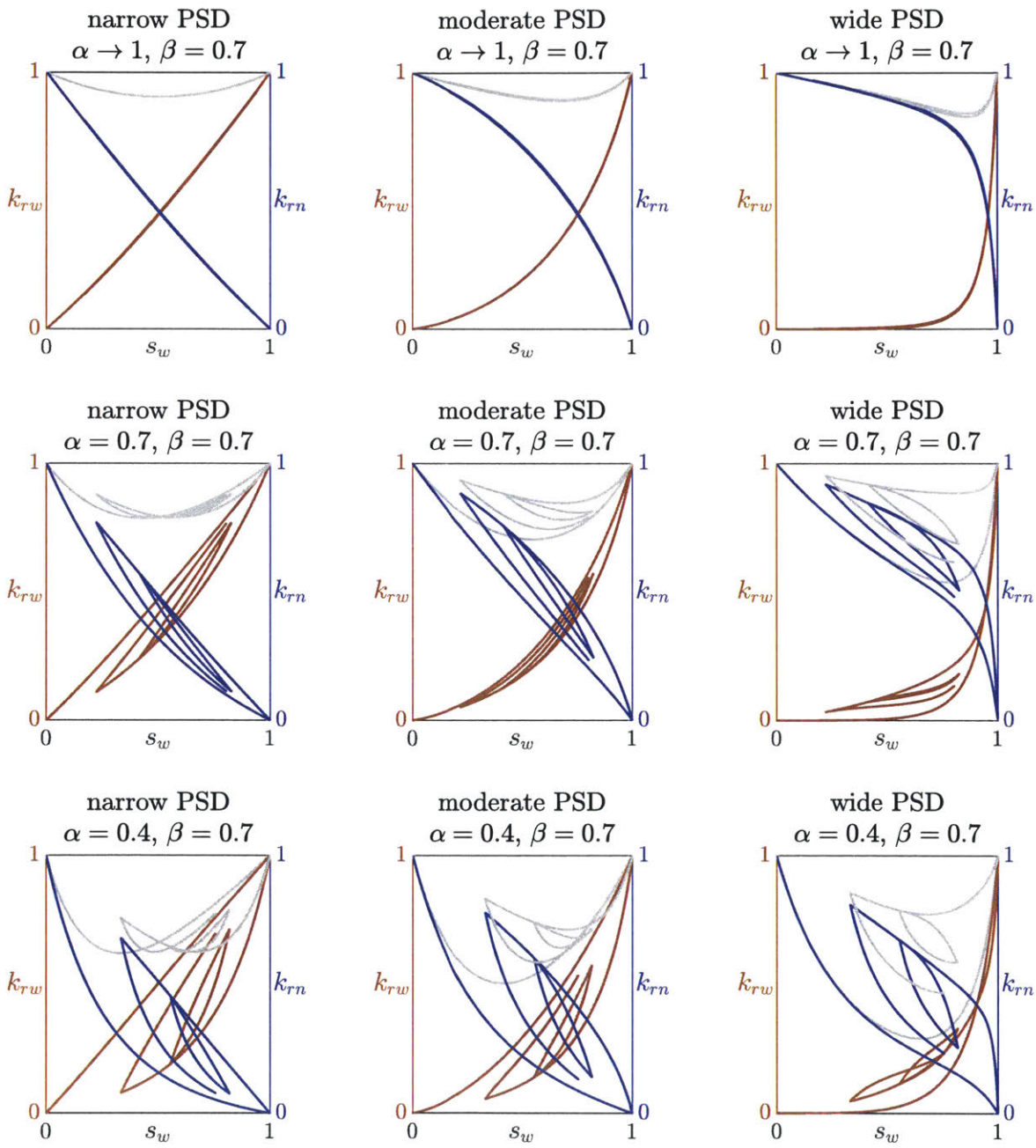
narrow PSD
$\alpha \to 1$, $\beta = 0.7$
moderate PSD
$\alpha \to 1$, $\beta = 0.7$
wide PSD
$\alpha \to 1$, $\beta = 0.7$
narrow PSD
$\alpha = 0.7$, $\beta = 0.7$
moderate PSD
$\alpha = 0.7$, $\beta = 0.7$
wide PSD
$\alpha = 0.7$, $\beta = 0.7$
narrow PSD
$\alpha = 0.4$, $\beta = 0.7$
moderate PSD
$\alpha = 0.4$, $\beta = 0.7$
wide PSD
$\alpha = 0.4$, $\beta = 0.7$
k_{rw}
k_{rn}
s_w
0
1

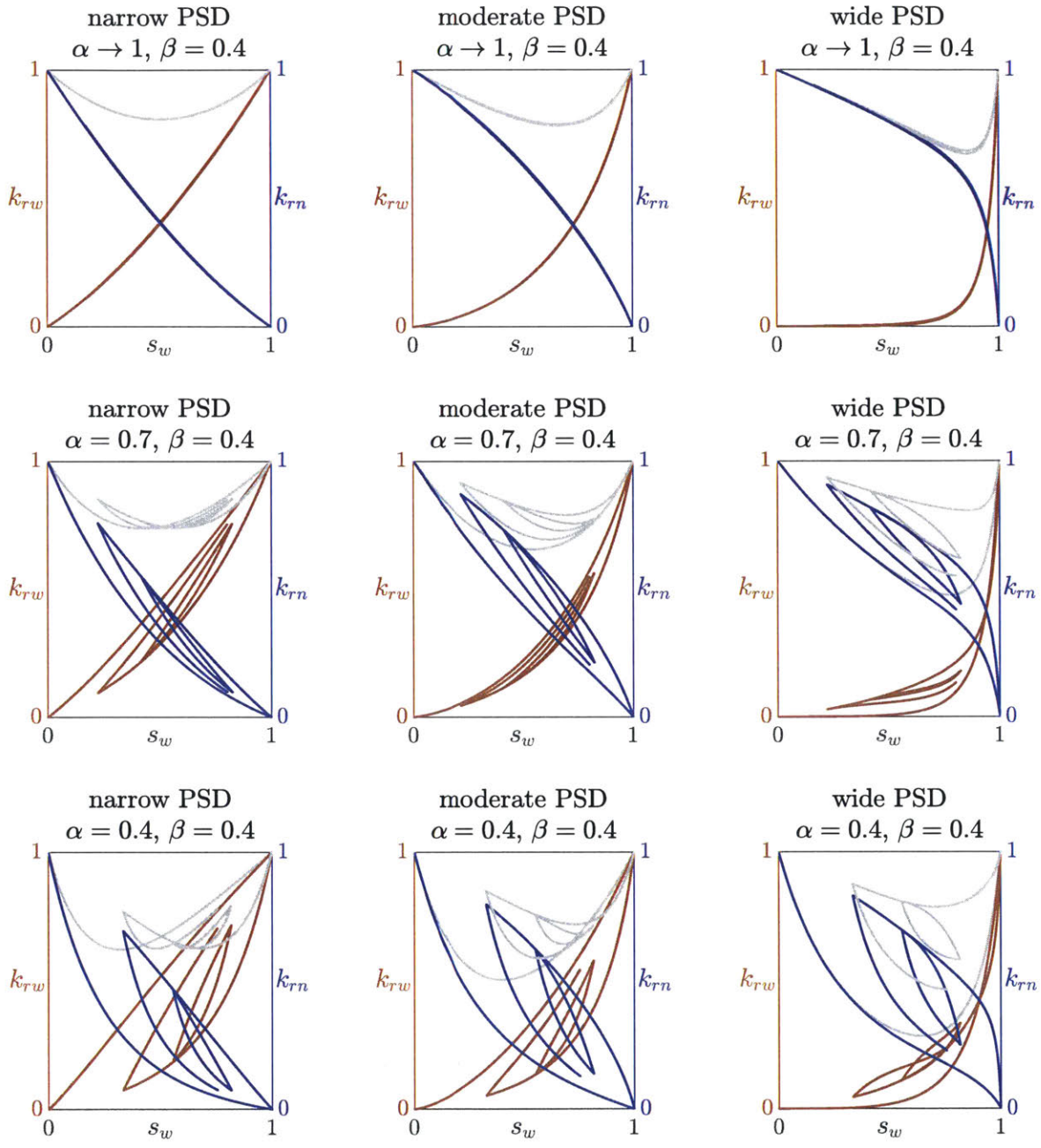

Figure 5-2: Scanning curves of the k_{rw} (red curves), k_{rn} (blue curves), as well as $k_{rw} + k_{rn}$ (gray curves) versus s_w predicted by Eqs. (5.31) and (5.32) (m=2) for three different accessivities ($\alpha \to 1$, $\alpha = 0.7$, and $\alpha = 0.4$), three different values of β (1,0.7, and 0.4), and three different PSDs (log-normal distribution with $\mu = 0$ and $\sigma = 0.01$, $\sigma = 0.5$, and $\sigma = 2$, where μ and σ are the mean and standard deviation of the associated normal distribution).

Chapter 6

Application to continuum simulation of multiphase flow in porous media

Continuum simulation of multiphase flow in porous media is perhaps the most relevant application in the scope of this thesis, where the various models presented in Chapters 3 and 5 can serve as constitutive relationships for capillary pressure and relative permeabilities that include hysteresis effects. In this chapter, we will show some preliminary results that demonstrate the application of our theoretical framework to conventional continuum simulation of multiphase flow.

6.1 General formulation and solution

Recall the system of governing equations in the conventional continuum model of immiscible two-phase flow in porous media given in Eqs. (1.2)–(1.5). We will now consider its numerical solution under a few assumptions. Firstly, we modify Eq. (1.2) by adding a source term[1] to the right-hand side of the conservation equation of each fluid, which we denote by Ξ_w and Ξ_n for the wetting and nonwetting phases, respectively. These terms will allow us to describe uniform fluid injection and extraction in a computational cell. Secondly, we consider 2-D horizontal flows, where the effects of gravity are absent, allowing us to drop the hydrostatic stress terms in Eq. (1.3).

[1] with units of the reciprocal of time

Thirdly, for convenience of notation, we define a set of transport coefficients called **effective mobilities**:

$$\kappa_w \equiv k_s k_{rw}/\mu_w, \quad \kappa_n \equiv k_s k_{rn}/\mu_n, \quad \kappa_T \equiv \kappa_w + \kappa_n, \tag{6.1}$$

which may vary during flow due to changes in the relative permeabilities of the two phases.

Under these circumstances, Eq. (1.2) for the nonwetting phase becomes what we shall refer to as the **saturation equation**:

$$\phi \frac{\partial s_n}{\partial t} = \nabla \cdot (\kappa_n \nabla p_n) + \Xi_n, \tag{6.2}$$

while summing the conservation equations for the two phases given in Eq. (1.2) and substituting in Eqs. (1.3), (1.4), and (1.5) result in the **pressure equation**:

$$\nabla \cdot (-\kappa_T \nabla p_n + \kappa_w \nabla p_c) = \Xi_w + \Xi_n. \tag{6.3}$$

The reformulation of Eqs. (1.2)–(1.5) is now complete given appropriately chosen constitutive relationships for p_c, k_{rw}, and k_{rn}. The state variables in this formulation are $s_n(\mathbf{x}, t)$ and $p_n(\mathbf{x}, t)$, from which the saturation and pressure of the wetting phase may be computed if desired.

As we propose in Chapters 3 and 5, in our probabilistic framework, hysteretic-enabling constitutive relationships for capillary pressure and relative permeabilities rely on the radius-resolved saturation function as an additional continuum-scale descriptor of the state of pore-scale fluid distribution. In general, we may write radius-resolved saturation as $\psi_w(F, \mathbf{x}, t)$, which would be equivalent to an infinite-dimensional vector that depends on space and time – we will discuss its representation using a finite number of variables in due course. Putting that aside, we may regard $\psi_w(F, \mathbf{x}, t)$ as a collection of auxiliary variables that participate in the algebraic constitutive relationships but not the PDEs.

The above formulation of two-phase flow, including Eqs. (6.2) and (6.3) and appro-

priate constitutive relationships, is commonly solved numerically using what is called the **Implicit Pressure Explicit Saturation (IMPES) scheme**. In this numerical scheme, we march forward in time from t^k to t^{k+1}, where the superscripts denote the indices of two adjacent time steps by sequentially updating the state variables in our model, which are denoted by $s_n(\mathbf{x}, t^k)$, $p_n(\mathbf{x}, t^k)$, and $\psi_w(F, \mathbf{x}, t^k)$ at the current time step. To advance to the next time step, the following calculations are carried out, in the order they are listed[2]:

1. *Computation of capillary pressure*: we compute p_c from F_c at the current time step using the prescribed PSD, which maps F_c to r_c, and Eq. (2.10), which maps r_c to p_c. Note that F_c is either supplied as part of the initial conditions or obtained during the update of the radius resolved saturation in the previous time step (see "implicit radius-resolved saturation update").

2. *Implicit pressure update*: we solve implicitly for $p_n(\mathbf{x}, t^{k+1})$ in the discretized form of Eq. (6.3).

3. *Explicit saturation update*: we march in time explicitly[3] to find $s_n(\mathbf{x}, t^{k+1})$ in Eq. (6.2).

4. *Computation of relative permeabilities*: we use $\psi_w(F, \mathbf{x}, t^k)$ to compute k_{rw} and k_{rn}, using either our semi-empirical formulae (Eqs. (5.11) and (5.12)), formulae based on our microscopic theory (Eqs. (5.31) and (5.32)), or other empirical formulae (such as (5.1)), and subsequently the effective mobilities in Eq. (6.1).

5. *Implicit radius-resolved saturation update*: given the new $s_n(\mathbf{x}, t^{k+1})$, we solve implicitly for the F_c to which we must subject $\psi_w(F, \mathbf{x}, t^k)$ so that the resulting new radius-resolved saturation, $\psi_w(F, \mathbf{x}, t^{k+1})$, integrates to the required conventional saturation based on Eq. (3.11) (see further discussions below).

[2]Note that in some cases, steps 1 and 2 may be carried out less frequently in the so-called "outer loop", while the remaining steps are carried out at all time steps in the so-called "inner loop". This speeds up the simulation at the cost of its accuracy because since step 2 is typically the most expensive step computationally. For all results presented in this chapter, we do indeed carry out all updates at each time step without such a distinction between outer and inner loops.

[3]namely, approximating the time derivative by the forward Euler method

The last step represents the main difference between the proposed formulation and its conventional counterpart. Now, as we see in Chapter 3, it is more "natural" to update the radius-resolved saturation by subjecting it to a new F_c, rather than a new s_w, which corresponds to the area under the curve of $\psi_w(F)$. Thus, the implicit determination of $\psi_w(F, \mathbf{x}, t^{k+1})$ in the above scheme is a somewhat expensive step. However, since the radius-resolved saturation profiles in different computational cells are independent from one another, the computational cost associated with solving for $\psi_w(F, \mathbf{x}, t^{k+1})$ only scales linearly with the number of computational cells considered. In future research, it may be of interest to consider model formulations[4] that avoid the prescription of s_w in updating the radius-resolved saturation.

Now we shall now discuss the data structure for representing the radius-resolved saturation function, $\psi_w : [0,1] \to [0,1] : F \mapsto \psi_w(F)$, for a given $\mathbf{x}$ and t. Perhaps the most unpretentious approach is to simply discretize the domain of F into N fixed, equal-size intervals, so that the components of some vector $\boldsymbol{\psi}_w \in [0,1]^N$ give the average values of the radius-resolved saturation in the corresponding intervals of F. However, because $\psi_w(F)$ may contain step discontinuities as seen in Eq. (3.38), a large N may be required to accurately represent $\psi_w(F)$ – we observe that the s_w–F_c becomes bumpy at the edges of the intervals of F if a small N is chosen, which may create artifacts in the simulation results.

On that account, we propose to represent the radius-resolved saturation as a piecewise-constant function with variable intervals of F:

$$\psi_w(F) = \begin{cases} y_1 & 0 \leq F \leq x_1 \\ y_i & F \in (x_{i-1}, x_i], \quad i = 2, \ldots, N-1 \\ y_N & x_{N-1} < F \leq 1, \end{cases} \tag{6.4}$$

so that the radius-resolved saturation is represented by $\mathbf{x} \in [0,1]^{N-1}$ and $\mathbf{y} \in [0,1]^N$, where $N = 1, 2, \ldots$, which constitute $(2N-1)$ numerical quantities to store at each

[4]Examples to study include the mixed formulation of the Richards equation [185] and the careful splitting of higher-order PDEs into DAEs [95].

computational cell. Note that the components of $\mathbf{x}$ must always be sorted in ascending order. The amount of data required to recreate $\psi_w(F)$ is generally far fewer using this representation compared to discretizing F into fixed intervals. For instance, if a computational cell is undergoing primary drainage, then according to Eq. (3-5), $N = 2$ is sufficient for representing $\psi_w(F)$ exactly at all times; if the direction of change of F_c is suddenly reversed, then $N = 3$ would suffice for the resulting $\psi_w(F)$. The N required to reproduce $\psi_w(F)$ exactly becomes large if the saturation of the control volume oscillates over time with decaying magnitudes[5], which may be countered by specifying a maximum allowed N at the expense of creating some discretization error. Also, when using this data structure, according to Eq. (3.11), we may evaluate the conventional saturation with:

$$s_w = x_1 y_1 + \sum_{i=2}^{N-1} (x_i - x_{i-1}) y_i + (1 - x_{N-1}) y_N. \tag{6.5}$$

We can then update $\mathbf{x}$ and $\mathbf{y}$ at each time step according to Eq. (3.38). Specifically, we insert into $\mathbf{x}$ a new component that equals the new value of F_c, which correspondingly creates a duplicate of the component y_i where i is such that, either, x_{i-1} is the largest component of the previous $\mathbf{x}$ that is smaller F_c, or, $i = 1$ if no such x_i exists. Also, if adjacent components in $\mathbf{y}$ are equal, i.e., $y_i = y_{i+1}$ for some $i \in \{1, \ldots, N-1\}$, then it is acceptable to remove both x_i and y_i from $\mathbf{x}$ and $\mathbf{y}$ respectively to free up storage, if desired.

6.2 Sample simulation results

In this section, we briefly report results of two simulation studies[6] carried out using the model formulation and numerical scheme presented so far. The key finding is that the constitutive relationships we propose for capillary pressure and relative permeabilities allow for the natural prediction of hysteresis as a result of the dynamics of the wetting-

[5] As a purely hypothetical example, consider a oscillating s_w trajectory whose end points form the sequence $\left(((-0.99)^k + 1)/2\right)_{k=0}^{\infty}$.

[6] performed by coauthor Mohammad Amin Amooie

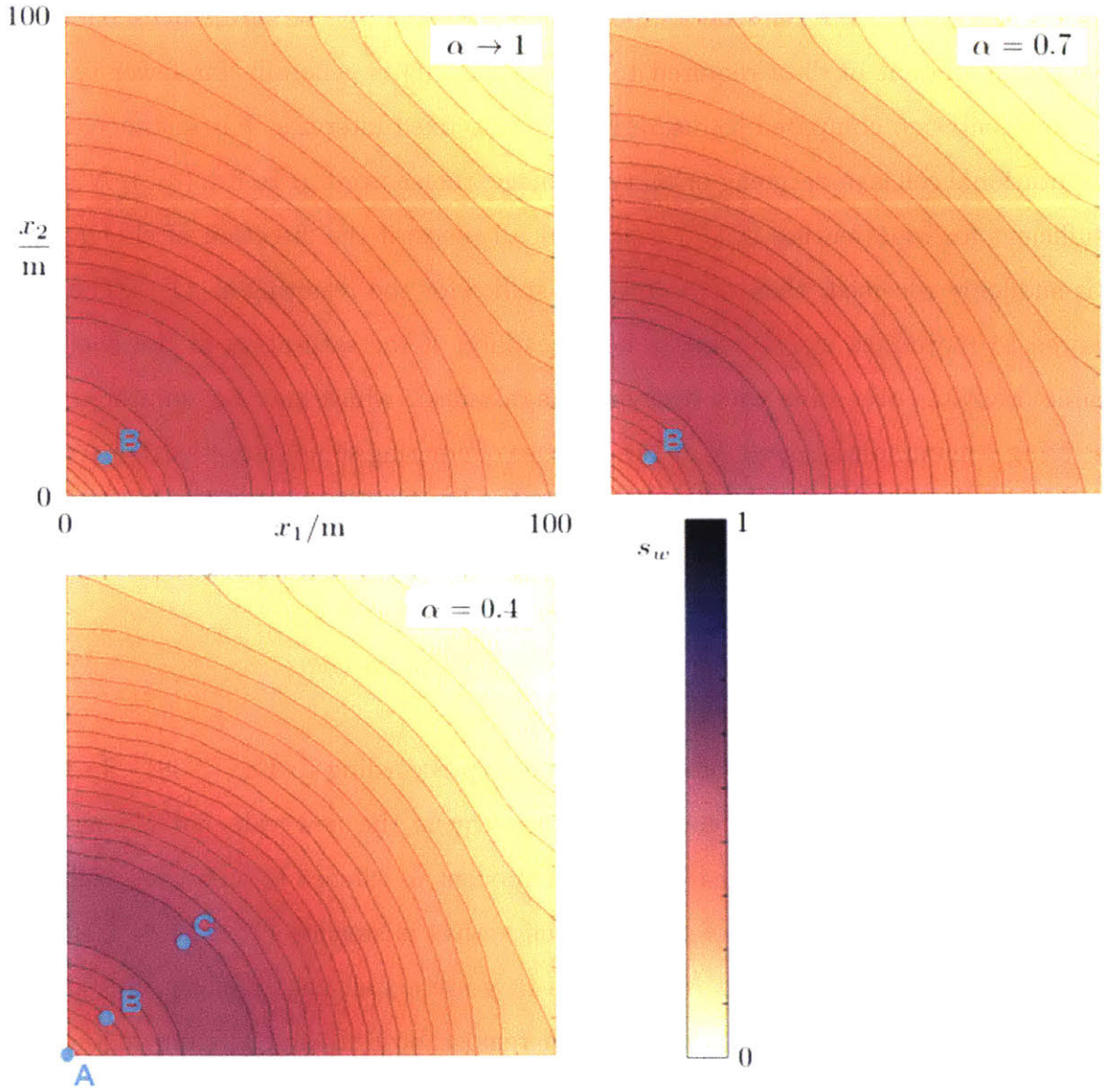

Figure 6-1: Contour plots of the saturation of the wetting phase at $t = 1$ year during irregular injection in domains with accessivities of $\alpha \to 1$, $\alpha = 0.7$, and $\alpha = 0.4$. Three locations in each domain, A = (0 m, 0 m), B = (0.1 m, 0.1 m), and C = (0.25 m, 0.25 m) are marked with light-blue circles.

phase radius-resolved saturation, while the strength of the hysteresis effects can be tuned by altering the pore-space accessivity.

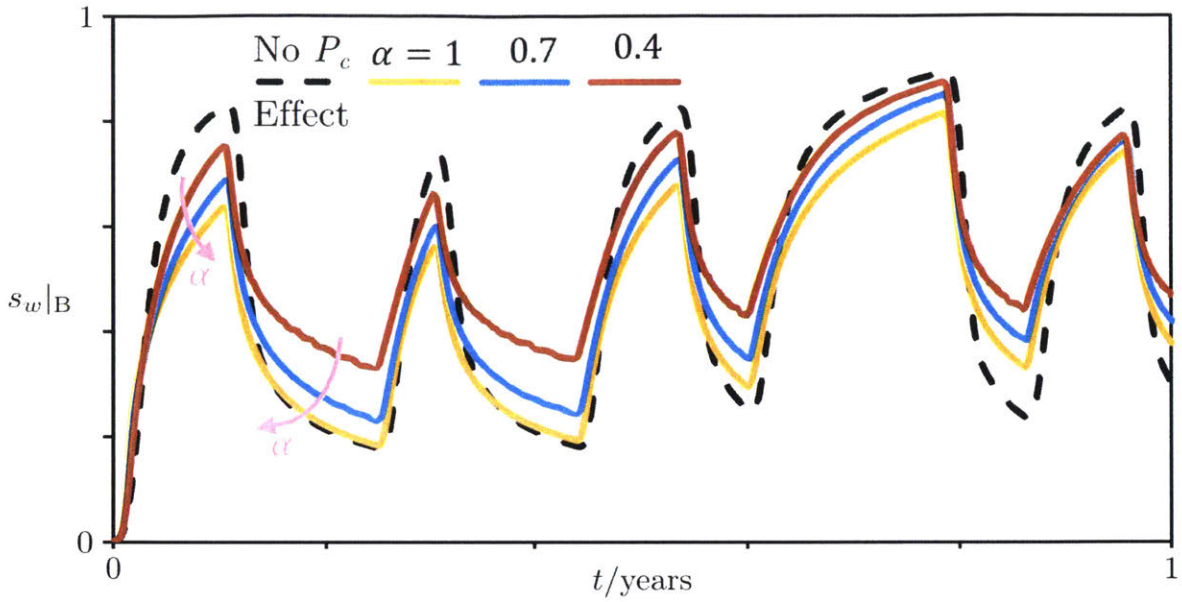

Figure 6-2: Time series of the wetting-phase saturations at location B (as identified in Figure 6-1) during irregular injection in domains with accessivities of $\alpha \to 1$, $\alpha = 0.7$, and $\alpha = 0.4$, which are given by the yellow, light-blue, and red curves, respectively. The dashed black curve shows the time series for the case where we set $p_c = 0$ at all locations and at all times in the simulation.

6.2.1 Alternating injection in a 2-D domain with capillary pressure hysteresis alone

In this first study, we consider the case where hysteresis is only present in the p_c–s_w relationship, but not in the relative permeabilities – they were modeled using the empirical formulae of Corey, or Eq. (5.1). The system domain was 100 m by 100 m in size, and was initially saturated with the nonwetting phase, so that $\psi_w(F, \mathbf{x}, 0) = 0$ and $s_n(\mathbf{x}, 0) = 1$ for all $F \in [0, 1]$ and $\mathbf{x} \in [0, 100 \text{ m}]^2$. The domain was divided into 20 by 20 computational cells. The normal flux density at each point on the outer boundary of the domain was kept at zero at all times. We injected the wetting and nonwetting fluids alternately in the lower-left corner of the domain near $\mathbf{x} = (0 \text{ m}, 0 \text{ m})$ by prescribing Ξ_w and Ξ_n in the corresponding computational cell in a time-dependent fashion. Both regular and irregular cycles of injection were considered. For regular injection, we switched between the two phases every 1 year; for irregular injection, the wetting phase was injected for $t/\text{year} \in [0, 1) \cup [2.5, 3) \cup [4.4, 5.3) \cup [6, 7.8) \cup [8.6, 9.5)$

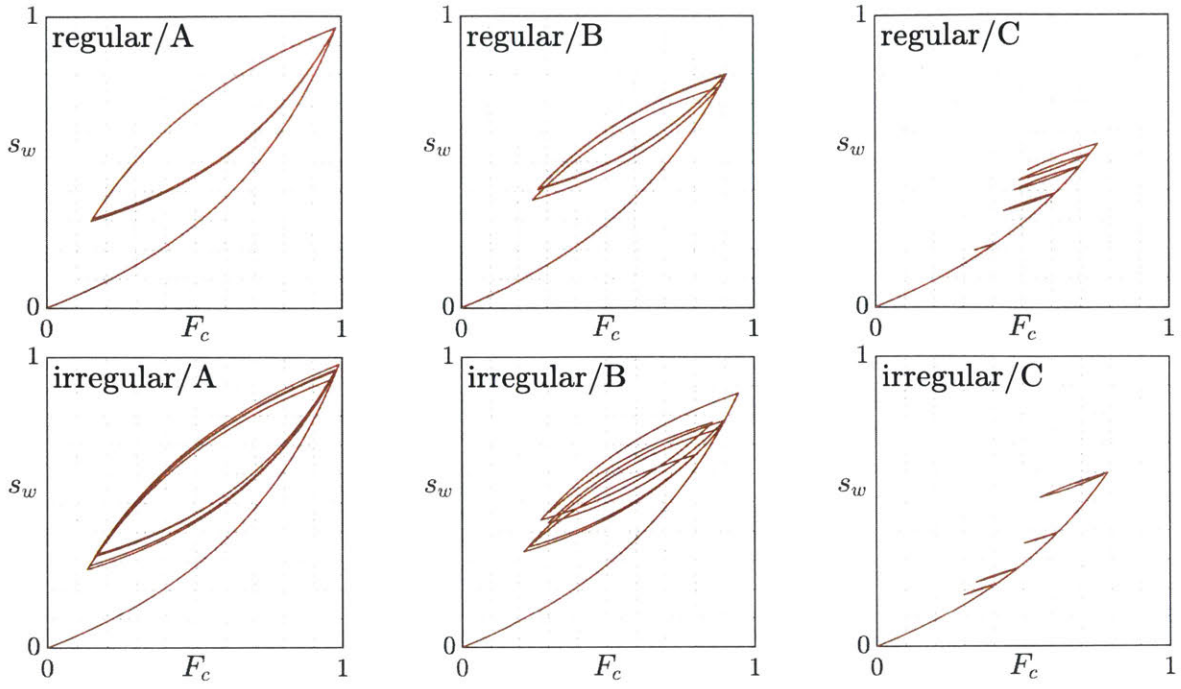

Figure 6-3: Trajectories of s_w versus F_c at A = (0 m, 0 m), B = (10 m, 10 m), and C = (100 m, 100 m) (see labels in Figure 6-1) over the courses of the simulations. The top three panels and the bottom three panels correspond to regular and irregular injections, respectively. Accessivity in set to 0.4 in all cases shown. The convectional saturations are obtained by integrating the radius-resolved saturations as specified in Eq. (3.11), leading to the natural prediction of diverse hysteresis behaviors.

and the nonwetting phase for the remaining time. Other constant properties in the simulation included: $\phi = 0.22$, $k_s = 2.5 \times 10^{-12}$ m^2, $\mu_w = \mu_n = 1 \times 10^{-3}$ Pa s.

Saturation profiles at $t = 1$ year during irregular injection are shown in Figure 6-1 for three values of accessivity, while the saturation time series at (10 m, 10 m) for the same conditions are plotted in Figure 6-2, in addition to the case where p_c is set to zero at all times. It appears that lower accessivities result in higher wetting-phase saturations during both drainage and imbibition. The F_c–s_w trajectories at points A, B, and C (as identified in Figure 6-1) over time in six simulation runs are shown in Figure 6-3 for both regular and irregular cycles of fluid injection. Here, we have $\alpha = 0.4$. Again, we emphasize that these hysteretic scanning curves are inherently predicted by the internal dynamics of $\psi_w(F, \mathbf{x}, t)$ in the simulations. We observe diverse hysteresis behaviors at different locations in the domain for different injection

conditions.

6.2.2 Simulation with both capillary pressure and relative permeability hystereses

We repeat these simulations using the constitutive relationships for relative permeabilities presented in Section 5.2.2. Here, as an illustrative example, we set $\alpha = 0.4$ and $\beta = 0.4$, and consider a "wide" log-normal distribution for the PSD with parameters $\mu = 0$ and $\sigma = 1$, which is the same as those chosen to generate the scanning curves in the bottom-right panel of Figure 5-2. Figure 6-4 is the contour plot of the saturation field at the end of the simulation, while Figure 6-5 includes the time series of the saturations of the wetting phase at three locations marked in Figure 6-4. The s_w–F_c, k_{rw}–s_w, and k_{rn}–s_w trajectories at the same three locations are shown in Figure 6-6. Again, the hysteresis observed naturally follows from the internal dynamics of the radius-resolved saturation function. This example demonstrate that our constitutive laws for capillary pressure and relative permeabilities are inherently able to account for hysteresis effects in continuum simulations of multiphase flow in porous media.

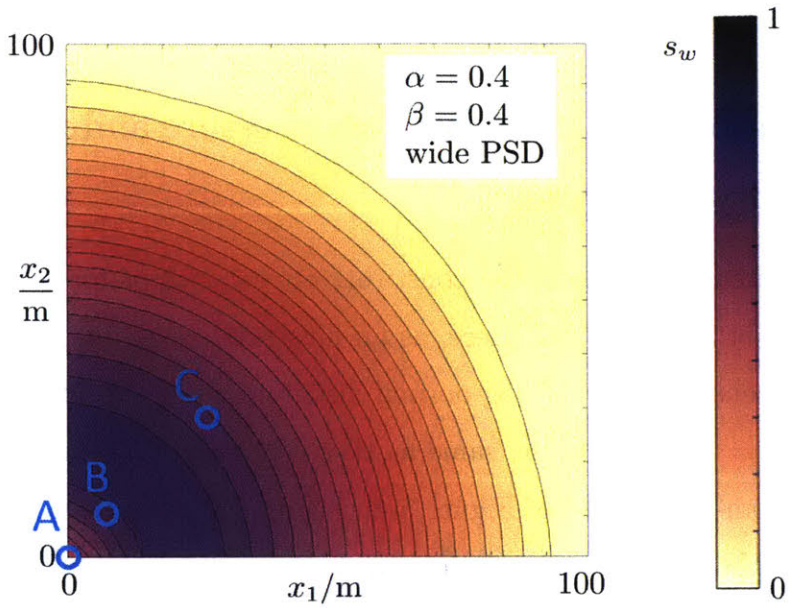

Figure 6-4: Contour plots of the saturation of the wetting phase at $t = 1$ year during irregular injection in a domain with $\alpha = 0.4$, $\beta = 0.4$, and a wide PSD (log-normal distribution with $\mu = 0$ and $\sigma = 1$, where μ and σ are the mean and standard deviation of the associated normal distribution). Three locations in each domain, A = (0 m, 0 m), B = (0.1 m, 0.1 m), and C = (0.25 m, 0.25 m) are marked with light-blue circles.

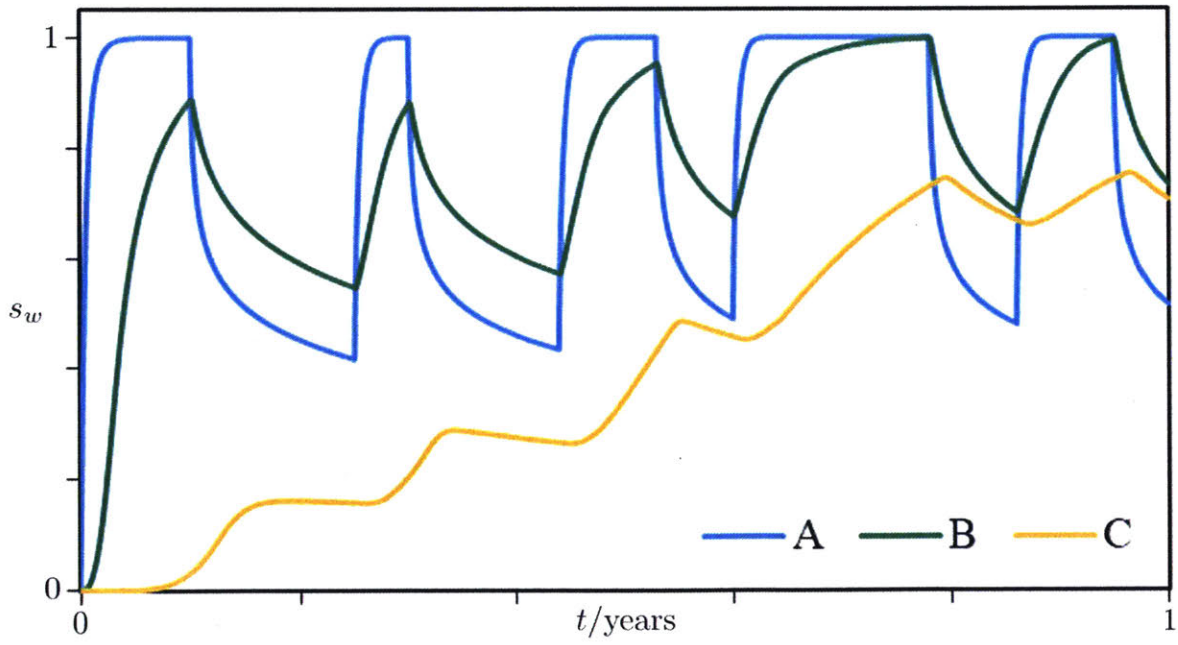

Figure 6-5: Time series of the wetting-phase saturations at three locations (as identified in Figure 6-4) during irregular injection in a domain with $\alpha = 0.4$, $\beta = 0.4$, and a wide PSD.

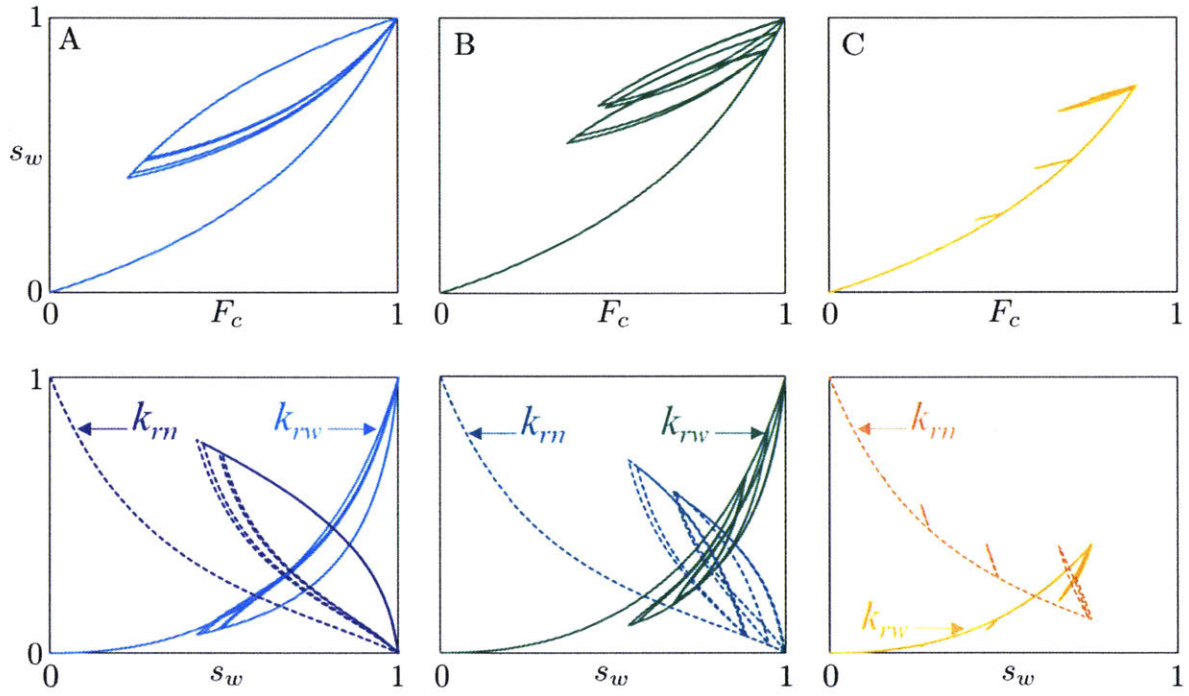

Figure 6-6: Trajectories of s_w versus F_c (top panels), k_{rw} versus s_w (bottom panels, solid curves), and k_{rn} versus s_w (bottom panels, dashed curves) at A = (0 m, 0 m), B = (10 m, 10 m), and C = (100 m, 100 m) (see labels in Figure 6-4) over the course of the simulation.

Chapter 7

Miscellaneous topics

In this chapter, we will touch on a few shorter topics that may not each warrant a standalone chapter. Some deal with computational works that support, illustrate, or partially validate our theory, while others demonstrate the possible extension of the continuum modeling concepts proposed in this thesis to other physical processes in porous media.

7.1 Invasion percolation simulation

In this section, we briefly summarize the use of invasion percolation simulations to validate our microscopic theory of capillary pressure hysteresis. As we have alluded to in Chapters 3, 4, and 5, **percolation theory** has been applied extensively to model various processes in porous media [45, 19, 104], including capillary pressure [186] and relative permeabilities [187] in multiphase flow. In a nutshell, in classical percolation theory, we prescribe the probability that each sites (or bonds) of a regular lattice are "occupied", and then study the statistics of clusters, which are collections of adjacent occupied sites (or bonds). It turns out that we are only able to derive analytical expressions of key statistics of clusters on very simple networks, such as one-dimensional chains and Bethe lattices, although certain scaling results can be obtained for other lattices. The concept of **invasion percolation** was put forth [188] to describe cases where the occupation of a site (or bond) is not completely at

random, but conditional on at least one of the neighbouring sites (or bonds) already being occupied. This is extremely relevant to multiphase flow because many pore-scale processes cannot occur without access via a continuous path through a fluid phase to the exterior of the control volume.

Since many percolation problems can only be solved numerically, they are also closely related to **pore-network simulations**. The idea of pore-network modeling was first put forward in the seminal paper of Fatt [189], who proposed using 2-D regular networks of "tubes of randomly distributed radii" to examine capillary pressure and relative permeabilities. For example, the primary drainage curve is simulated in such a pore-network model by considering invasion percolation: the network is initially filled with the wetting phase, and the nonwetting phase then invades the network from its boundary on rising capillary pressure. A tube is allowed to drain only if it both has a large enough radius according to Eq. (2.10), and has direct access to the wetting phase via one of its neighboring tubes. Fatt's model is extended to give what later becomes the standard setup in the pore-network modeling approach, where the pore space is formed by joining wide, rounded pores and narrow, channel-like throats on 2- or 3-D lattices [150, 122]. Additional parameters and probability densities are introduced to characterize the geometry and connectivity of the pore space. These degrees of freedom are then tuned so that the model predictions match relevant experimental results.

The pore-space instances considered in our probabilistic framework appear much simpler in comparison, both in terms of geometrical and topological features. It is therefore of interest to investigate the concepts in our framework in the contexts of pore-network simulations. Here, we will simulate invasion percolation on two-dimensional square lattices and compare the results against our theory.

Firstly, we construct an N-by-N square lattice whose bonds or edges are assigned random "pore radii". Recall from Section 2.1.3 that we find it advantageous to refer to a particular pore size by F, or the volume fraction of all pore slices in the sample that are smaller than the given size. This way, we may simply assign to each edge on the lattice an F drawn randomly and uniformly from the interval $[0, 1]$, obviating the need

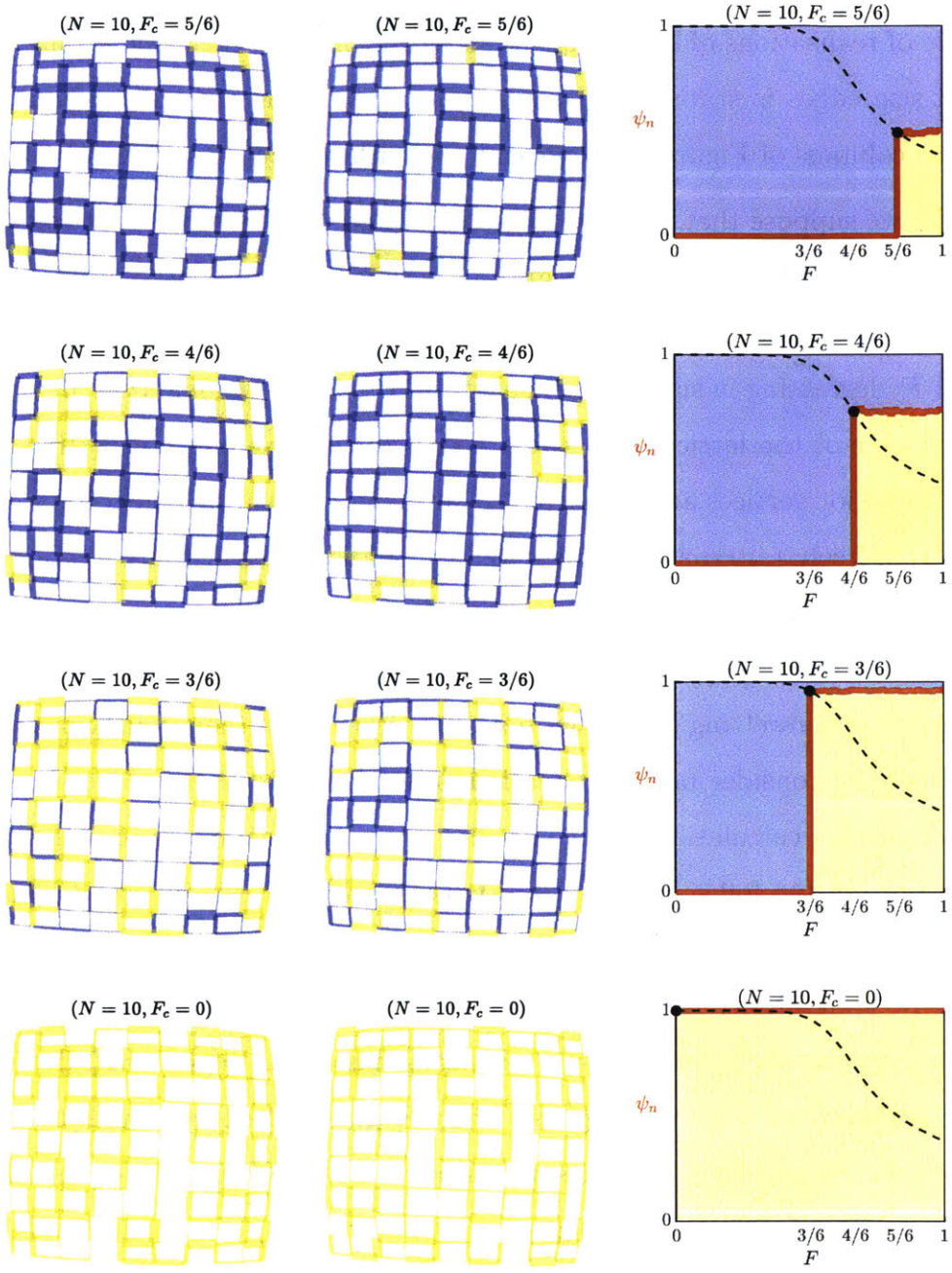

Figure 7-1: Each of the leftmost two columns depicts quasistatic drainage on a two-dimensional square lattice with side length $N = 10$, showing the fluid distribution at various F_c as it decreases from 1 to 0. The thickness of each edge corresponds to its $F(r)$, where r is its randomly assigned pore radius. The rightmost column displays the corresponding radius-resolved saturation of the nonwetting phase, $\psi_n(F)$, as red curves, based on a total of 2 000 independent trials. The shaded areas represent saturations of the two phases (see Eq. (3.11)). The black dashed curve shows the trajectory of the mean value of ψ_n for $F_c < F \leq 1$ as a function of F_c (see Eq. (3.34)).

for prescribing a PSD. Repeating this process a great number of times would result in an ensemble of realizations of lattices of the same dimensions, where the arrangement of different-size edges is statistically similar, but distinct in each realization. The leftmost two columns of Figure 7-1 represent two such realizations with $N = 10$.

Secondly, we suppose that the pore space is initially filled with the wetting phase only (represented by the blue fluid in Figure 7-1), which would undergo drainage as it is replaced by the nonwetting phase (represented by the yellow fluid in Figure 7-1) in response to F_c decreasing in small increments from 1 to 0. We assume that all vertices on the perimeter of the lattice have direct access to the invading nonwetting fluid, and that all interior vertices are connected to sinks, into which the defending wetting fluid may drain freely (alternatively, we may assume that the defending wetting fluid is indefinitely compressible, like the vacuum phase in mercury intrusion porosimetry). Under quasistatic conditions, at any prescribed F_c, each edge may be filled with either the wetting or the nonwetting phase, but not both. We neglect the capacity of vertices on the lattice, and consider bond percolation only (similar to [189]). Like in typical invasion percolation calculations, an edge filled with the wetting phase will drain if and only if both of the following two conditions are satisfied: (1) its size F is larger than the imposed F_c; (2) at least one of its vertices belongs to an edge that is filled with the nonwetting phase. As we see in either of the first two columns of Figure 7-1, the n phase replaces the w phase in an increasing number of edges as F_c decreases, until all edges are filled with the n phase when F_c goes to zero, although the exact invasion percolation pattern is not the same in each realization due to the randomness in the arrangement of different-size pores.

Thirdly, we compute the radius-resolved saturation of the nonwetting phase at each F_c, denoted by $\psi_n(F; F_c)$, by tallying edges of each size (given by F) filled with either fluid (w or n), across all realizations of lattices with the same prescribed side length. For example, at $F_c = 4/6$, we find that among all edges of sizes near $F = 0.81$ (i.e., in some small interval centered at this value depending on the discretization level) across a total of 2 000 realizations of $N = 10$ lattices, 71.7% are filled with the nonwetting phase and the rest are filled with the wetting phase; therefore, $\psi_n(F =$

$0.81; F_c = 4/6) = 0.717$, as we may identify in the second plot in the rightmost column of Figure 7-1. Similarly, the figure also contains $\psi_n(F)$ at other selected F_c. We observe that in each profile, $\psi_n = 0$ for all $F < F_c$, and that ψ_n is nearly constant for $F > F_c$. This is consistent with our proposition in Eq. (3.33). Denoting the mean value of $\psi_n(F; F_c)$ for $F > F_c$ by $\psi_0(F_c)$ (similar to Eq. (3.33)), we plot its trajectory as black dashed curves overlaying the radius-resolved saturation profiles in Figure 7-1 (similar to Figure 3-1). Evidently, the $\psi_0(F_c)$ trajectory is shaped differently in either case; notably, $\psi_0(F_c)$ approaches unity around $F_c = 1/2$ on two-dimensional square lattices (see Figure 7-1), rather than at $F_c = 0$ in our statistical theory based on pore branching (see Eq. (3.34) and Figure 3-1). These correspond to the critical occupation probabilities (percolation thresholds) for bond percolation on a 2-D square lattice and in 1-D, which are 1/2 and 1, respectively [45, 46].

Fourthly, we use Eq. (3.11) to compute s_n from $\psi_n(F)$ at each F_c, so as to obtain the $s_n(F_c)$ relationship for quasistatic primary drainage. This calculation is then repeated for various N ranging from 2 to 200, with selected results shown in the left panel of Figure 7-2. For small N, nearly all pore segments on the lattice are directly accessible by the invading fluid, and we have $s_n \approx 1 - F_c$, as the capillary bundle model would predict. As N becomes larger, $s_n(F_c)$ deviates further from the $s_n = 1 - F_c$ line, indicating a more prominent role of the ink-bottle effect. However, in all cases, s_n rapidly approaches $1 - F_c$ past the critical probability of 1/2, which is reminiscent of the observations in [145], and differs from those shown in Figure 3-4. Nevertheless, it is clear that when we increase N here, like when we decrease α in our statistical theory, the porous sample behave in a way that is more and more distinct from that of a capillary bundle, as a result of a greater degree of serial connections between different-size pores.

Lastly, we capitalize on these observations to arrive at estimates for the accessivities of porous samples represented by the various square lattices considered. On the one hand, according to our microscopic statistical theory, $1/\alpha$ can be interpreted geometrically as the mean number of different-size pores encountered per pore instance – see Section 2.2.3. Although this interpretation of accessivity, as we have discussed,

is only strictly valid when the pore space contains no loops, we may still consider it in the context of square lattices to obtain a "geometric estimate" for α. One can verify that a 2-D square lattice with side length $N = 2, 3, \ldots$, as depicted in Figure 7-1, has $2N(N-1)$ edges, and that of those edges, $4(2N-3)$ are connected to a vertex on the perimeter. If we claim that each edge that is accessible from the perimeter constitutes a pore instance for fluid displacement, and all the different-size edges are shared among these instances, we may write:

$$\frac{1}{\alpha_{\text{geom}}} = \frac{\text{total \# edges on lattice}}{\text{\# edges on perimeter}} = \frac{2N(N-1)}{4(2N-3)} \implies \alpha_{\text{geom}} = \frac{2(2N-3)}{N(N-1)}. \tag{7.1}$$

These geometric estimates, shown as the black curve in the right panel of Figure 7-2, are valid for all integers greater than or equal to 2. Note that $\alpha_{\text{geom}} = 1$ for both $N = 2$ and $N = 3$ because in either case all edges on the lattice are also directly accessible from its perimeter. On the other hand, from a macroscopic perspective, we expect α to be correlated with the area of a hysteresis loop in a drainage–imbibition cycle, which we shall denote by H. Based on our simple formulae for primary drainage and imbibition, Eqs. (3.28) and (3.41), the area between each pair of curves for a given α in Figure 3-4 is:

$$H = 1 - 2\int_0^1 \frac{\alpha(1-F_c)}{(1-\alpha)F_c + \alpha} \mathrm{d}F_c = 1 + \frac{2\alpha}{1-\alpha}\left(\frac{\ln\alpha}{1-\alpha} + 1\right), \tag{7.2}$$

which implies that the area of the hysteresis loop on a $s_n\,(F_c)$ graph (e.g., Figure 3-4) would vary from 0 to 1 as α changes from 1 to 0. In contrast, in the left panel in Figure 7-2, it appears that the area between the $s_n\,(F_c)$ curve and the $s_n = 1 - F_c$ line only increases up to $1/8$ as $N \to \infty$. The area of a full hysteresis loop, which we shall denote by H', would hence only increase up to $1/4$. If we consider $H' = 1/4$ and $H = 1$ analogous in the sense that they are both the maximum possible areas of a drainage–imbibition hysteresis loop in either scenario, it is plausible to estimate accessivity from invasion percolation data by substituting $H = 4H'$ into Eq. (7.2) and solving for α, which we shall we refer to as α_{marco} because it is based on measurements in terms of macroscopic quantities only. The results for various N are shown as red

circles in the right panel of Figure 7-2. Remarkably, α_{geom} and α_{marco} agree quite well with each other, even though they are both crude estimates based on our statistical theory involving pore morphologies that are notably simpler than those considered in these invasion percolation simulations. These results substantiate the view that accessivity as a continuum property of porous media does indeed have a physically intuitive pore-scale interpretation: because α measures the degree to which different-size pores are arranged in parallel or series, it must correlate with the area of hysteresis loops that arise due to connectivity effects, which holds true beyond the premise of our simple statistical theory based on pore branching, at least in a qualitative sense, even in pore networks that are plagued with loops.

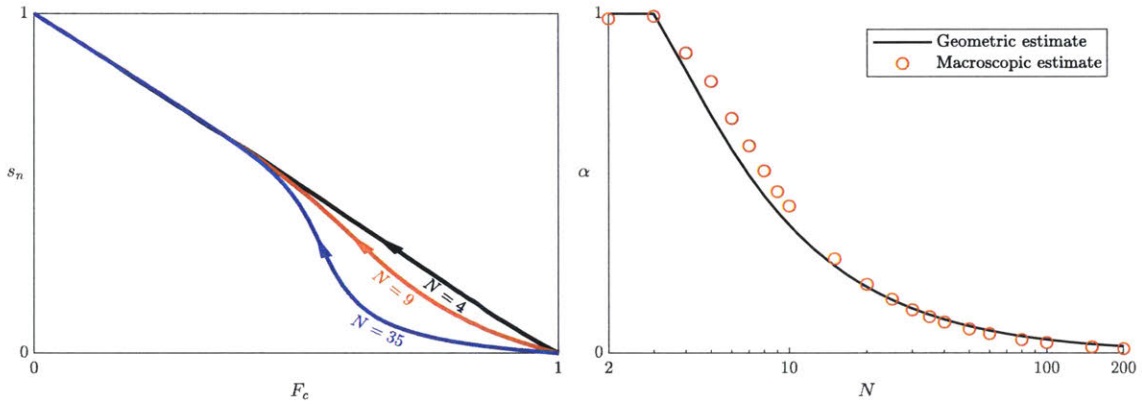

Figure 7-2: The left panel shows the $s_n\,(F_c)$ curves during primary drainage on 2-D square lattices of side lengths $N = 4$, $N = 9$, and $N = 35$, which deviates further from the $s_n = 1 - F_c$ (capillary bundle limit) as N grows larger. The right panel compares the geometric and macroscopic estimates of accessivities of lattices with various N (the horizontal axis uses a logarithmic scale), which are calculated from pore-scale data and continuum-scale measurements, respectively, and seem to agree well.

7.2 Skeletal representation of pore space

In this section, we will present elements of an image analysis routine that we have developed and implemented to convert a given pore-space morphology to its skeletal representation, which would then enable dynamical pore-network simulations on the extracted skeleton, to be discussed in Section 7.3. As we have noted in Sections 2.1

and 3.1.1, there has been a continued interest in the acquisition, analysis, and use of 2-D and 3-D image data of porous materials [190, 191, 192, 193, 194]. The grayscale data obtained from methods such as X-ray tomography[1] are first subject to **image segmentation** or **image thresholding** [195, 196, 197] in order to spatially resolve the phases present and to essentially arrive at functions like those defined in Eqs. (2.1) and (3.1). This information can be used to estimate certain statistical properties of the porous medium [198], or enable pore-network simulations [199, 200, 201, 202] or direct pore-scale simulations of multiphase flow [203, 74, 75]. Likewise, **micromodels**, which allow multiphase flow to be directly visualized in experiments [68, 204], also furnish pore images that can then be subject to various simulation methods [205, 206, 95, 207].

The need to extract a lower-dimensional skeletal representation[2] of the pore space arises from its use to construct pore-network models. A number of algorithms have been reported in the literature [208, 209, 210, 211, 212, 213, 214].

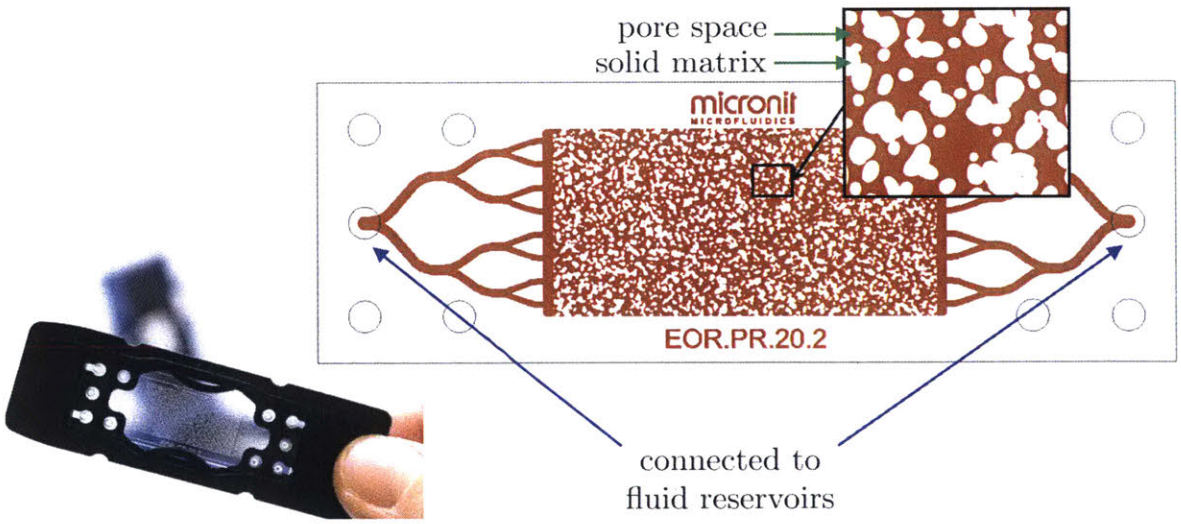

Figure 7-3: Photograph and pore-space morphology of the MICRONIT EOR.PR.20.2 microfluidic chip. Graphics supplied by the manufacturer[3].

We have developed and implemented a similar routine with concepts that are more

[1] aka. "data bricks" [190]

[2] other names of this representation or processes for obtaining such a similar representation include: ultimate dilation of grains, erosion, morphological thinning, skeletization, medial axis, line representation

[3] also see https://www.micronit.com/products/enhanced-oil-recovery.html

closely related to our probabilistic framework, which we will describe using the example of a pore image of a microfluidic chip. The chip is referred to as "EOR.PR.20.2", or the Enhanced Oil Recovery Chip with physical rock network, and is designed and manufactured by MICRONIT as a lab-on-a-chip device. A photograph of the chip and its 2-D pore image[4] are shown in Figure 7-3. The depth of the pore space in the direction perpendicular to the page as shown in Figure 7-3 is 20 μm, while the mean pore diameter in the plane of the page is in the 200–300 μm range. The height and width of the pore image[5] are 397 and 790 pixels, respectively, and each pixel corresponds definitively to either the solid matrix or the pore space[6], which in effect gives the discretized form of the function p_s for the medium as defined in Eq. (2.1), which we may represent with a binary data matrix $\mathbf{P} \in \{0,1\}^{397\times790}$.

The first step of our routine involves the labeling of connected components [215]. Here, each pixel in the solid matrix $P_{i,j} \in \{P_{i,j} \in \mathbf{P} : P_{i,j} = 1\}$ an index $c \in C \subset \mathbb{N}$ such that two pixels in the solid matrix share the same index if and only if they are connected via the solid phase, including in the diagonal direction[7]. The result of connected-component labeling is visualized in the upper left panel of Figure 7-4, where each distinct index is given a unique color[8]. Note that this method is only applicable to a 2-D pore image because the entire solid matrix is necessarily connected in 3D, causing every voxel in the solid matrix to be assigned the same index. Also notice that some connected components identified have highly nonconvex shapes, such as the largest several grains. This may create issues later on in the routine. Methods such as convex decomposition (exact [216] or approximate [217]) may resolve these issues, but were not implemented here.

The second step is referred to as pore-space coloring, and involves assigning each pixel in the pore space $P_{i,j} \in \{P_{i,j} \in \mathbf{P} : P_{i,j} = 0\}$ an index from the previously defined set of indices C for connected components. The index assigned to each pixel

[4]Available as the mask used to fabricate the chip

[5]considering only the central region of the chip that is meant to represent a porous medium, i.e., excluding the distributor channels on both sides of the chip

[6]i.e., no image segmentation is required

[7]That is, a pixel $P_{i,j}$ in the interior of a solid phase is considered connected to its nearest eight neighboring pixels, $\{P_{i\pm1,j\pm1}\}$, given that each is also in the solid phase.

[8]some colors may have been reused but not in a way that obscure this visualization

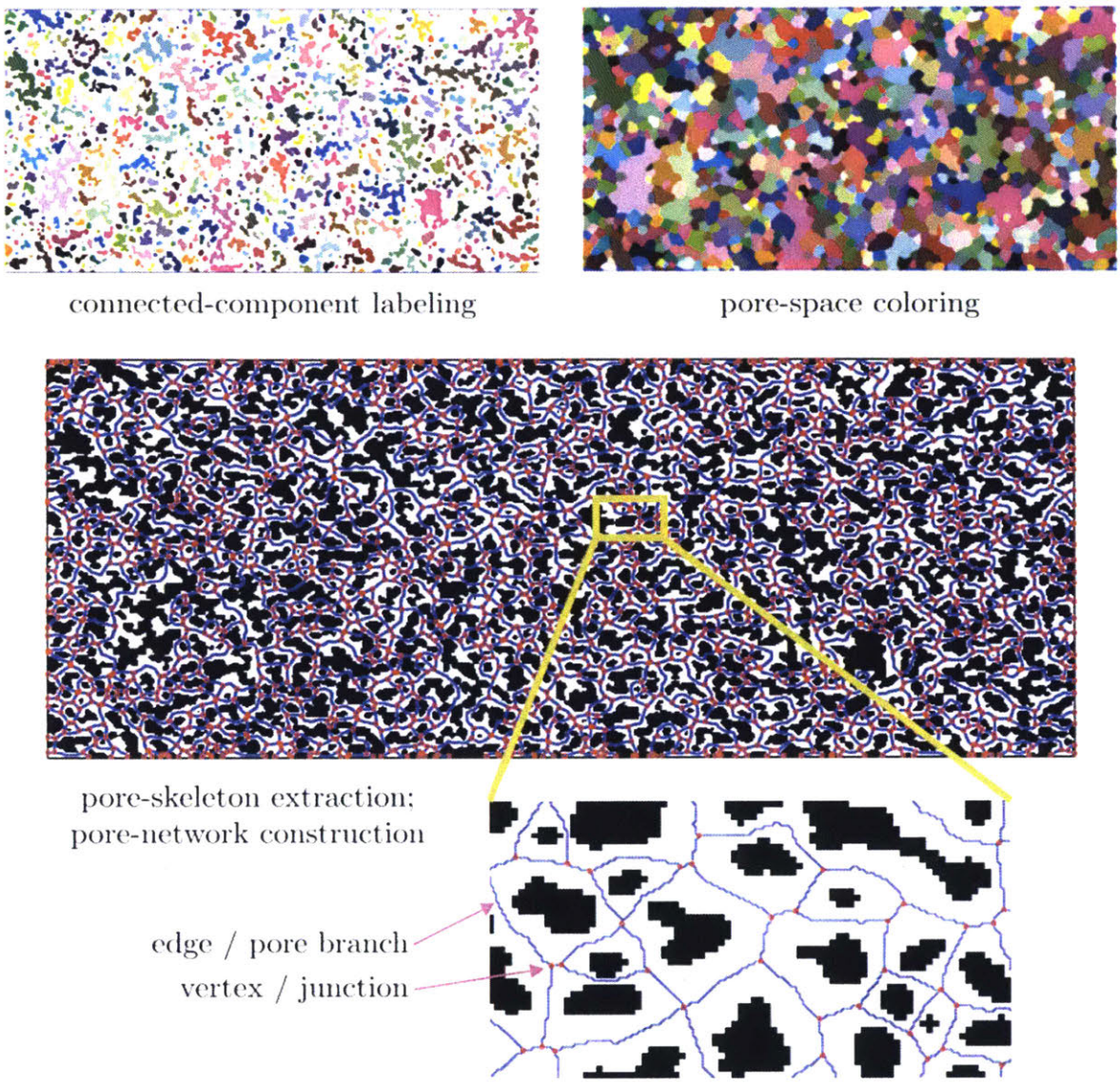

Figure 7-4: Schematic showing the steps in the routine that we apply to the pore image of EOR.PR.20.2.

in the pore space is equal to that of the closest solid pixel. In fact, to ensure that no pore pixel is equidistant from two solid pixels with different indices, we refine the resolution of the data matrix in this step to give $\hat{\mathbf{P}} \in \{0,1\}^{794\times1580}$ such that $P_{i,j} = \hat{P}_{2i-1,2j-1} = \hat{P}_{2i-1,2j} = \hat{P}_{2i,2j-1} = \hat{P}_{2i,2j}$ for all $i = 1,\ldots,397$ and $j = 1,\ldots,790$. This way, every pore pixel in $\hat{\mathbf{P}}$ is guaranteed to have exactly one closest solid pixel. Also, in searching for the closest solid pixel, we only need to consider the boundary pixels of all solid grains, which are defined as solid pixels that have at least one

adjacent pore pixel. The result of this step is visualized in the upper right panel of Figure 7-4. At this point, all pixels in the refined pore image are assigned an index in C; pixels share the same index if and only if they are connected. We note that if all solid grains are strictly convex, then the result of this step is equivalent to the Voronoi tessellation of the binary pore image [218, 219], as exemplified by the pore morphology considered in Section 7.3.

In the third step, we trace out the pore skeleton by highlighting all midpoints of unit line segments separating two pixels with distinct indices, i.e., points that belong to the borders of the color patches in the upper right panel of Figure 7-4. Each of these points are exactly equidistant to at least two distinct nearby solid grains, and can be assigned an effective pore radius that is equal to its distance to the nearest solid grains. Also, if we define a "Euclidean distance function" [220] from points in the pore space of the continuous domain of the porous medium to the distance to the nearest point in the solid matrix, then the points highlighted in this step are local maxima or saddle points of that distance function. The highlighted points are shown as blue points in the bottom panel of Figure 7-4.

The fourth step of the routine involves the identification of pore branches and junctions so as to construct an equivalent pore network that represents the morphology of the pore space. Junctions are taken as pixels on the skeleton that are equidistant to three or more solid grains[9], located at the boundary of the domain of the porous medium, or at the centroid of several nearby points with the above properties[10] (in which case such points are appended to the collection of points that trace out the skelton). Now that all points highlighted as part of the skeleton are either identified as a junction or not, we connect every point that is not a junction to its closest two other points on the skeleton with a line segment. This results in the full skeletal representation of the pore space. Additionally, the skeleton is unambiguously divided up into individual pore branches that are joined together at junctions like described in Section 2.2.1. We may also define an directed graph $G(V, E)$ where vertices

[9] i.e., points of triple contact or beyond in the upper right panel of Figure 7-4

[10] e.g., three triple contact points that are no more than one unit length away from one another

$v \in V = \{0, \ldots, |V| - 1\}$ represent all junctions, and edges $e \in E = \{0, \ldots, |E| - 1\}$ represent all pore branches. Each edge is mapped to a 2-tuple of vertices found at its two ends, $e \mapsto (v_{\mathrm{LO}}, v_{\mathrm{HI}})$, where v_{LO} and v_{HI} are the vertices of the lower and higher indices, respectively. It is permissible for different edges to map to the same 2-tuple of vertices. The topology of the pore space is hence embedded in G. In this example, G contains 692 edges and 522 vertices.

Finally, we parameterize each pore branch using some choice of pore axial coordinate, such as the arc length (see Section 2.2.1). We then measure the pore radius as a function of the pore axial coordinate, which we define as the distance to the nearest solid pixel[11]. We can then derive the PSD by computing the histogram of all radius data on a pore volume basis. Figure 7-5 shows the result, as well as a fitted log-normal distribution that seems to approximate the data well. The pore branches are assigned volumes that match those of the corresponding pores, while the junctions do not occupy any physical space.

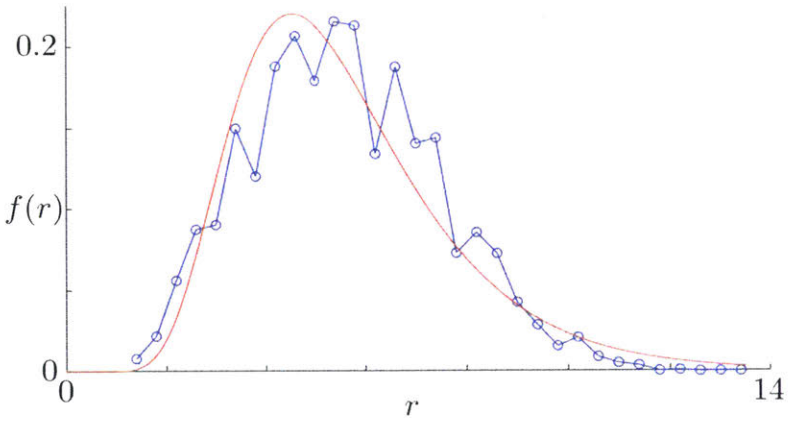

Figure 7-5: PDF of the PSD for EOR.PR.20.2, $f(r)$, determined from our image analysis routine. Radius data are reported in units of side length of a pixel. The raw distribution, shown in blue, has a mean of 5.57 and a standard deviation of 1.90, while the fitted log-normal distribution, shown in red, has a mean of 5.60 and a standard deviation of 2.15.

We posit that these analyses may be extended to accommodate other concepts

[11]Note that although this definition makes pore radii easy to compute, it is not consistent with our definition of effective pore radius discussed in Section 2.1.3. Ideally, we should consider the curvature of a static meniscus between two hypothetical immiscible fluid phases located at each axial location along the skeleton.

from our theory, such as the determination of the radius-resolved saturations in pore-scale simulations[12] and the estimation of pore-space accessivity by simulating quasistatic invasion percolation (as discussed in Section 7.1). It may be of interest to investigate these topics in future research.

7.3 Dynamical pore-network simulation

In this section, we present an illustrative example of performing dynamical pore-network simulations based on the skeletal representation of pore space derived using the methods detailed in Section 7.2. Here, we populate the pore skeleton with two immiscible fluid phases[13], such that along each edge, we may have alternating slugs of different fluids. Our goal is to simulate the dynamics of the redistribution of these fluids on the skeleton in response to pressures imposed on the domain boundary, given appropriate initial conditions.

Our overall solution scheme is as follows:

1. *Computation of conductances and Young-Laplace pressures*: at each instant, the fluid filling along an edge entails its hydraulic conductance, as well as the locations of any interfaces between different fluids, where pressure jumps occur according to the pore radii at those locations, as described by Eq. (2.10).

2. *Implicit vertex pressure update*: for pseudosteady flows, e.g., Stokes flow, we can use solve implicitly for the pressures at all vertices by enforcing material conservation at all vertices.

3. *Calculation of edge flow rates*: we then compute the instantaneous volumetric flow rates on all edges of the graph.

[12]The key challenge there is to unambiguously associate every pore pixel with a pore slice of a particular radius, which becomes exceedingly difficult as the shapes of pores deviate significantly from straight cylinders. More generally speaking, perhaps the concept of radius-resolved saturations should be extended to include different local patterns of fluid distribution, which could be assisted by studying any correlations in the p_w function defined in Eq. (3.1).

[13]It is much easier to simulate single-phase flow based on the skeletal representation, although the intrinsic permeabilities computed should be compared with direct pore-scale simulations or micromodel experiments.

4. *Explicit edge saturation update*: using the instantaneous flow rates found, we then advect the fluid filling profile along each edge in the direction of the flow explicitly in time.

This solution scheme, despite pertaining to pore-network modeling, is reminiscent of the IMPES scheme introduced in Chapter 6 for solving conventional continuum models of multiphase flow in porous media, underlining the analogies between pore-scale and continuum-scale quantities.

7.3.1 Data structure

Recall that the pore skeleton is expressed mathematically as the graph $G(V, E)$ defined in Section 7.2. At each time t, we attribute a pressure value to each vertex, p_v. In the case that a vertex resides on the domain boundary, we refer to it as an exterior vertex, and assign to it the prescribed boundary pressure at that location. On the other hand, each edge on the graph is associated with an instantaneous flow rate q_e, which takes a positive value if the flow occurs from the "LO-vertex" to the "HI-vertex" of that edge, and a negative value if the flow is in the opposite direction.

Forgoing potentially more elegant approaches, we record the fluid filling on the skeleton by adopting a finite-difference discretization of the edge axial coordinate. Each finite-difference node n is thereby assigned an effective pore radius r_n, and a saturation s_n of the nonwetting phase[14]. The nodes are placed evenly along each edge with respect to the pore axial coordinate[15], with the first and last nodes coinciding with the vertices at both ends of the edge. Nodes over the entire skeleton are assigned unique global indices $n \in N = \{0, \ldots, |N| - 1\}$ so that they grow both from the LO-vertex to the HI-vertex on each edge and in increasing edge indices on the entire graph.

[14]In this section only, the subscript n refers to the node index, not the nonwetting fluid. Where necessary, we will refer to the wetting and nonwetting phases using upright letters w and n.

[15]i.e., the volume of pore space between every two adjacent nodes is the same

7.3.2 Governing equations

The simulation begins at $t = 0$ subject to appropriately chosen initial conditions, and then marches forward in time in dynamically determined increments. To initialize the system, we specify the initial fluid filling by setting $s_n, n \in N$. The value of s_n at finite-difference nodes that coincide with exterior vertices are dictated by the type of fluid found in the reservoir connected to that vertex: unity if the reservoir fluid is nonwetting, and zero if it is wetting. We also prescribe the values of p_v at each exterior vertices, which shall remain unchanged throughout the simulation.

Following the sign convention set out earlier, the instantaneous volumetric flow rate on edge e is given by:

$$q_e = C_e \left(p_{v_{e,\mathrm{LO}}} - p_{v_{e,\mathrm{HI}}} + p_{\mathrm{cap},e} \right), \tag{7.3}$$

where C_e is the total hydraulic conductance of the edge, $p_{v_{e,\mathrm{LO}}}$ and $p_{v_{e,\mathrm{HI}}}$ are the pressures at the LO- and HI-vertices of the edge, and $p_{\mathrm{cap},e}$ is the net capillary pressure drop on the edge. Under the lubrication approximation, recalling our discussion about hydraulic conductances from Section 5.2.1, we find that:

$$C_e = \left[\frac{8}{\pi^2} \int_0^{x_{\max,e}} \frac{\mu(x)}{[r(x)]^6} \, \mathrm{d}x \right]^{-1} \approx \left[\frac{8 \Delta V_c}{\pi^2} \sum_{n=n_{e,\mathrm{LO}}}^{n_{e,\mathrm{HI}}-1} \frac{1}{2} \left(\frac{\mu_n}{{r_n}^6} + \frac{\mu_{n+1}}{{r_{n+1}}^6} \right) \right]^{-1}, \tag{7.4}$$

where x denotes the pore axial coordinate, along which the fluid viscosity μ and the effective pore radius r are allowed to vary, $x_{\max,e}$ is the total pore volume attributed to egde e, and ΔV_c is the volume of a computational cell. The viscosity μ_n at node n is evaluated using:

$$\mu_n = \begin{cases} \mu_{\mathrm{w}} & s_n \leq 0.5 \\ \mu_{\mathrm{n}} & s_n > 0.5, \end{cases} \tag{7.5}$$

where μ_{w} and μ_{n} denote the viscosities of the wetting and nonwetting phases, respectively.

The net capillary pressure drop on edge e is defined as:

$$p_{\text{cap},e} = \sum_{x \in X_{\text{cap},e}} \zeta(x) \left(\frac{2\gamma_{\text{wn}} \cos\theta_c}{r(x)} \right), \tag{7.6}$$

where $X_{\text{cap},e}$ denotes the set of all pore axial locations where there exists a meniscus between the two fluids[16], and $\zeta(x) = \text{sgn}(\text{d}(s)/\text{d}(x))$ across the interface[17]. Eq. (7.6) is discretized to:

$$p_{\text{cap},e} = 2\gamma_{\text{wn}} \cos\theta_c \sum_{n=n_{e,\text{LO}}}^{n_{e,\text{HI}}-1} \left[\zeta_n \left(r_n + (r_{n+1} - r_n) \left(\frac{0.5 - s_n}{s_{n+1} - s_n} \right) \right)^{-1} \right], \tag{7.7}$$

where:

$$\zeta_n = \begin{cases} +1 & s_n \leq 0.5 \text{ and } s_{n+1} > 0.5 \text{ (positive interface)} \\ -1 & s_n > 0.5 \text{ and } s_{n+1} \leq 0.5 \text{ (negative interface)} \\ 0 & \text{otherwise (interface absent).} \end{cases} \tag{7.8}$$

We define the following dimensionless variables:

$$\begin{gathered} \widetilde{r} \equiv \frac{r}{r_0}, \quad \widetilde{p} \equiv \frac{p}{2\gamma_{\text{wn}} \cos\theta_c / r_0}, \quad \widetilde{q} \equiv \frac{q}{\pi {r_0}^4 (p_{\max} - p_{\min}) / 8\mu_{\text{n}} L_M}, \\ \widetilde{C}_e \equiv \frac{C_e}{\pi {r_0}^4 / 8\mu_{\text{n}} L_M}, \quad \widetilde{V} \equiv \frac{V}{\pi {r_0}^2 L_M}, \quad \widetilde{t} \equiv \frac{t}{8\mu_{\text{n}} {L_M}^2 / (p_{\max} - p_{\min}) {r_0}^2}, \end{gathered} \tag{7.9}$$

and the following dimensionless parameters:

$$\widetilde{\mu}_{\text{w}} \equiv \frac{\mu_{\text{w}}}{\mu_{\text{n}}}, \quad \Delta\widetilde{p} \equiv \frac{p_{\max} - p_{\min}}{2\gamma_{\text{wn}} \cos\theta_c / r_0}, \quad \text{Ca} \equiv \frac{{r_0}^2 \Delta p}{8\gamma_{\text{wn}} L_M}, \tag{7.10}$$

where r_0 is any characteristic pore radius such as the mean or the minimum value, L_M is the macroscopic length scale for the size of the entire porous medium, $(p_{\max} - p_{\min})$ is the pressure drop imposed across the length of the porous medium, and Ca is the

[16] We say that an interface at location x is "positive" if $s(x^-) \leq 0.5$ and $s(x^+) > 0.5$, and "negative" if $s(x^-) > 0.5$ and $s(x^+) \leq 0.5$.

[17] That is, $\zeta(x) = +1$ if there is a positive interface at location x, and $\zeta(x) = -1$ if there is a negative interface.

capillary number[18], which is expected to be much less than unity because $r_0/L \ll 1$. Hence, Eqs. (7.3), (7.4), (7.5), and (7.7) become:

$$\widetilde{q}_e = \frac{\widetilde{C}_e}{\Delta\widetilde{p}}\left(\widetilde{p}_{v_{e,\mathrm{LO}}} - \widetilde{p}_{v_{e,\mathrm{HI}}} + \widetilde{p}_{\mathrm{cap},e}\right), \tag{7.11}$$

$$\widetilde{C}_e = \Delta\widetilde{V}_c\left[\sum_{n=n_{e,\mathrm{LO}}}^{n_{e,\mathrm{HI}}-1}\frac{1}{2}\left(\frac{\widetilde{\mu}_n}{(\widetilde{r}_n)^6} + \frac{\widetilde{\mu}_{n+1}}{(\widetilde{r}_{n+1})^6}\right)\right]^{-1}, \quad \widetilde{\mu}_n = \begin{cases}\widetilde{\mu}_{\mathrm{w}} & s_n \le 0.5,\\ 1 & s_n > 0.5\end{cases} \tag{7.12}$$

$$\widetilde{p}_{\mathrm{cap},e} = \sum_{n=n_{e,\mathrm{LO}}}^{n_{e,\mathrm{HI}}-1}\left[\zeta_n\left(\widetilde{r}_n + (\widetilde{r}_{n+1} - \widetilde{r}_n)\left(\frac{0.5 - s_n}{s_{n+1} - s_n}\right)\right)^{-1}\right]. \tag{7.13}$$

Material conservation at each interior vertex v writes:

$$\sum_{e\in\mathcal{E}_{v,\mathrm{HI}}}\widetilde{q}_e - \sum_{e\in\mathcal{E}_{v,\mathrm{LO}}}\widetilde{q}_e = 0, \tag{7.14}$$

where:

$$\mathcal{E}_{v,\mathrm{HI}} = \{e : \exists v', e \mapsto (v', v)\}, \quad \mathcal{E}_{v,\mathrm{LO}} = \{e : \exists v', e \mapsto (v, v')\}. \tag{7.15}$$

This linear system of equations is solved iteratively by the Gauss-Seidel method, where we make $\widetilde{p}_v$ the subject in each equation:

$$\widetilde{p}_v = \frac{\sum_{e\in\mathcal{E}_{v,\mathrm{HI}}}\left(\widetilde{C}_e\widetilde{p}_{v'} + \widetilde{p}_{\mathrm{cap},e}\right) + \sum_{e\in\mathcal{E}_{v,\mathrm{LO}}}\left(\widetilde{C}_e\widetilde{p}_{v'} - \widetilde{p}_{\mathrm{cap},e}\right)}{\sum_{e\in\mathcal{E}_{v,\mathrm{HI}}\cup\mathcal{E}_{v,\mathrm{LO}}}\widetilde{C}_e}. \tag{7.16}$$

The solutions $\widetilde{p}_v$ may be substituted back into Eq. (7.11) to compute all $\widetilde{q}_e$.

Now, given the instantaneous flow rates on edges, we update the fluid filling at all nodes over a small time increment to be determined. Essentially, we have to solve the 1-D transient advection equation on each edge:

$$\frac{\partial s}{\partial t} + q_e\frac{\partial s}{\partial x} = 0. \tag{7.17}$$

[18]For the same porous medium and fluid phases, the ratio of $\Delta\widetilde{p}$ to Ca is constant.

An important dimensionless group to consider is the Courant number, which is written for each edge as:

$$\mathrm{Co}_e^k = \frac{|q_e^k|\Delta t^k}{\Delta V_c}, \tag{7.18}$$

where k indexes the simulation time so that each time increment $\Delta t^k = t^{k+1} - t^k$. To ensure stable time marching, at time index k, we set the time increment dynamically by enforcing the Courant–Friedrichs–Lewy condition [221]:

$$\max_{e\in E}\{\mathrm{Co}_e^k\} = 0.1 \implies \Delta t^k = \frac{(0.1)\Delta V_c}{\max\limits_{e\in E}\{|q_e^k|\}} \implies \Delta \widetilde{t}^k = \frac{0.1}{\max\limits_{e\in E}\{|\widetilde{q}_e^k|\}}. \tag{7.19}$$

Eq. (7.17) is discretized using an explicit time-marching scheme with the first-order upwind approximation for the advective term to give:

$$s_n^{k+1} = \begin{cases} \left(1 - \mathrm{Co}_e^k\right) s_n^k + \mathrm{Co}_e^k s_{n-1}^k, & n = n_{e,\mathrm{LO}} + 1, \cdots, n_{e,\mathrm{HI}} \quad \widetilde{q}_e^k > 0 \\ \left(1 - \mathrm{Co}_e^k\right) s_n^k + \mathrm{Co}_e^k s_{n+1}^k, & n = n_{e,\mathrm{LO}}, \cdots, n_{e,\mathrm{HI}} - 1 \quad \widetilde{q}_e^k < 0, \end{cases} \tag{7.20}$$

The boundary condition on edge e is supplied at the entry node[19]. If the entry node coincides with an exterior vertex, then the saturation is set to represent the fluid type in the connected reservoir; otherwise, we set the saturation at the entry node to[20]:

$$s_{n_{\mathrm{entry}}}^{k+1} = \frac{\sum\limits_{\substack{e'\in\mathbb{E}_{v,\mathrm{HI}} \\ \widetilde{q}_{e'}^k>0}} \mathrm{Co}_{e'}^k s_{n_{e',\mathrm{HI}}}^k + \sum\limits_{\substack{e'\in\mathbb{E}_{v,\mathrm{LO}} \\ \widetilde{q}_{e'}^k<0}} \mathrm{Co}_{e'}^k s_{n_{e',\mathrm{LO}}}^k}{\sum\limits_{\substack{e'\in\mathbb{E}_{v,\mathrm{HI}} \\ \widetilde{q}_{e'}^k>0}} \mathrm{Co}_{e'}^k + \sum\limits_{\substack{e'\in\mathbb{E}_{v,\mathrm{LO}} \\ \widetilde{q}_{e'}^k<0}} \mathrm{Co}_{e'}^k}. \tag{7.21}$$

This completes the update of the fluid filling profile.

[19] i.e., $n_{e,\mathrm{LO}}$ if $\widetilde{q}_e^k > 0$ and $n_{e,\mathrm{HI}}$ if $\widetilde{q}_e^k < 0$

[20] this is equal to the mean of the saturations exiting edges that have flows towards the coinciding vertex, weighted by their respective Courant numbers

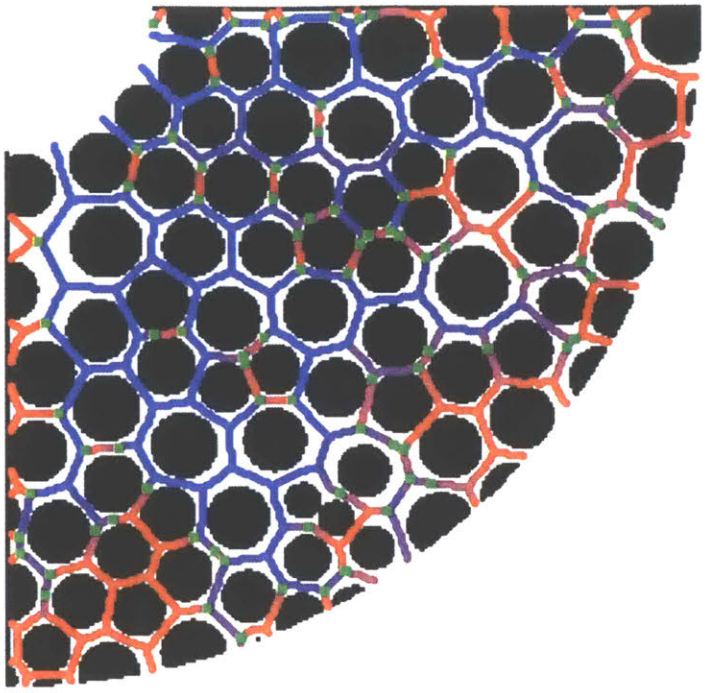

Figure 7-6: Fluid distribution on the skeletal representation of a micromodel after the first percolation event during primary drainage. Wetting and nonwetting phases are shown in red and blue, respectively. Interfaces between the two phases are represented with green squares.

7.3.3 Sample result

We carry out dynamical pore-network simulations on a skeleton extracted from the pore image of a micromodel similar to that used in [68]. The micromodel consists of circular posts of various sizes sandwiched in a Hele-Shaw cell. As shown in Figure 7-6, the pore space is initially saturated with the wetting phase, and we carry out primary drainage by exposing the the upper right corner of the device to a reservoir of the nonwetting phase at a higher pressure. We have $\widetilde{\mu}_{\mathrm{w}} = 0.8$ and $\Delta\widetilde{p} = 10$. The figure shows the fluid distribution on the skeleton after the first percolation event.

7.4 Kinetics of moisture transport in boehmite

In this section, we will briefly report our preliminary analysis of a set of experimental data[21] on the kinetics of water sorption and desorption in boehmite[22]. The uptake and release of moisture in building materials create the effect of **moisture buffering** [5] by reducing the fluctuation of humidity in the indoor humidity levels, which is analogous to the use of phase change materials to lessen air temperature swings [222]. It is thus of interest to measure and model the transport of moisture in building materials in order to design building materials for better moisture buffering characteristics. Models for moisture transport in porous media in the literature are based on a variety of pore-scale mechanisms [223, 224, 225, 56, 226, 58, 227, 59, 228]. Equilibrium water sorption and desorption measurements are often fitted to parametric sorption isotherms [229], while kinetics data of soprtion and desorption are often described by a simple exponential decay [230] or superimposed exponential decays [231, 232], which could be plausibly attributed to distinct physical origins, including any external mass-transfer resistance from the bulk air to the surface of the sample in poorly executed experiments.

7.4.1 Experimental setup

Figure 7-7 shows the experimental setup used to collect the sorption kinetics data. In each experiment, the sample[23] was placed in a shallow glass cup atop the scale located inside the climatic chamber. The sampler holder had a circular cross section with a diameter of 85 mm, as shown in Figure 7-8. To minimize any external mass-transfer resistance, a channel was designed to divert some of the inlet air to above the sample on purpose. The relative humidity and temperature of the incoming air were set by the user, with the latter kept constant at 20.0 °C throughout each experiment. The time evolution of the mass of the sample subjected to climate variations was

[21] supplied by coauthor Remi Goulet

[22] same material as that described in Section 4.2

[23] The boehmite powder was slightly compressed to prevent it from being blown away by the air draft.

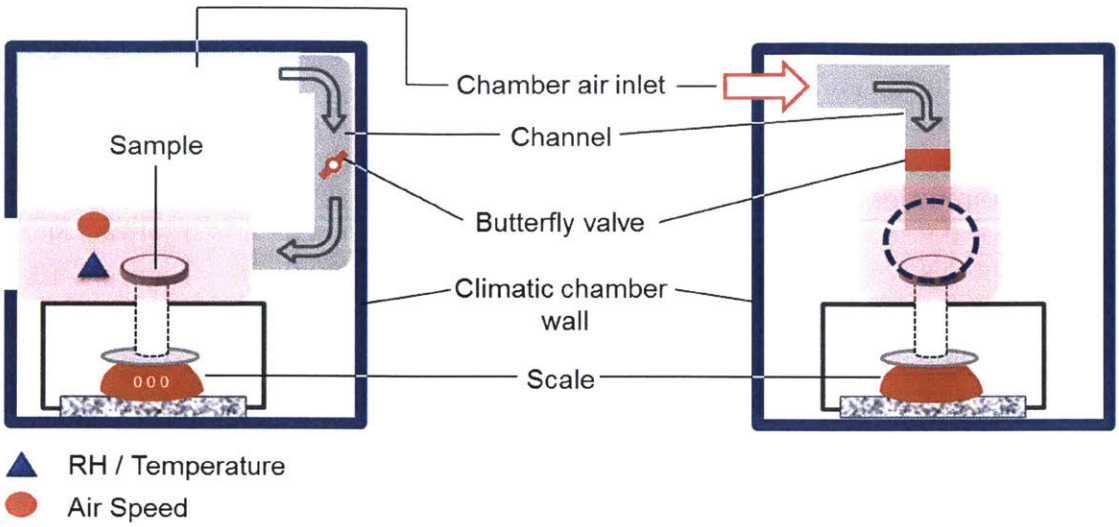

Figure 7-7: (Courtesy of coauthor Remi Goulet.) Schematic of the sorption kinetics bench used for measurements in this study. The left and right panels correspond to the front and side views, respectively.

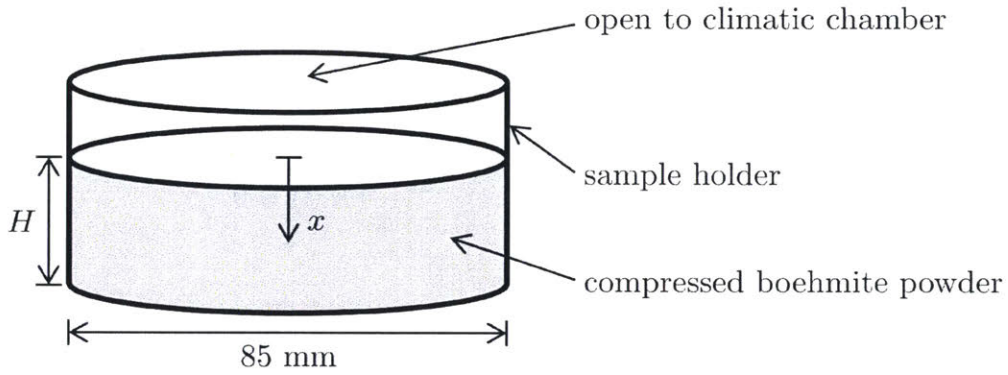

Figure 7-8: Geometry of the sample holder. We denote the vertical downward depth from the top surface of the sample with coordinate x.

measured, along with that of the relative humidity and of the air speed in the vicinity of the sample. The air speed was such that it would cause the sample to vibrate, leading to noisy mass measurements; hence, inlet air stream was periodically stopped so that mass measurements may be taken when the air around the sample was still. The uncertainties associated with measurements of the sample mass, the relative humidity, and the air velocity are ± 25 mg, ± 0.03, and ± 1.5 cm s^{-1}.

Four experimental trials were conducted, where samples of boehmite were subjected to step changes in the relative humidity of air. Table 7.1 summarizes the

Table 7.1: Summary of the water sorption kinetics data sets for boehmite.

#	Approximate range of relative humidities	Humidity steps during sorption	Humidity steps during desorption	Powder height, H (mm)	Plot
1	0.5–0.8	one	one	23.0	Figure 7-9
2	0.5–0.8	three	three	23.0	Figure 7-10
3	0.1–0.9	eight	eight	10.9	Figure 7-11
4	0.1–0.9	eight	eight	10.7	Figure 7-12

experimental conditions.

7.4.2 Theory

Based on the geometry of the sample depicted in Figure 7-8, we model moisture transport by considering the following 1-D nonlinear transient diffusion problem:

$$\text{PDE:} \quad \frac{\partial s}{\partial t} = \frac{\partial}{\partial x}\left(D_{\text{eff}}(s)\frac{\partial s}{\partial x}\right) \tag{7.22}$$

$$\text{BCs:} \quad s(0,t) = s_{\text{eq}}(h_\infty(t)), \quad \frac{\partial s}{\partial x}(H,t) = 0 \tag{7.23}$$

$$\text{IC:} \quad s(x,t_0) = s_{\text{eq}}(h_\infty(t_0)). \tag{7.24}$$

Here, the length coordinate $x \in [0, H]$ corresponds to the vertical downward distance from the top surface of the sample, as shown in Figure 7-8; H is the height of the sample, which is recorded in Table 7.1 for each experiment; s denotes the saturation of water in the porous medium; D_{eff} is the effective chemical diffusivity of water in the porous medium, which may depend on s and may be hysteretic; $h_\infty(t)$ is the imposed relative humidity in the climate chamber at time t, which we assume to be equal to the relative humidity at the top surface of the sample[24]; $s_{\text{eq}}(h_\infty)$ is the saturation in a porous medium in equilibrium with an air at relative humidity h, which are given by equilibrium sorption isotherms and may be hysteretic; and t_0 denotes any time at which we may assume the entire sample has achieved equilibrium with the humid air

[24]by assuming good mixing in the climatic chamber and hence negligible external mass-transfer resistance, given our experimental setup

in the climatic chamber, e.g., immediately before each humidity step is effected[25].

For small changes in s, we may linearize the model by assuming D_{eff} is constant. Suppose $h_\infty(t)$ undergoes a step change from $h_{\infty,-}$ to $h_{\infty,+}$ at $t = t_0$, we define the following dimensionless variables:

$$\Theta \equiv \frac{s - s_{\text{eq}}(h_{\infty,-})}{s_{\text{eq}}(h_{\infty,+}) - s_{\text{eq}}(h_{\infty,-})}, \quad \widetilde{x} \equiv \frac{x}{H}, \quad \widetilde{t} \equiv \frac{t - t_0}{H^2/D_{\text{eff}}}, \tag{7.25}$$

which leads to the linear dimensionless problem:

$$\text{PDE:} \quad \frac{\partial \Theta}{\partial \widetilde{t}} = \frac{\partial^2 \Theta}{\partial \widetilde{x}^2} \tag{7.26}$$

$$\text{BCs:} \quad \Theta(0, \widetilde{t}) = 1, \quad \frac{\partial \Theta}{\partial \widetilde{x}}(1, \widetilde{t}) = 0 \tag{7.27}$$

$$\text{IC:} \quad \Theta(\widetilde{x}, 0) = 0. \tag{7.28}$$

This linear problem can be solved analytically. The exact solution is:

$$\Theta(\widetilde{x}, \widetilde{t}) = \sum_{n=0}^{\infty} \frac{2}{\lambda_n} \sin(\lambda_n \widetilde{x}) e^{-{\lambda_n}^2 \widetilde{t}}, \quad \lambda_n = \left(n + \frac{1}{2}\right)\pi, \tag{7.29}$$

which gives the dimensionless total mass of water in the sample as:

$$\widetilde{m}(\widetilde{t}) = \int_0^1 \Theta(\widetilde{x}, \widetilde{t})\, \mathrm{d}\widetilde{x} = \sum_{n=0}^{\infty} \frac{2}{{\lambda_n}^2} e^{-{\lambda_n}^2 \widetilde{t}}, \quad \lambda_n = \left(n + \frac{1}{2}\right)\pi. \tag{7.30}$$

If we segment the time series of $m(t)$ for each experimental run and match them to the respective relative humidity steps, we can fit the response to the dimensional form of the analytical solution in Eq. (7.30):

$$m(t) = m_0 + \Delta m \sum_{n=0}^{\infty} \frac{2}{{\lambda_n}^2} \exp\left(\frac{-{\lambda_n}^2 \widetilde{t}}{H^2/D_{\text{eff}}}\right), \quad \lambda_n = \left(n + \frac{1}{2}\right)\pi, \tag{7.31}$$

where m_0 is the mass at the beginning of the segmented time series, and Δm and

[25] assuming that h_∞ has been kept constant for a sufficiently long time – e.g., a time that is much longer than the diffusion time of the sample – prior to t_0

D_{eff} are free parameters[26].

7.4.3 Results and preliminary analysis

We plot the time series of sample mass (relative to the reading of the scale immediately before the first humidity step is effected) and the imposed relative humidity in each experimental trial in Figures 7-9, 7-10, 7-11, and 7-12. We note that the sample mass occasionally changes nonmonotonically in response to a relative humidity step, which we attribute to experimental uncertainties.

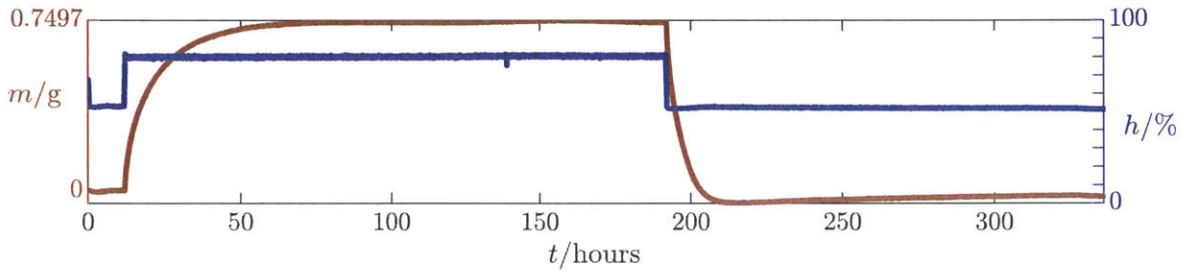

Figure 7-9: Time series of relative sample mass and relative humidity in the first water sorption kinetics experiment.

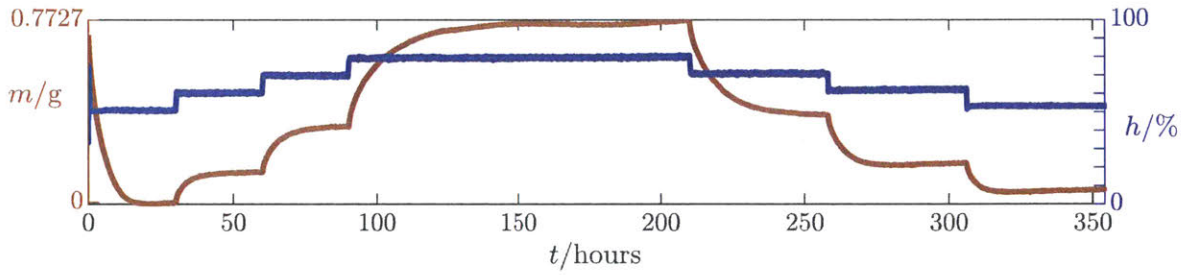

Figure 7-10: Time series of relative sample mass and relative humidity in the second water sorption kinetics experiment.

Estimates of D_{eff} of water in boehmite generated from all experimental data are shown in Figure 7-13. Each arrow corresponds to the D_{eff} obtained by fitting a segmented $m(h)$ response to a specific humidity step, which is implied by the horizontal span and direction of the arrow. The color of the arrow indicates the experimental

[26]Note that Δm should be approximately equal to the total change in sample mass in response to the humidity step, but is reserved as a fitting parameter considering the sample mass may not have fully equilibrated at the end of the segmented time series.

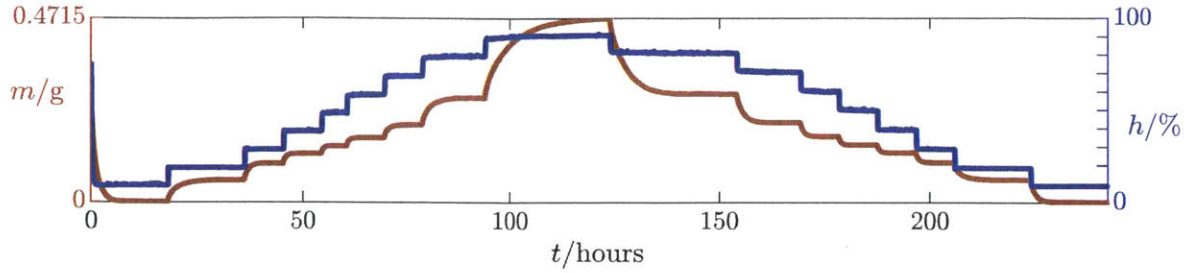

Figure 7-11: Time series of relative sample mass and relative humidity in the third water sorption kinetics experiment.

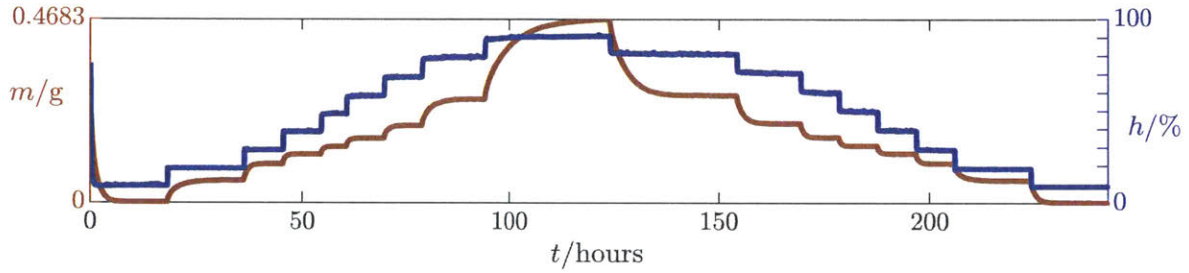

Figure 7-12: Time series of relative sample mass and relative humidity in the fourth water sorption kinetics experiment.

trial that it is associated with. Results across all data set are in good agreement, and remarkably, estimates obtained from the third and fourth trials are virtually identical, which may be due to the improved accuracy of measurements in these later experiments.

We observe that D_{eff} varies nonmonotonically with h. It peaks around $h = 40\%$ and becomes less for either lower or higher h. Overall, the values of D_{eff} span a little more than one order of magnitude. There is also mild hysteresis between the D_{eff} observed during sorption and desorption; desorption is generally associated with higher D_{eff} than sorption over the same range for the relative humidity, except for $20\% < h < 50\%$, where this trend is reversed. Given these observations, it is plausible that the mechanism for moisture transport in the pore space may undergo a transition near these values of h.

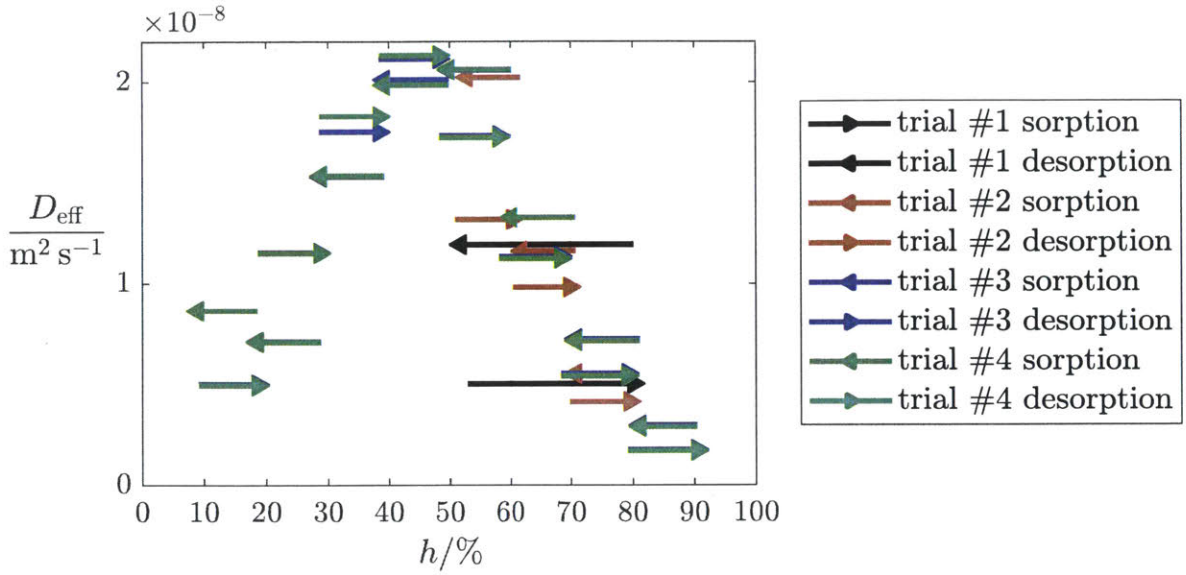

Figure 7-13: Estimated effective chemical diffusivities of water in boehmite as a function of equilibrium relative humidity. Results obtained from the four experimental trials are shown in black, red, blue, and green, respectively. Each arrow corresponds to the D_{eff} calculated for a specific humidity step, which is indicated by its horizontal span and direction. Note that many arrows for trials 3 and 4 coincide almost exactly.

7.4.4 Toward a microscopic theory

Moisture transport differs from immiscible multiphase flow in porous media. The latter involves only mechanical equilibrium at interfaces between fluids, while the former also involves chemical equilibrium because both the liquid and vapor phases consist of the chemical species water. As a result, it may be necessary to consider a different set of pore-scale physical processes in order to describe moisture transport at the continuum scale [233]. In doing that, it may also be able to incorporate elements of our probabilistic framework to capture the effects of pore-space morphological and fluid distribution. Here, we present a precursory microscopic theory of moisture transport in porous media based on free energy which makes a connection to the PSD.

Using the framework of nonequilibrium thermodynamics [234, 235], we postulate that the flux density of liquid water through the porous medium is driven by gradients

of its chemical potential, which gives[27]:

$$\frac{\partial s}{\partial t} = -\nabla \cdot \left(-\frac{D}{k_B T} s \nabla \mu_L \right), \tag{7.32}$$

where $(D/k_B T)$ is known as the mobility, D is the tracer diffusivity[28], and μ_L is the chemical potential of liquid water in the pore space. Neglecting the interaction between water vapor and the solid matrix, and denoting the equilibrium chemical potential of liquid water or water vapor in the bulk with μ^*, we formulate the chemical potential of the vapor phase as:

$$\mu_G = \mu^* + k_B T \ln h, \tag{7.33}$$

and that of the liquid phase as:

$$\mu_L = \mu^* - \frac{2\gamma \cos\theta V_m}{r}, \tag{7.34}$$

where k_B is the Boltzmann constant, h is the relative humidity in the vapor phase, γ is the surface tension between liquid water and humid air, θ is the contact angle as measured in the liquid phase, V_m is the molecular volume of water, and r is the radius of the pore hosting the liquid phase. Equating Eqs. (7.33) and (7.34) gives the Kelvin equation [37]:

$$\ln h_c = -\frac{2\gamma \cos\theta V_m}{r_c k_B T}, \tag{7.35}$$

which gives the equilibrium condition[29] between a vapor phase at relative humidity h_c and a liquid phase residing in a pore slice of radius r_c. Neglecting connectivity effects, which corresponds to $\alpha \to 1$ in our probabilistic framework, then all pores with radii smaller than r_c will become saturated with liquid water in a porous medium

[27]We assume that variations in s is driven by fluxes of liquid water only, which may not be accurate at lower relative humidities [228]. Also, hydraulic effects are also neglected in this analysis, i.e., no dynamic pressure gradients.

[28]which is assumed to be constant in this simple analysis

[29]analogous to Eq. (2.10) in multiphase flow and Eq. (4.1) in mercury porosimetry

in equilibrium with a humid air at relative humidity h_c, while all larger pores will host the vapor phase. Thus, the saturation of liquid water is given by[30]:

$$s = F_c \equiv F(r_c), \tag{7.36}$$

where F is the CDF of the PSD. Assuming that the liquid and vapor phases in the pore space are locally in equilibrium in any representative control volume of the porous medium, we take the gradient of Eq. (7.34):

$$\begin{aligned}\nabla\mu_L &= -\nabla\left(\frac{2\gamma\cos\theta V_m}{r_c}\right) \\ &= -2\gamma\cos\theta V_m\left[\frac{\mathrm{d}}{\mathrm{d}r_c}\left(\frac{1}{r_c}\right)\right]\left[\frac{\mathrm{d}F_c}{\mathrm{d}r_c}\right]^{-1}\nabla s \\ &= \frac{2\gamma\cos\theta V_m}{{r_c}^2 f_c}\nabla s,\end{aligned} \tag{7.37}$$

where $f_c \equiv f(r_c)$ and f denotes the PDF of the PSD. We insert Eq. (7.37) into Eq. (7.32) to obtain:

$$\frac{\partial s}{\partial t} = \nabla\cdot\left(\frac{D}{k_B T}\frac{2\gamma\cos\theta V_m}{{r_c}^2 f_c}s\nabla s\right). \tag{7.38}$$

Comparing with Eq. (7.22), we obtain:

$$\frac{D_{\text{eff}}}{D} = \frac{2\gamma\cos\theta V_m}{k_B T}\frac{s}{{r_c}^2 f_c} = -\frac{s}{r_c f_c}\ln h_c, \tag{7.39}$$

subject to Eqs. (7.35) and (7.36).

Thus, given the PSD or the equilibrium sorption isotherm, Eq. (7.39) enables the calculation of D_{eff} in the limit of $\alpha \to 1$. Some experimental sorption isotherms for boehmite[31] are shown in Figure 7-14. Because there is negligible hysteresis in the data, we use their average in Eq. (7.39) to derive the effective chemical diffusivity. The result is shown in Figure 7-15. We see that D_{eff} reaches its maximum value around $h = 40\%$ and becomes lower as h either increases or decreases. The values

[30] analogous to Eq. (3.4)

[31] supplied by coauthor Remi Goulet

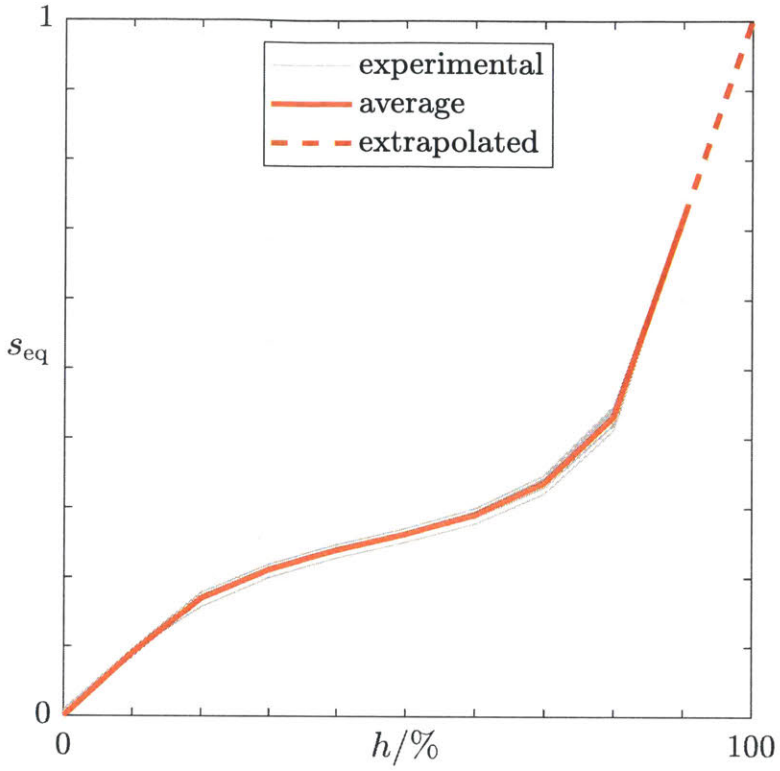

Figure 7-14: Experimental sorption and desorption isotherms at 20 °C (four sorption–desorption cycles) and their average for use in our calculation.

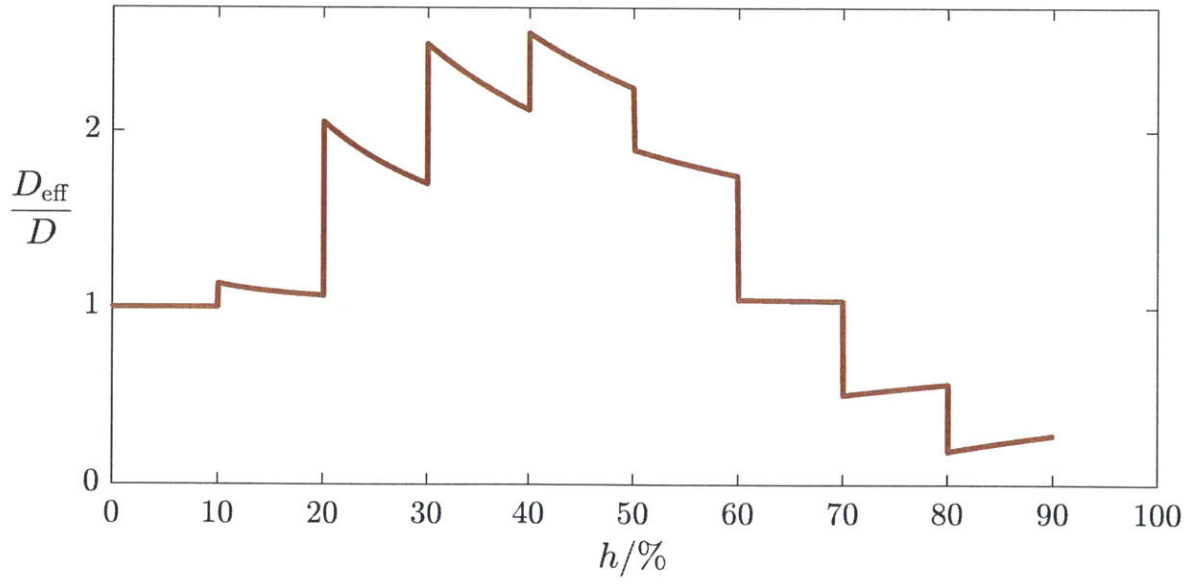

Figure 7-15: Ratio of effective chemical diffusivities to tracer diffusivity for water in boehmite as a function of equilibrium relative humidity predicted by Eq. (7.39). The qualitative behavior of D_{eff} resembles the results determined from the sorption kinetics data in Figure 7-13.

of D_{eff} in the range of relative humidities considered span approximately one order of magnitude. These features match the D_{eff} estimated from our sorption kinetics measurements shown in Figure 7-13. This preliminary result suggests that it may be possible to connect moisture transport at the continuum scale to the microstructure of porous media, which we characterize using the PSD in this simple analysis. It would be of interest to extend our theory by considering other concepts in our probabilistic framework, such as pore-space accessivity and radius-resolved saturations.

Chapter 8

Conclusion

In this thesis, we have proposed a number of novel concepts for modeling porous media at the continuum scale in the context of immiscible multiphase flow and other related physical processes. We have devised a probabilistic framework for connecting the relevant microscopic properties and states of porous media to macroscopic quantities of interest. Through experimental and computational studies, we have been able to partially validate our theory and demonstrate its utility in diverse applications. Our work has also revealed future research tasks that will help strengthen and broaden our theoretical framework.

Central to the thesis is our probabilistic framework presented in Chapter 2, which conceptualizes the pore space in a porous sample as an ensemble of pore-space instances, each formed by a number of independent homogeneous Poisson point processes corresponding to pore-scale events such as branching, pore-radius variation, and meniscus pinning. As a result, we have defined continuum properties and state variables for modeling porous media that have intuitive connections to pore-scale concepts.

One such property is the pore-space accessivity, α, defined in Section 2.2.3 to characterize the arrangement of different-radius pore slices that make up the pore space. Its two limiting values, $\alpha \to 0$ and $\alpha \to 1$, correspond to different-radius pores being arranged overwhelmingly in series and overwhelmingly in parallel, the latter echoing the widely used capillary bundle model. We have demonstrated in Chapter 4

that it is possible to measure the accessivity of a porous specimen by subjecting it to mercury cyclic porosimetry, a common characterization technique for porous materials.

In modeling capillary pressure and relative permeability hystereses in multiphase flow in porous media, presented in Chapters 3 and 5, we have also defined the radius-resolved saturations, $\psi_w(F)$ and $\psi_n(F)$, to describe the pore-scale distribution of fluid phases across different pore sizes. While $\psi_w(F)$ and $\psi_n(F)$ readily integrate to conventional saturations, they are distinguished in their inherent ability to predict hysteresis phenomena when used as state variables in continuum models. With the aid of our probabilistic framework, we have arrived at a series of relatively simple but physically meaningful formulae for hysteresis in capillary pressure (Eqs. (3.38) and (3.39)) and relative permeabilities (Eqs. (5.11), (5.12), (5.31), and (5.32)). The formulae have been successfully implemented as hysteresis-enabling constitutive relationships in continuum simulations of multiphase flow in Chapter 6. We have also discussed other topics of relevance to this thesis in Chapter 7.

In conclusion, we have demonstrated that it is possible to describe hysteresis in multiphase flow in porous media with simple, physics-based continuum modeling concepts. It is our hope that these concepts will augment current methods of portraying hysteresis in multiphase flow, as well as gain broader utility in the theoretical, computational, and experimental research of other physical phenomena in porous media.

Appendix A

Useful properties of homogeneous Poisson point processes

A.1 Preliminaries

Consider a **homogeneous Poisson point process** defined on a real line, whose coordinate we refer to as a "distance". Suppose the process is associated with a rate parameter of λ, which has units of inverse distance, such that the expected number of events occurring over an interval of distance x is equal to λx; in fact, the number of events occurring over a randomly chosen interval of distance x follows a **Poisson distribution**. On the other hand, the distance between two adjacent events, which we denote by the random variable X, follows an **exponential distribution** whose probability density function (PDF) is given by:

$$p(x) = \lambda e^{-\lambda x} \tag{A.1}$$

and whose cumulative distribution function (CDF) is given by:

$$P(x) = 1 - e^{-\lambda x}. \tag{A.2}$$

It is easy to verify that the expected value of the distribution, $\langle x \rangle$, equals λ^{-1}.

A.2 Simultaneous independent processes

Now, consider a collection of simultaneous independent homogeneous Poisson point processes indexed by $i = 1, \ldots, N$, each associated with its respective rate parameters λ_i. While we have stated that distance between two adjacent events from the same Poisson process follows an exponential distribution, the same is also true for the distance between two adjacent events from any of the N independent Poisson processes, whose CDF is given by:

$$\begin{aligned} P_{\text{tot}}(x) &= 1 - \prod_{i=1}^{N} (1 - P_i(x)) \\ &= 1 - \prod_{i=1}^{N} e^{-\lambda_i x} \\ &= 1 - e^{-\lambda_{\text{tot}} x}, \quad \lambda_{\text{tot}} = \sum_{i=1}^{N} \lambda_i, \end{aligned} \tag{A.3}$$

where P_i denotes the exponential CDF associated with event i. Thus, the expected distance between two adjacent events from any of the N independent Poisson processes is equal to ${\lambda_{\text{tot}}}^{-1}$.

As we traverse the real line in either direction from an arbitrary starting point, the probability that the first event encountered is from process i is given by:

$$\begin{aligned} \int_0^\infty p_i(x) \prod_{\substack{j=1 \\ j \neq i}}^{N} (1 - P_j(x)) \, \mathrm{d}x &= \int_0^\infty \lambda_i e^{-\lambda_i x} \prod_{\substack{j=1 \\ j \neq i}}^{N} e^{-\lambda_j x} \, \mathrm{d}x \\ &= \lambda_i \int_0^\infty \prod_{j=1}^{N} e^{-\lambda_j x} \, \mathrm{d}x \\ &= \lambda_i \int_0^\infty e^{-\lambda_{\text{tot}} x} \, \mathrm{d}x \\ &= \lambda_i \left. \frac{e^{-\lambda_{\text{tot}} x}}{-\lambda_{\text{tot}}} \right|_0^\infty \\ &= \frac{\lambda_i}{\lambda_{\text{tot}}}. \end{aligned} \tag{A.4}$$

We may generalize this result by stating that the probability that the first event

encountered is from one of the processes in the set $A \subset \{1, \ldots, N\}$ is given by $\sum_{i \in A} \lambda_i / \lambda_{\text{tot}}$, since the occurrence of events associated with all the processes in A is itself a homogeneous Poisson point process, as we have shown above.

A.3 Branching process

Suppose that the simultaneous independent homogeneous Poisson point processes refer to a branching process. Specifically, let λ_z be the rate parameter for the event of encountering a z-coordinate junction, $z = 1, 3, 4, \ldots$, as we traverse the real line. After encountering z-coordinate junction, the real line will split into $z - 1$ independent real lines[1], on which the simultaneous independent homogeneous Poisson point processes continue occurring in an independent fashion. Also define $\lambda_{\mathbb{Z}^+} = \sum_{z \in \mathbb{Z}^+} \lambda_z$ (for simplicity of notation, where we set $\lambda_2 = 0$), which is the rate parameter for the event of encountering a junction of any coordination number.

Suppose that there is a numerical property, $u \in \mathbb{R}$ associated with the line segment between the starting point on the real line and the location of the first junction of any coordination number. Let this numerical property be represented by the random variable U. Further suppose that each junction represents the algebraic operation of summation, such that we may calculate a total for this numerical property that is associated with all descendant line segments on this side of the starting point, which we denote by $v \in \mathbb{R}$ and represent by the random variable V. Because the $z - 1$ descendant real lines emanating from a z-coordinate junction are independent and homogeneous Poisson point processes are "memoryless", the total numerical property for each descendant real line and that of the parent real line are independent and identically distributed (i.i.d.). This allows us to construct the following equation in terms of random variables:

$$V_0 = U + \sum_{z \in \mathbb{Z}^+} \frac{\lambda_z}{\lambda_{\mathbb{Z}^+}} \sum_{j=1}^{z-1} V_j, \tag{A.5}$$

[1]For $z = 1$, the real line simply terminates and hence all Poisson processes cease immediately.

where all V_j are i.i.d. as V. Note that the equation is linear with respect to all random variables. Thus, we take the expected value of both sides of the equation to obtain:

$$\begin{aligned}
\langle v_0 \rangle &= \langle u \rangle + \sum_{z \in \mathbb{Z}^+} \frac{\lambda_z}{\lambda_{\mathbb{Z}^+}} \sum_{j=1}^{z-1} \langle v_j \rangle \\
\langle v \rangle &= \langle u \rangle + \sum_{z \in \mathbb{Z}^+} \frac{\lambda_z}{\lambda_{\mathbb{Z}^+}} (z-1) \langle v \rangle \\
\left[1 - \sum_{z \in \mathbb{Z}^+} \frac{\lambda_z}{\lambda_{\mathbb{Z}^+}} (z-1) \right] \langle v \rangle &= \langle u \rangle \\
\left[\sum_{z \in \mathbb{Z}^+} \frac{\lambda_z}{\lambda_{\mathbb{Z}^+}} - \sum_{z \in \mathbb{Z}^+} \frac{\lambda_z}{\lambda_{\mathbb{Z}^+}} (z-1) \right] \langle v \rangle &= \langle u \rangle \\
\langle v \rangle &= \frac{\lambda_{\mathbb{Z}^+}}{\sum_{z \in \mathbb{Z}^+} (2-z) \lambda_z} \langle u \rangle ,
\end{aligned} \tag{A.6}$$

where the ratio of $\langle v \rangle$ to $\langle u \rangle$ is positive if and only if:

$$\sum_{z \in \mathbb{Z}^+} (2-z) \lambda_z > 0, \tag{A.7}$$

which further constrains the permissible values of $\{\lambda_z / \lambda_{\mathbb{Z}^+} \in [0,1] : z \in \mathbb{Z}^+\}$. For instance, consider:

$$\begin{aligned}
(2-1) \frac{\lambda_1}{\lambda_{\mathbb{Z}^+}} + \sum_{z=3}^{\infty} (2-z) \frac{\lambda_z}{\lambda_{\mathbb{Z}^+}} &> 0 \\
\frac{\lambda_1}{\lambda_{\mathbb{Z}^+}} &> \sum_{z=3}^{\infty} (z-2) \frac{\lambda_z}{\lambda_{\mathbb{Z}^+}} \\
\frac{\lambda_1}{\lambda_{\mathbb{Z}^+}} &> \sum_{z=3}^{\infty} (3-2) \frac{\lambda_z}{\lambda_{\mathbb{Z}^+}} \\
\frac{\lambda_1}{\lambda_{\mathbb{Z}^+}} &> 1 - \frac{\lambda_1}{\lambda_{\mathbb{Z}^+}} \\
\frac{\lambda_1}{\lambda_{\mathbb{Z}^+}} &> \frac{1}{2},
\end{aligned} \tag{A.8}$$

so $\lambda_1 / \lambda_{\mathbb{Z}^+} \in (1/2, 1]$. We can similarly derive bounds for other rate parameters. Note that as long as Eq. (A.7) holds, we always have $\langle v \rangle \geq \langle u \rangle$, which readily follows from

Eq. (A.6) by noting the definition of $\lambda_{\mathbb{Z}^+}$.

To illustrate, we will use the result in Eq. (A.6) to compute the expected total distance of all line segments on one side of an arbitrary starting point on the parent real line. Because the line segment between the starting point and the first junction of any coordination number has an expected distance of $\langle u \rangle = {\lambda_{\mathbb{Z}^+}}^{-1}$, the expected value of the total distance is given by:

$$\langle v \rangle = \frac{\lambda_{\mathbb{Z}^+}}{\sum_{z \in \mathbb{Z}^+} (2-z)\lambda_z} \frac{1}{\lambda_{\mathbb{Z}^+}} = \frac{1}{\sum_{z \in \mathbb{Z}^+} (2-z)\lambda_z}. \tag{A.9}$$

We can also derive results similar to Eq. (A.6) for other algebraic operations at junctions, as long as the governing equation is linear with respect to all random variables.

Bibliography

[1] Z. Gu and M. Z. Bazant. Microscopic theory of capillary pressure hysteresis based on pore-space accessivity and radius-resolved saturation. *Chem. Eng. Sci.*, 196:225–246, 2019.

[2] J. Bear. *Dynamics of fluids in porous media.* New York : American Elsevier, 1972.

[3] B. O. Brattebo and D. B. Booth. Long-term stormwater quantity and quality performance of permeable pavement systems. *Water Res.*, 37(18):4369–4376, November 2003.

[4] T. H. Ahmed. *Reservoir engineering handbook.* Boston : Gulf Professional Pub., 4th edition, 2010.

[5] S. Hameury. Moisture buffering capacity of heavy timber structures directly exposed to an indoor climate: a numerical study. *Build. Environ.*, 40(10):1400–1412, October 2005.

[6] H. S. Fogler. *Essentials of Chemical Reaction Engineering.* Pearson Education, 2011.

[7] S. Torquato. *Random heterogeneous materials: microstructure and macroscopic properties*, volume 16. Springer Science & Business Media, 2013.

[8] H. P. G. Darcy. *Les fontaines publiques de la ville de Dijon: Exposition et application des principes à suivre et des formules à employer dans les questions de distribution d'eau.* Victor Dalmont, 1856.

[9] P. Forchheimer. Wasserbewegung durch Boden. *Z. Ver. Dtsch. Ing.*, 45(50):1782–1788, 1901.

[10] L. J. Klinkenberg. The permeability of porous media to liquids and gases. In *Drilling and production practice.* American Petroleum Institute, 1941.

[11] D. Lasseux and F. J. Valdés-Parada. On the developments of Darcy's law to include inertial and slip effects. *CR Mécanique*, 345(9):660–669, 2017.

[12] H. C. Brinkman. A calculation of the viscous force exerted by a flowing fluid on a dense swarm of particles. *Flow Turbul. Combust.*, 1(1):27, 1949.

[13] M. Muskat and M. W. Meres. The flow of heterogeneous fluids through porous media. *Physics*, 7(9):346–363, 1936.

[14] M. Muskat, R. D. Wyckoff, H. G. Botset, and M. W. Meres. Flow of gas-liquid mixtures through sands. *T. AIME*, 123(01):69–96, 1937.

[15] G. F. Pinder and W. G. Gray. *Essentials of Multiphase Flow in Porous Media.* John Wiley & Sons, 2008.

[16] H. I. Essaid, W. N. Herkelrath, and K. M. Hess. Simulation of fluid distributions observed at a crude oil spill site incorporating hysteresis, oil entrapment, and spatial variability of hydraulic properties. *Water Resour. Res.*, 29(6):1753–1770, 1993.

[17] R. Juanes, E. J. Spiteri, F. M. Orr, and M. J. Blunt. Impact of relative permeability hysteresis on geological CO2 storage. *Water Resour. Res.*, 42(12), 2006.

[18] C. Doughty. Modeling geologic storage of carbon dioxide: Comparison of non-hysteretic and hysteretic characteristic curves. *Energ. Convers. Manage.*, 48(6):1768–1781, June 2007.

[19] M. Sahimi. *Flow and Transport in Porous Media and Fractured Rock: From Classical Methods to Modern Approaches.* John Wiley & Sons, 2011.

[20] C. F. Gauss. Besprechung des Buchs von LA Seeber: Untersuchnugen iiber die Eigenschaften der positiven ternaren quadratischen Formen usw. *Gottingsche Gelehrte Anzeigen*, 1831.

[21] L. C. Graton and H. J. Fraser. Systematic packing of spheres: with particular relation to porosity and permeability. *J. Geol.*, 43(8, Part 1):785–909, 1935.

[22] O. Wiener. Die theorie des mischkorpers fur das feld der statonaren stromung. i. die mittelwertsatze fur kraft, polarisation and energie, der abhandlungen der mathematisch-physischen klasse der konigl. *Sachsischen Gesellshaft der Wissenschaften*, 32:509–604, 1912.

[23] Z. Hashin and S. Shtrikman. A variational approach to the theory of the effective magnetic permeability of multiphase materials. *J. Appl. Phys.*, 33(10):3125–3131, 1962.

[24] N. Epstein. On tortuosity and the tortuosity factor in flow and diffusion through porous media. *Chem. Eng. Sci.*, 44(3):777–779, 1989.

[25] S. J. Cooper, A. Bertei, P. R. Shearing, J. A. Kilner, and N. P. Brandon. TauFactor: An open-source application for calculating tortuosity factors from tomographic data. *SoftwareX*, 5:203–210, 2016.

[26] E. Krüger. Die Grundwasserbewegung. *Internationale Mitteilungen für Bodenkunde*, 8:105, 1918.

[27] J. Kozeny. *Über kapillare leitung des wassers im boden:(aufstieg, versickerung und anwendung auf die bewässerung)*. Hölder-Pichler-Tempsky, 1927.

[28] P. C. Carman. Fluid flow through granular beds. *T. Inst. Chem. Eng.*, 15:150–166, 1937.

[29] P. C. Carman. *Flow of gases through porous media*. Academic Press, New York, 1956.

[30] A. E. Scheidegger. Theoretical models of porous matter. *Produc. Mon.*, 17(10):17–23, 1953.

[31] W. M. Deen. *Analysis of transport phenomena*. Oxford University Press, New York, 2nd edition, 2012.

[32] E. W. Washburn. Note on a method of determining the distribution of pore sizes in a porous material. *P. Natl. A. Sci. USA*, pages 115–116, 1921.

[33] H. L. Ritter and L. C. Drake. Pore-size distribution in porous materials: pressure porosimeter and determination of complete macropore-size distributions. *Ind. En. Chem. Anal. Ed.*, 17(12):782–786, 1945.

[34] W. R. Purcell. Capillary pressures-their measurement using mercury and the calculation of permeability therefrom. *J. Petrol. Technol.*, 1(02):39–48, 1949.

[35] N. M. Winslow and J. J. Shapiro. An instrument for the measurement of pore-size distribution by mercury penetration. *ASTM Bull.*, 236:39–54, 1959.

[36] L. K. Frevel and L. J. Kressley. Modifications in mercury porosimetry. *Anal. Chem.*, 35(10):1492–1502, 1963.

[37] W. Thomson. 4. On the equilibrium of vapour at a curved surface of liquid. *P. Roy. Soc. Edin.*, 7:63–68, 1872.

[38] E. P. Barrett, L. G. Joyner, and P. P. Halenda. The determination of pore volume and area distributions in porous substances. I. Computations from nitrogen isotherms. *J. Am. Chem. Soc.*, 73(1):373–380, 1951.

[39] R. W. Cranston and F. A. Inkley. 17 The Determination of Pore Structures from Nitrogen Adsorption Isotherms. In *Advances in catalysis*, volume 9 of *Proceedings of the International Congress on Catalysis*, pages 143–154. Academic Press, January 1957.

[40] M. J. Blunt. Flow in porous media - pore-network models and multiphase flow. *Curr. Opin. Colloid In.*, 6(3):197–207, 2001.

[41] A. S. Al-Kharusi and M. J. Blunt. Network extraction from sandstone and carbonate pore space images. *J. Petrol. Sci. Eng.*, 56(4):219–231, 2007.

[42] D. B. Silin, G. Jin, and T. W. Patzek. Robust determination of the pore space morphology in sedimentary rocks. In *SPE Annual Technical Conference and Exhibition*. Society of Petroleum Engineers, 2003.

[43] D. Silin and T. Patzek. Pore space morphology analysis using maximal inscribed spheres. *Physica A*, 371(2):336–360, 2006.

[44] S. Lowell, J. E. Shields, M. A. Thomas, and M. Thommes. *Characterization of Porous Solids and Powders: Surface Area, Pore Size and Density*. Springer Science & Business Media, 2012.

[45] M. Sahimi. *Applications of percolation theory*. CRC Press, 1994.

[46] D. Stauffer and A. Aharony. *Introduction to percolation theory*. CRC press, revised second edition edition, 2014.

[47] G. Allaire. Homogenization of the Stokes flow in a connected porous medium. *Asymptotic Anal.*, 2(3):203–222, 1989.

[48] U. Hornung. *Homogenization and porous media*, volume 6. Springer Science & Business Media, 2012.

[49] A. L. Loeb. Thermal conductivity: VIII, a theory of thermal conductivity of porous materials. *J. Am. Ceram. Soc.*, 37(2):96–99, 1954.

[50] J. K. Carson, S. J. Lovatt, D. J. Tanner, and A. C. Cleland. Thermal conductivity bounds for isotropic, porous materials. *Int. J. Heat Mass Tran.*, 48(11):2150–2158, 2005.

[51] A. E. Scheidegger. *The physics of flow through porous media*. University of Toronto Press: Toronto, third edition edition, 1974.

[52] L. A. Richards. Capillary conduction of liquids through porous mediums. *J. Appl. Phys.*, 1(5):318–333, 1931.

[53] S. E. Buckley and M. C. Leverett. Mechanism of fluid displacement in sands. *T. AIME*, 146(01):107–116, 1942.

[54] E. C. Childs and N. Collis-George. The permeability of porous materials. In *P. Roy. Soc. Lond. A Mat.*, volume 201, pages 392–405. The Royal Society, 1950.

[55] A. Klute. Some Theoretical Aspects of the Flow of Water in Unsaturated Soils 1. *Soil Sci. Soc. Am. J.*, 16(2):144–148, 1952.

[56] H. Tamon, M. Okazaki, and R. Toei. Flow mechanism of adsorbate through porous media in presence of capillary condensation. *AIChE J.*, 27(2):271–277, 1981.

[57] K.-H. Lee and S.-T. Hwang. The transport of condensible vapors through a microporous Vycor glass membrane. *J. Colloid Interf. Sci.*, 110(2):544–555, 1986.

[58] D. N. Jaguste and S. K. Bhatia. Combined surface and viscous flow of condensable vapor in porous media. *Chem. Eng. Sci.*, 50(2):167–182, 1995.

[59] H. D. Do and D. D. Do. A new diffusion and flow theory for activated carbon from low pressure to capillary condensation range. *Chem. Eng. J.*, 84(3):295–308, 2001.

[60] L. J. Durlofsky. Coarse scale models of two phase flow in heterogeneous reservoirs: volume averaged equations and their relationship to existing upscaling techniques. *Computat. Geosci.*, 2(2):73–92, 1998.

[61] T. Arbogast. Numerical subgrid upscaling of two-phase flow in porous media. In *Numerical treatment of multiphase flows in porous media*, pages 35–49. Springer, 2000.

[62] J. H. Cushman, L. S. Bennethum, and B. X. Hu. A primer on upscaling tools for porous media. *Adv. Water Resour.*, 25(8-12):1043–1067, 2002.

[63] B. D. Wood. The role of scaling laws in upscaling. *Adv. Water Resour.*, 32(5):723–736, 2009.

[64] L. Li, C. A. Peters, and M. A. Celia. Upscaling geochemical reaction rates using pore-scale network modeling. *Adv. Water Resour.*, 29(9):1351–1370, 2006.

[65] R. Lenormand, C. Zarcone, and A. Sarr. Mechanisms of the displacement of one fluid by another in a network of capillary ducts. *J. Fluid Mech.*, 135:337–353, 1983.

[66] T. Pak, I. B. Butler, S. Geiger, M. I. J. van Dijke, and K. S. Sorbie. Droplet fragmentation: 3d imaging of a previously unidentified pore-scale process during multiphase flow in porous media. *P. Natl. A. Sci.*, 112(7):1947–1952, 2015.

[67] R. Holtzman and E. Segre. Wettability stabilizes fluid invasion into porous media via nonlocal, cooperative pore filling. *Phys. Rev. Lett.*, 115(16):164501, 2015.

[68] B. Zhao, C. W. MacMinn, and R. Juanes. Wettability control on multiphase flow in patterned microfluidics. *P. Natl. A. Sci.*, 113(37):10251–10256, 2016.

[69] P. M. Adler and H. Brenner. Multiphase flow in porous media. *Annu. Rev. Fluid Mech.*, 20(1):35–59, 1988.

[70] M. J. Blunt, B. Bijeljic, H. Dong, O. Gharbi, S. Iglauer, P. Mostaghimi, A. Paluszny, and C. Pentland. Pore-scale imaging and modelling. *Adv. Water Resour.*, 51:197–216, January 2013.

[71] D. Wildenschild and A. P. Sheppard. X-ray imaging and analysis techniques for quantifying pore-scale structure and processes in subsurface porous medium systems. *Adv. Water Resour.*, 51:217–246, January 2013.

[72] S. Berg, H. Ott, S. A. Klapp, A. Schwing, R. Neiteler, N. Brussee, A. Makurat, L. Leu, F. Enzmann, J.-O. Schwarz, M. Kersten, S. Irvine, and M. Stampanoni. Real-time 3d imaging of Haines jumps in porous media flow. *P. Natl. A. Sci.*, 110(10):3755–3759, March 2013.

[73] C. Pan, M. Hilpert, and C. T. Miller. Lattice-Boltzmann simulation of two-phase flow in porous media. *Water Resour. Res.*, 40(1), 2004.

[74] A. Q. Raeini, M. J. Blunt, and B. Bijeljic. Modelling two-phase flow in porous media at the pore scale using the volume-of-fluid method. *J. Comput. Phys.*, 231(17):5653–5668, July 2012.

[75] F. O. Alpak, B. Riviere, and F. Frank. A phase-field method for the direct simulation of two-phase flows in pore-scale media using a non-equilibrium wetting boundary condition. *Computat. Geosci.*, 20(5):881–908, October 2016.

[76] N. C. Wardlaw and M. McKellar. Mercury porosimetry and the interpretation of pore geometry in sedimentary rocks and artificial models. *Powder Technol.*, 29(1):127–143, May 1981.

[77] W. E. Soll, M. A. Celia, and J. L. Wilson. Micromodel studies of three-fluid porous media systems: Pore-scale processes relating to capillary pressure-saturation relationships. *Water Resour. Res.*, 29(9):2963–2974, 1993.

[78] N. K. Karadimitriou, S. M. Hassanizadeh, V. Joekar-Niasar, and P. J. Kleingeld. Micromodel study of two-phase flow under transient conditions: Quantifying effects of specific interfacial area. *Water Resour. Res.*, 50(10):8125–8140, 2014.

[79] S. Diamond. Mercury porosimetry: an inappropriate method for the measurement of pore size distributions in cement-based materials. *Cement Concrete Res.*, 30(10):1517–1525, 2000.

[80] A. G. Hunt, R. P. Ewing, and R. Horton. What's wrong with soil physics? *Soil Sci. Soc. Am. J.*, 77(6):1877–1887, 2013.

[81] W. B. Haines. Studies in the physical properties of soil: V. The hysteresis effect in capillary properties, and the modes of moisture distribution associated therewith. *J. Agr. Sci.*, 20(01):97–116, 1930.

[82] J. C. P. Broekhoff and J. H. De Boer. Studies on pore systems in catalysts: XI. Pore distribution calculations from the adsorption branch of a nitrogen adsorption isotherm in the case of "ink-bottle" type pores. *J. Catal.*, 10(2):153–165, 1968.

[83] F. Moro and H. Böhni. Ink-bottle effect in mercury intrusion porosimetry of cement-based materials. *J. Colloid Interf. Sci.*, 246(1):135–149, 2002.

[84] R. H. Brooks and A. T. Corey. Hydraulic properties of porous media and their relation to drainage design. *T. ASAE*, 7(1):26–0028, 1964.

[85] M. T. van Genuchten. A closed-form equation for predicting the hydraulic conductivity of unsaturated soils. *Soil Sci. Soc. Am. J.*, 44(5):892–898, 1980.

[86] M. C. Leverett. Capillary behavior in porous solids. *T. AIME*, 142(01):152–169, 1941.

[87] M. C. Leverett, W. B. Lewis, and M. E. True. Dimensional-model studies of oil-field behavior. *T. AIME*, 146(01):175–193, 1942.

[88] W. Rose and W. A. Bruce. Evaluation of capillary character in petroleum reservoir rock. *J. Petrol. Technol.*, 1(05):127–142, 1949.

[89] Y. Mualem. A conceptual model of hysteresis. *Water Resour. Res.*, 10(3):514–520, 1974.

[90] Y. Mualem and G. Dagan. A dependent domain model of capillary hysteresis. *Water Resour. Res.*, 11(3):452–460, 1975.

[91] Y. Mualem. A modified dependent-domain theory of hysteresis. *Soil Sci.*, 137(5):283–291, 1984.

[92] P. S. Scott, G. J. Farquhar, and N. Kouwen. Hysteretic effects on net infiltration. *Adv. Infiltration*, pages 163–170, 1983.

[93] J. B. Kool and J. C. Parker. Development and evaluation of closed-form expressions for hysteretic soil hydraulic properties. *Water Resour. Res.*, 23(1):105–114, 1987.

[94] J. C. Parker and R. J. Lenhard. A model for hysteretic constitutive relations governing multiphase flow: 1. Saturation-pressure relations. *Water Resour. Res.*, 23(12):2187–2196, 1987.

[95] L. Cueto-Felgueroso, X. Fu, and R. Juanes. Pore-scale modeling of phase change in porous media. *Phys. Rev. Fluids*, 3(8):084302, 2018.

[96] J. van Brakel. Pore space models for transport phenomena in porous media review and evaluation with special emphasis on capillary liquid transport. *Powder Technol.*, 11(3):205–236, 1975.

[97] J. A. Quiblier. A new three-dimensional modeling technique for studying porous media. *J. Colloid Interf. Sci.*, 98(1):84–102, 1984.

[98] S. G. Oh and J. C. Slattery. Interfacial tension required for significant displacement of residual oil. *Soc. Petrol. Eng. J.*, 19(02):83–96, 1979.

[99] R. P. Mayer and R. A. Stowe. Mercury porosimetry - breakthrough pressure for penetration between packed spheres. *J. Coll. Sci.*, 20(8):893–911, 1965.

[100] R. P. Mayer and R. A. Stowe. Mercury porosimetry: filling of toroidal void volume following breakthrough between packed spheres. *J. Phys. Chem.*, 70(12):3867–3873, 1966.

[101] D. M. Smith and D. L. Stermer. Particle size analysis via mercury intrusion measurements. *Powder Technol.*, 53(1):23–30, 1987.

[102] M. D. Fredlund, G. W. Wilson, and D. G. Fredlund. Use of the grain-size distribution for estimation of the soil-water characteristic curve. *Can. Geotech. J.*, 39(5):1103–1117, 2002.

[103] H. I. Meyer. Pore distribution in porous media. *J. Appl. Phys.*, 24(5):510–512, 1953.

[104] V. I. Selyakov and V. Kadet. *Percolation models for transport in porous media: with applications to reservoir engineering*, volume 9. Springer Science & Business Media, 2013.

[105] M. B. Pinson, T. Zhou, H. M. Jennings, and M. Z. Bazant. Inferring Pore Connectivity from Sorption Hysteresis in Multiscale Porous Media. *arXiv:1402.3377 [cond-mat]*, February 2014.

[106] B. Albers. Modeling the hysteretic behavior of the capillary pressure in partially saturated porous media: a review. *Acta Mech.*, 225(8):2163–2189, 2014.

[107] G. I. Barenblatt. Filtration of two nonmixing fluids in a homogeneous porous medium. *Fluid Dyn.*, 6(5):857–864, 1971.

[108] L. Luckner, M. T. van Genuchten, and D. R. Nielsen. A consistent set of parametric models for the two-phase flow of immiscible fluids in the subsurface. *Water Resour. Res.*, 25(10):2187–2193, 1989.

[109] S. M. Hassanizadeh and W. G. Gray. Mechanics and thermodynamics of multiphase flow in porous media including interphase boundaries. *Adv. Water Resour.*, 13(4):169–186, 1990.

[110] G. I. Barenblatt, T. W. Patzek, and D. B. Silin. The mathematical model of nonequilibrium effects in water-oil displacement. *SPE J.*, 8(04):409–416, 2003.

[111] R. Juanes. Nonequilibrium effects in models of three-phase flow in porous media. *Adv. Water Resour.*, 31(4):661–673, 2008.

[112] S. M. Hassanizadeh and W. G. Gray. Thermodynamic basis of capillary pressure in porous media. *Water Resour. Res.*, 29(10):3389–3405, 1993.

[113] F. Kalaydjian. A macroscopic description of multiphase flow in porous media involving spacetime evolution of fluid/fluid interface. *Transport Porous Med.*, 2(6):537–552, 1987.

[114] A. Y. Beliaev and S. M. Hassanizadeh. A theoretical model of hysteresis and dynamic effects in the capillary relation for two-phase flow in porous media. *Transport Porous Med.*, 43(3):487–510, 2001.

[115] S. M. Hassanizadeh, M. A. Celia, and H. K. Dahle. Dynamic effect in the capillary pressure–saturation relationship and its impacts on unsaturated flow. *Vadose Zone J.*, 1(1):38–57, 2002.

[116] J.-T. Cheng, L. J. Pyrak-Nolte, D. D. Nolte, and N. J. Giordano. Linking pressure and saturation through interfacial areas in porous media. *Geophys. Res. Lett.*, 31(8), 2004.

[117] D. Chen, L. J. Pyrak-Nolte, J. Griffin, and N. J. Giordano. Measurement of interfacial area per volume for drainage and imbibition. *Water Resour. Res.*, 43(12), 2007.

[118] L. J. Pyrak-Nolte, D. D. Nolte, D. Chen, and N. J. Giordano. Relating capillary pressure to interfacial areas. *Water Resour. Res.*, 44(6), 2008.

[119] M. L. Porter, M. G. Schaap, and D. Wildenschild. Lattice-Boltzmann simulations of the capillary pressure-saturation-interfacial area relationship for porous media. *Adv. Water Resour.*, 32(11):1632–1640, 2009.

[120] P. C. Reeves and M. A. Celia. A Functional Relationship Between Capillary Pressure, Saturation, and Interfacial Area as Revealed by a Pore-Scale Network Model. *Water Resour. Res.*, 32(8):2345–2358, 1996.

[121] R. J. Held and M. A. Celia. Modeling support of functional relationships between capillary pressure, saturation, interfacial area and common lines. *Adv. Water Resour.*, 24(3):325–343, 2001.

[122] V. Joekar-Niasar, S. M. Hassanizadeh, and A. Leijnse. Insights into the relationships among capillary pressure, saturation, interfacial area and relative permeability using pore-network modeling. *Transport Porous Med.*, 74(2):201–219, 2008.

[123] V. Joekar-Niasar and S. M. Hassanizadeh. Uniqueness of specific interfacial area - capillary pressure-saturation relationship under non-equilibrium conditions in two-phase porous media flow. *Transport Porous Med.*, 94(2):465–486, 2012.

[124] J. O. Helland and S. M. Skjaeveland. Relationship between capillary pressure, saturation, and interfacial area from a model of mixed-wet triangular tubes. *Water Resour. Res.*, 43(12), 2007.

[125] R. Hilfer. Macroscopic equations of motion for two-phase flow in porous media. *Phys. Rev. E*, 58(2):2090, 1998.

[126] R. Hilfer. Macroscopic capillarity and hysteresis for flow in porous media. *Phys. Rev. E*, 73(1):016307, 2006.

[127] F. Doster, P. A. Zegeling, and R. Hilfer. Numerical solutions of a generalized theory for macroscopic capillarity. *Phys. Rev. E*, 81(3):036307, 2010.

[128] H. M. Rootare. A review of mercury porosimetry. In *Advanced Experimental Techniques in Powder Metallurgy*, pages 225–252. Springer, 1970.

[129] S. Diamond. Pore size distributions in clays. *Clay. Clay Miner.*, 18(1):7–23, 1970.

[130] J. van Brakel, S. Modrỳ, and M. Svata. Mercury porosimetry: state of the art. *Powder Technol.*, 29(1):1–12, 1981.

[131] C. A. L. y Leon. New perspectives in mercury porosimetry. *Adv. Colloid Interfac.*, 76:341–372, 1998.

[132] H. Giesche. Mercury Porosimetry: A General (Practical) Overview. *Part. Part. Syst. Char.*, 23(1):9–19, 2006.

[133] E. Romero and P. H. Simms. Microstructure investigation in unsaturated soils: a review with special attention to contribution of mercury intrusion porosimetry and environmental scanning electron microscopy. In *Laboratory and Field Testing of Unsaturated Soils*, pages 93–115. Springer, 2008.

[134] Marcia L. Huber, Arno D. Laesecke, and Daniel G. Friend. The Vapor Pressure of Mercury. *NIST Interagency/Internal Report (NISTIR) - 6643*, April 2006.

[135] J. H. Caro and H. P. Freeman. Physical structure of fertilizer materials, pore structure of phosphate rock and triple superphosphate. *J. Agr. Food Chem.*, 9(3):182–186, 1961.

[136] C. Salmas and G. Androutsopoulos. Mercury porosimetry: contact angle hysteresis of materials with controlled pore structure. *J. Colloid Interf. Sci.*, 239(1):178–189, 2001.

[137] F. A. L. Dullien and G. K. Dhawan. Characterization of pore structure by a combination of quantitative photomicrography and mercury porosimetry. *J. Colloid Interf. Sci.*, 47(2):337–349, 1974.

[138] F. A. L. Dullien and G. K. Dhawan. Bivariate pore-size distributions of some sandstones. *J. Colloid Interf. Sci.*, 52(1):129–135, 1975.

[139] G. P. Androutsopoulos and R. Mann. Evaluation of mercury porosimeter experiments using a network pore structure model. *Chem. Eng. Sci.*, 34(10):1203–1212, January 1979.

[140] G. R. Lapidus, A. M. Lane, K. M. Ng, and W. C. Conner. Interpretation of mercury porosimetry data using a pore-throat network model. *Chem. Eng. Commun.*, 38(1-2):33–56, 1985.

[141] C. D. Tsakiroglou and A. C. Payatakes. A new simulator of mercury porosimetry for the characterization of porous materials. *J. Colloid Interf. Sci.*, 137(2):315–339, 1990.

[142] R. L. Portsmouth and L. F. Gladden. Determination of pore connectivity by mercury porosimetry. *Chem. Eng. Sci.*, 46(12):3023–3036, 1991.

[143] M. A. Ioannidis and I. Chatzis. A Mixed-Percolation Model of Capillary Hysteresis and Entrapment in Mercury Porosimetry. *J. Colloid Interf. Sci.*, 161(2):278–291, December 1993.

[144] C. D. Tsakiroglou and A. C. Payatakes. Characterization of the pore structure of reservoir rocks with the aid of serial sectioning analysis, mercury porosimetry and network simulation. *Adv. Water Resour.*, 23(7):773–789, June 2000.

[145] R. G. Larson and N. R. Morrow. Effects of sample size on capillary pressures in porous media. *Powder Technol.*, 30(2):123–138, 1981.

[146] G. C. Wall and R. J. C. Brown. The determination of pore-size distributions from sorption isotherms and mercury penetration in interconnected pores: The application of percolation theory. *J. Colloid Interf. Sci.*, 82(1):141–149, 1981.

[147] A. E.-A. Heiba. Porous media: fluid distributions and transport with applications to petroleum recovery. Technical report, Minnesota Univ., Minneapolis (USA), 1985.

[148] A. Lane, N. Shah, and W. M. C. Conner. Measurement of the morphology of high-surface-area solids: porosimetry as a percolation process. *J. Colloid Interf. Sci.*, 109(1):235–242, 1986.

[149] A. Tsetsekou, G. P. Androutsopoulos, and R. Mann. Mercury porosimetry hysteresis and entrapment predictions based on a corrugated random pore model. *Chem. Eng. Commun.*, 110(1):1–29, 1991.

[150] G. P. Androutsopoulos and C. E. Salmas. A simplified model for mercury porosimetry hysteresis. *Chem. Eng. Commun.*, 176(1):1–42, 1999.

[151] N. C. Wardlaw and J. P. Cassan. Estimation of Recovery Efficiency by Visual Observation of Pore Systems in Reservoir Rocks. *B. Can. Petrol. Geol.*, 26(4):572–585, 1978.

[152] Y. Li and N. C. Wardlaw. The influence of wettability and critical pore-throat size ratio on snap-off. *J. Colloid Interf. Sci.*, 109(2):461–472, 1986.

[153] R. D. Hill. A study of pore size distribution of fired clay bodies. *Trans. Brit. Ceram. Soc*, 59(6):189–212, 1960.

[154] T. A. Ell and S. J. Sangwine. Quaternion involutions and anti-involutions. *Comput. Math. Appl.*, 53(1):137–143, January 2007.

[155] *SCHOTT CoralPor Porous Glass Product Information.* 2013.

[156] *SASOL PURAL / CATAPAL high purity aluminas.* 2003.

[157] H. H. Gerke and M. T. van Genuchten. A dual-porosity model for simulating the preferential movement of water and solutes in structured porous media. *Water Resour. Res.*, 29(2):305–319, 1993.

[158] G. Mason. The effect of pore space connectivity on the hysteresis of capillary condensation in adsorption—desorption isotherms. *J. Colloid Interf. Sci.*, 88(1):36–46, 1982.

[159] G. Mason. The effect of pore lattice structure on the pore size distributions calculated from sorption isotherms using percolation theory. *J. Colloid Interf. Sci.*, 95(1):277–278, September 1983.

[160] M. Parlar and Y. C. Yortsos. Percolation theory of vapor adsorption—desorption processes in porous materials. *J. Colloid Interf. Sci.*, 124(1):162–176, 1988.

[161] N. A. Seaton. Determination of the connectivity of porous solids from nitrogen sorption measurements. *Chem. Eng. Sci.*, 46(8):1895–1909, 1991.

[162] E. Masoero, M. B. Pinson, P. A. Bonnaud, H. Manzano, Q. Ji, S. Yip, J. J. Thomas, M. Z. Bazant, K. Van Vliet, and H. M. Jennings. Modelling Hysteresis in the Water Sorption and Drying Shrinkage of Cement Paste. September 2015.

[163] M. B. Pinson, E. Masoero, P. A. Bonnaud, H. Manzano, Q. Ji, S. Yip, J. J. Thomas, M. Z. Bazant, K. J. Van Vliet, and H. M. Jennings. Hysteresis from multiscale porosity: modeling water sorption and shrinkage in cement paste. *Phys. Rev. Appl.*, 3(6):064009, 2015.

[164] J. T. Gostick, M. A. Ioannidis, M. W. Fowler, and M. D. Pritzker. Direct measurement of the capillary pressure characteristics of water–air–gas diffusion layer systems for PEM fuel cells. *Electrochem. Commun.*, 10(10):1520–1523, 2008.

[165] A. Forner-Cuenca, J. Biesdorf, A. Lamibrac, V. Manzi-Orezzoli, F. N. Büchi, L. Gubler, T. J. Schmidt, and P. Boillat. Advanced Water Management in PEFCs: Diffusion Layers with Patterned Wettability II. Measurement of Capillary Pressure Characteristic with Neutron and Synchrotron Imaging. *J. Electrochem. Soc.*, 163(9):F1038–F1048, 2016.

[166] A. Lamibrac, J. Roth, M. Toulec, F. Marone, M. Stampanoni, and F. N. Büchi. Characterization of liquid water saturation in gas diffusion layers by x-ray tomographic microscopy. *J. Electrochem. Soc.*, 163(3):F202–F209, 2016.

[167] M. Sabharwal, J. T. Gostick, and M. Secanell. Virtual Liquid Water Intrusion in Fuel Cell Gas Diffusion Media. *J. Electrochem. Soc.*, 165(7):F553–F563, 2018.

[168] T. G. Tranter, J. T. Gostick, A. D. Burns, and W. F. Gale. Capillary Hysteresis in Neutrally Wettable Fibrous Media: A Pore Network Study of a Fuel Cell Electrode. *Transport Porous Med.*, 121(3):597–620, 2018.

[169] F. A. L. Dullien. Determination of Pore Accessibilities - An Approach. *J. Petrol. Technol.*, 21(01):14–15, January 1969.

[170] F. A. L. Dullien. Wood's metal porosimetry and its relation to mercury porosimetry. *Powder Technol.*, 29(1):109–116, May 1981.

[171] A. B. Abell, K. L. Willis, and D. A. Lange. Mercury intrusion porosimetry and image analysis of cement-based materials. *J. Colloid Interf. Sci.*, 211(1):39–44, 1999.

[172] A. T. Corey. The interrelation between gas and oil relative permeabilities. *Produc. Mon.*, 19(1):38–41, 1954.

[173] S. F. Averjanov. About permeability of surface soils in case of incomplete saturation. *Eng. Collect.*, 7:19–21, 1950.

[174] S. Irmay. On the hydraulic conductivity of unsaturated soils. *Eos T. Am. Geophys. Un.*, 35(3):463–467, 1954.

[175] M. Boreli and G. Vachaud. Note sur la détermination de la teneur en eau résiduelle et sur la variation de la perméabilité relative dans les sols non saturés. *C. R. Ac. Sci. Paris*, 263(19):698, 1966.

[176] G. Vachaud. Étude du régime transitoire de l'écoulement de l'eau pendant le drainage des nappes à surface libre. *La Houille Blanche*, 5:391–406, 1968.

[177] W. Brutsaert. Some Methods of Calculating Unsaturated Permeability. *T. ASAE*, 10(3):0400–0404, 1967.

[178] Y. Mualem. A new model for predicting the hydraulic conductivity of unsaturated porous media. *Water Resour. Res.*, 12(3):513–522, 1976.

[179] I. Fatt and H. Dykstra. Relative permeability studies. *J. Petrol. Technol.*, 3(09):249–256, 1951.

[180] N. T. Burdine. Relative permeability calculations from pore size distribution data. *J. Petrol. Technol.*, 5(03):71–78, 1953.

[181] M. R. J. Wyllie and G. H. F. Gardner. The generalized Kozeny-Carman equation. *World Oil*, 146(4):121–128, 1958.

[182] J. Koplik. Creeping flow in two-dimensional networks. *J. Fluid Mech.*, 119:219–247, 1982.

[183] S. Tyč and B. I. Halperin. Random resistor network with an exponentially wide distribution of bond conductances. *Phys. Rev. B*, 39(1):877–880, January 1989.

[184] J. Koplik, T. J. Lasseter, and others. Two-phase flow in random network models of porous media. *Soc. Petrol. Eng. J.*, 25(01):89–100, 1985.

[185] M. A. Celia, E. T. Bouloutas, and R. L. Zarba. A general mass-conservative numerical solution for the unsaturated flow equation. *Water Resour. Res.*, 26(7):1483–1496, 1990.

[186] R. Mourhatch, T. T. Tsotsis, and M. Sahimi. Determination of the true pore size distribution by flow permporometry experiments: an invasion percolation model. *J. Membrane Sci.*, 367(1):55–62, 2011.

[187] V. V. Kadet and A. M. Galechyan. Percolation model of relative permeability hysteresis. *J. Appl. Mech. Tech. Phys.*, 54(3):423–432, 2013.

[188] D. Wilkinson and D. F. Willemsen. Invasion percolation: a new form of percolation theory. *J. Phys. A-Math. Gen.*, 16(14):3365, 1983.

[189] I. Fatt. Network model of porous media. *J. Petrol. Technol.*, 8(7):144–177, 1956.

[190] R. A. Ketcham and W. D. Carlson. Acquisition, optimization and interpretation of X-ray computed tomographic imagery: applications to the geosciences. *Comput. Geosci.*, 27(4):381–400, 2001.

[191] A. P. Sheppard, R. M. Sok, and H. Averdunk. Techniques for image enhancement and segmentation of tomographic images of porous materials. *Physica A*, 339(1):145–151, 2004.

[192] A. Kaestner, E. Lehmann, and M. Stampanoni. Imaging and image processing in porous media research. *Adv. Water Resour.*, 31(9):1174–1187, 2008.

[193] M. Tuller, R. Kulkarni, and W. Fink. Segmentation of X-ray CT data of porous materials: A review of global and locally adaptive algorithms. *Soil–Water–Root Processes: Advances in Tomography and Imaging*, soilwaterrootpr:157–182, 2013.

[194] S. Schlüter, A. Sheppard, K. Brown, and D. Wildenschild. Image processing of multiphase images obtained via X-ray microtomography: a review. *Water Resour. Res.*, 50(4):3615–3639, 2014.

[195] M. Sezgin and B. Sankur. Survey over image thresholding techniques and quantitative performance evaluation. *J. Electron. Imaging*, 13(1):146–166, 2004.

[196] P. Iassonov, T. Gebrenegus, and M. Tuller. Segmentation of X-ray computed tomography images of porous materials: A crucial step for characterization and quantitative analysis of pore structures. *Water Resour. Res.*, 45(9), 2009.

[197] P. C. Baveye, M. Laba, W. Otten, L. Bouckaert, P. D. Sterpaio, R. R. Goswami, D. Grinev, A. Houston, Y. Hu, and J. Liu. Observer-dependent variability of the thresholding step in the quantitative analysis of soil images and X-ray microtomography data. *Geoderma*, 157(1-2):51–63, 2010.

[198] M. L. Porter and D. Wildenschild. Image analysis algorithms for estimating porous media multiphase flow variables from computed microtomography data: a validation study. *Computat. Geosci.*, 14(1):15–30, 2010.

[199] R. D. Hazlett. Simulation of capillary-dominated displacements in microtomographic images of reservoir rocks. *Transport Porous Med.*, 20(1-2):21–35, 1995.

[200] C. A. Baldwin, A. J. Sederman, M. D. Mantle, P. Alexander, and L. F. Gladden. Determination and characterization of the structure of a pore space from 3d volume images. *J. Colloid Interf. Sci.*, 181(1):79–92, 1996.

[201] T. W. Patzek. Verification of a complete pore network simulator of drainage and imbibition. In *SPE/DOE Improved Oil Recovery Symposium*. Society of Petroleum Engineers, 2000.

[202] H. Dong and M. J. Blunt. Pore-network extraction from micro-computerized-tomography images. *Phys. Rev. E*, 80(3):036307, September 2009.

[203] H. Okabe and M. J. Blunt. Prediction of permeability for porous media reconstructed using multiple-point statistics. *Phys. Rev. E*, 70(6):066135, 2004.

[204] A. Anbari, H.-T. Chien, S. S. Datta, W. Deng, D. A. Weitz, and J. Fan. Microfluidic Model Porous Media: Fabrication and Applications. *Small*, 14(18):1703575, 2018.

[205] R. Hu, J. Wan, Y. Kim, and T. K. Tokunaga. Wettability effects on supercritical CO2–brine immiscible displacement during drainage: Pore-scale observation and 3d simulation. *Int. J. Greenh. Gas Con.*, 60:129–139, 2017.

[206] H. S. Rabbani, V. Joekar-Niasar, T. Pak, and N. Shokri. New insights on the complex dynamics of two-phase flow in porous media under intermediate-wet conditions. *Sci. Rep.-UK*, 7(1):4584, 2017.

[207] H. S. Rabbani, D. Or, Y. Liu, C.-Y. Lai, N. B. Lu, S. S. Datta, H. A. Stone, and N. Shokri. Suppressing viscous fingering in structured porous media. *P. Natl. A. Sci.*, 115(19):4833–4838, 2018.

[208] W. B. Lindquist, S.-M. Lee, D. A. Coker, K. W. Jones, and P. Spanne. Medial axis analysis of void structure in three-dimensional tomographic images of porous media. *J. Geophys. Res. Sol. Ea.*, 101(B4):8297–8310, 1996.

[209] S. Bakke and P. E. Øren. 3-D pore-scale modelling of sandstones and flow simulations in the pore networks. *SPE J.*, 2(02):136–149, 1997.

[210] W. B. Lindquist and A. Venkatarangan. Investigating 3d geometry of porous media from high resolution images. *Phys. Chem. Earth Pt. A*, 24(7):593–599, 1999.

[211] J. F. Delerue, E. Perrier, Z. Y. Yu, and B. Velde. New algorithms in 3d image analysis and their application to the measurement of a spatialized pore size distribution in soils. *Phys. Chem. Earth Pt. A*, 24(7):639–644, 1999.

[212] J.-F. Delerue and E. Perrier. DXSoil, a library for 3d image analysis in soil science. *Comput. Geosci.*, 28(9):1041–1050, 2002.

[213] P. E. Øren and S. Bakke. Process based reconstruction of sandstones and prediction of transport properties. *Transport Porous Med.*, 46(2-3):311–343, 2002.

[214] P. E. Øren and S. Bakke. Reconstruction of Berea sandstone and pore-scale modelling of wettability effects. *J. Petrol. Sci. Eng.*, 39(3-4):177–199, 2003.

[215] K. Suzuki, I. Horiba, and N. Sugie. Linear-time connected-component labeling based on sequential local operations. *Comput. Vis. Image Und.*, 89(1):1–23, 2003.

[216] Y. S. Kim. Recognition of form features using convex decomposition. *Comput. Aided Design*, 24(9):461–476, 1992.

[217] J.-M. Lien and N. M. Amato. Approximate convex decomposition of polygons. *Computat. Geom.*, 35(1-2):100–123, 2006.

[218] D. F. Watson. Computing the n-dimensional Delaunay tessellation with application to Voronoi polytopes. *Comput. J.*, 24(2):167–172, 1981.

[219] C. Rycroft. Voro++: A three-dimensional Voronoi cell library in C++. Technical report, Lawrence Berkeley National Lab.(LBNL), Berkeley, CA (United States), 2009.

[220] P.-E. Danielsson. Euclidean distance mapping. *Comput. Vision Graph.*, 14(3):227–248, 1980.

[221] R. Courant, K. Friedrichs, and H. Lewy. Über die partiellen Differenzengleichungen der mathematischen Physik. *Math. Ann.*, 100(1):32–74, 1928.

[222] A. M. Khudhair and M. M. Farid. A review on energy conservation in building applications with thermal storage by latent heat using phase change materials. *Energ. Convers. Manage.*, 45(2):263–275, January 2004.

[223] P. C. Carman and P. R. Malherbe. Routine measurement of surface of paint pigments and other fine powders. I. *J. Soc. Chem. Ind.*, 69(5):134–143, 1950.

[224] P. C. Carman and F. A. Raal. Diffusion and flow of gases and vapours through micropores III. Surface diffusion coefficients and activation energies. *P. Roy. Soc. Lond. A Mat.*, 209(1096):38–58, 1951.

[225] H. Rhim and S.-T. Hwang. Transport of capillary condensate. *J. Colloid Interf. Sci.*, 52(1):174–181, 1975.

[226] C. Hall. Water sorptivity of mortars and concretes: a review. *Mag. Concrete Res.*, 41(147):51–61, 1989.

[227] E. S. Kikkinides, K. P. Tzevelekos, A. K. Stubos, M. E. Kainourgiakis, and N. K. Kanellopoulos. Application of effective medium approximation for the determination of the permeability of condensable vapours through mesoporous media. *Chem. Eng. Sci.*, 52(16):2837–2844, August 1997.

[228] E. Shahraeeni and D. Or. Pore scale mechanisms for enhanced vapor transport through partially saturated porous media. *Water Resour. Res.*, 48(5), 2012.

[229] J. Chirife and H. A. Iglesias. Equations for fitting water sorption isotherms of foods: Part 1 — a review. *Int. J. Food Sci. Tech.*, 13(3):159–174, 1978.

[230] A. D. Roman-Gutierrez, S. Guilbert, and B. Cuq. Distribution of Water between Wheat Flour Components: A Dynamic Water Vapour Adsorption Study. *J. Cereal Sci.*, 36(3):347–355, November 2002.

[231] C. A. S. Hill, A. J. Norton, and G. Newman. The water vapour sorption properties of Sitka spruce determined using a dynamic vapour sorption apparatus. *Wood Sci. Technol.*, 44(3):497–514, August 2010.

[232] Y. Xie, C. A. S. Hill, Z. Jalaludin, S. F. Curling, R. D. Anandjiwala, A. J. Norton, and G. Newman. The dynamic water vapour sorption behaviour of natural fibres and kinetic analysis using the parallel exponential kinetics model. *J. Mater. Sci.*, 46(2):479–489, January 2011.

[233] M. B. Pinson. *Non-equilibrium thermodynamics in porous media : battery degradation, and sorption and transport in porous materials.* Thesis, Massachusetts Institute of Technology, 2015.

[234] I. Prigogine, R. Defay, and D. H. Everett. *Chemical thermodynamics*, volume 32. Longmans London, 1954.

[235] S. R. De Groot and P. Mazur. *Non-equilibrium thermodynamics.* Courier Corporation, 2013.